



저작자표시-비영리-변경금지 2.0 대한민국

이용자는 아래의 조건을 따르는 경우에 한하여 자유롭게

- 이 저작물을 복제, 배포, 전송, 전시, 공연 및 방송할 수 있습니다.

다음과 같은 조건을 따라야 합니다:



저작자표시. 귀하는 원저작자를 표시하여야 합니다.



비영리. 귀하는 이 저작물을 영리 목적으로 이용할 수 없습니다.



변경금지. 귀하는 이 저작물을 개작, 변형 또는 가공할 수 없습니다.

- 귀하는, 이 저작물의 재이용이나 배포의 경우, 이 저작물에 적용된 이용허락조건을 명확하게 나타내어야 합니다.
- 저작권자로부터 별도의 허가를 받으면 이러한 조건들은 적용되지 않습니다.

저작권법에 따른 이용자의 권리는 위의 내용에 의하여 영향을 받지 않습니다.

이것은 [이용허락규약\(Legal Code\)](#)을 이해하기 쉽게 요약한 것입니다.

[Disclaimer](#)

공학박사 학위논문

**Three-Dimensionally Architected
Multiscale Low-Temperature Solid Oxide
Fuel Cells**

**3 차원 아키텍처링을 이용한 멀티스케일 저온형
고체산화물 연료전지**

2019 년 8 월

서울대학교 대학원

기계항공공학부

신 성 수

3 차원 아키텍처링을 이용한 멀티스케일 저온형 고체산화물 연료전지

Three-Dimensionally Architected Multiscale Low-
Temperature Solid Oxide Fuel Cells

지도교수 최 만 수

이 논문을 공학박사 학위논문으로 제출함

2019 년 4 월

서울대학교 대학원

기계항공공학부

신 성 수

신성수의 공학박사 학위논문을 인준함

2019 년 6 월

위원장 : 고 승 환 
부위원장 : 최 만 수 
위원 : 이 훈 석 
위원 : 김 형 천 
위원 : 강 성 빈 

Three-Dimensionally Architected Multiscale Low-Temperature Solid Oxide Fuel Cells

Sung Soo Shin

Department of Mechanical and Aerospace Engineering

The Graduate School

Seoul National University

Abstract

Fuel cell, one of the promising next-generation energy conversion systems, is eco-friendly electrochemical device and has characteristics of low emission of pollutant and high energy output per weight. Among fuel cells, solid oxide fuel cell (SOFC) has the highest efficiency of power generation and has an advantage of hydrocarbon fuel using including hydrogen through the internal reforming. However, conventional SOFCs have limitations of thermal performance degradation, high cost of system maintenance and difficulty in application to mobile systems due to the high operating temperature above 700 °C. Therefore, lowering the operating temperature has been one of the remarkable goals of SOFC systems, and researches of structural development have been conducted to implement a low-temperature SOFC (LT-SOFC). In this thesis, we have developed

advanced multiscale electrode architecturing technologies and novel three-dimensional interface architecturing technologies that overcome the limitations of previously reported researches for the implementation of LT-SOFC.

First, we have optimized the structure of each component of SOFCs using a powder-suspension electrospray deposition process and confirmed the stable operation of the fuel cell at high operating temperature. A polyvinyl butyral polymer binder was used for the fabrication of a dense electrolyte layer to block the gas permeation between the anode and the cathode, and a polyvinylpyrrolidone polymer binder was used for the cathode layer to be porous for the gas flow. The focus of our research was on the morphology of the structure after sintering depending on the weight ratio of the ceramic powder and the polymer binder in the suspension during the electrospray deposition process. The deposited cathode layer was uniformly dispersed under the condition of 1:1 weight ratio of the cathode powder and the polymer binder. In addition, we figured out through the particle size analyzer and scanning electron microscope analysis that the dispersion status of the suspension could affect not only the as deposited structure but also the sintered. As a result, a fuel cell with an optimized electrolyte and cathode structure resulted in a peak power density of 805 mW/cm^2 at an operating temperature of $650 \text{ }^\circ\text{C}$. Also, the degradation rate was 1.5 % for 100 hours at the condition of a constant current density of 0.4 A/cm^2 at $650 \text{ }^\circ\text{C}$, which verified that the performance in long-term measurement was maintained.

Next, we developed two different multiscale electrode architecturing technologies, a ceramic thin film fabrication technology and a novel infiltration technology, via a precursor-solution electro spray deposition process. First, we fabricated ceramic thin films using a precursor-solution electro spray deposition process and applied them as nanoscale interlayers between the SOFC electrolyte and the cathode layer. In our previous study, we have optimized a micro-thick structure using a powder-suspension electro spray deposition process, while subsequent researches have fabricated thin film structures under micron thickness using a precursor-solution electro spray deposition process. In particular, in this study, the stable spray condition of the precursor solution using deionized water as a solvent, which has three times higher surface tension than ethyl alcohol, was established by using silica nozzle with 8 μm tip diameter. Nano adhesion layer (nAL) and nano cathode functional layer (nCFL) were fabricated, and the nAL-cell and nCFL-cell were prepared by inserting nanoscale interlayer between electrolyte layer and cathode layer of SOFCs. We also fabricated Ref-cell without nanoscale interlayer and evaluated the performance of all three cells. As a result, the maximum power density of nCFL-cell increased by 18 % and 13 % compared to nAL-cell and Ref-cell at 650 $^{\circ}\text{C}$, respectively. Those results were derived from two reasons: (i) the increase of the oxygen ion transport pathways due to the better adhesion by the nanoscale interlayer inserted between the electrolyte layer and the cathode layer; and (ii) the maximization of oxygen reduction reaction (ORR) sites by smaller particle size of nanoscale interlayer. Second, a

novel strategy of infiltration process was developed to enhance the performance of SOFC by improving the microstructure of electrode. The traditional infiltration process was a simple method of dropping the precursor solution onto the electrode using a micropipette. However, there are issues that are difficult to infiltrate uniformly into the entire surface of the electrode and difficult to control the flow of the infiltrated precursor-solution. In this study, a novel infiltration process was developed to uniformly deposit the precursor-solution onto the electrode using the precursor-solution electrospray deposition process and control the infiltration rate of the precursor-solution according to the humidity. The fuel cell with our new infiltration process resulted in higher maximum powder density of 15 % and 215 % compared to the conventionally infiltrated fuel cell and the non-infiltrated fuel cell at 650 °C, respectively. The significant increase of performance can be explained by the improvement of the electrode reaction mechanism such as increase of electrochemical reaction sites through the sintering of uniformly infiltrated precursor-solution by humidification.

Finally, we have developed a micro-ceramic imprinting technology that combines a micro pattern imprinting and a tape lamination process, which is a method of manufacturing SOFC anode support, and fabricated three-dimensional SOFCs using thin film deposition processes. It has been well known that the microscale surface patterning of ceramic materials is difficult because of their fragile properties. In this research, to solve those problems, we developed pyramid patterned anode support by lamination

process of polymer-ceramic composite anode tapes and polymer mold with micro pattern. In addition, we used sputtering and pulsed laser deposition process to deposit electrolyte and cathode layer of full test cells. The cells with a flat structure without a PUA polymer mold in the lamination process and a three-dimensional pyramid structure were denoted as Planar-cell and 3DA-cell, respectively. For 3DA- cell fabrication, YSZ-based cell using YSZ electrolyte and CGO-based cell using CGO/YSZ/CGO composite electrolyte were fabricated. In other words, we confirmed that 3D architecturing is available without any limitation of materials. The YSZ-based 3DA-cell and CGO-based 3DA-cell resulted in maximum power of 0.523 W and 0.931 W, which is 55 % and 76 % higher than 0.338 W of YSZ-based Planar-cell and 0.530 W of CGO-based Planar-cell at 500 °C, respectively. The output power of our pyramid-patterned fuel cells were higher than the previously reported three-dimensionally architected SOFCs. In addition, the 0.01 %/hour performance degradation rate of YSZ-based 3DA-cell was obtained through the long-term stability test under the constant current density of 0.6 A/cm² at 550 °C. As a result, it was verified that the fuel cell we fabricated has high stability and high output power than the previous results.

Keywords: Three-dimensional architecturing, Solid oxide fuel cell, Electrospray deposition, Nanoscale interlayer, Infiltration, Microscale ceramic imprinting

Student Number: 2015-30162

Contents

Abstract	i
Contents	vi
List of Tables	ix
List of Figures	x
Nomenclature	xvi
Chapter 1. Introduction	1
1.1. Introduction	1
1.2. References	9
Chapter 2. Tailoring Ceramic Membrane Structures via Polymer-Assisted Electrospray Deposition	13
2.1. Introduction	13
2.2. Experimental.....	16
2.3. Results and Discussion.....	21
2.3.1. Principles of PA-ESD process for SOFC fabrication	21
2.3.2. Microstructure control of ceramic layers for dense electrolytes	24
2.3.3. Microstructure control of ceramic layers for porous cathodes	29
2.3.4. Electrochemical performance of spray-based SOFCs	35
2.4. Conclusions	42
2.5. References	43

Chapter 3. Multiscale Electrode Architecturing Technologies via Precursor-Solution Electro spray Deposition.....	49
3.1. Introduction	49
3.2. Experimental.....	52
3.3. Results and Discussion.....	60
3.3.1. Principles of precursor-solution electro spray deposition process	60
3.3.2. Structural analysis of fabricated nanoscale interlayers.....	65
3.3.3. Electrochemical performance of fuel cells including nanoscale interlayers.....	68
3.3.4. Principles of gelation and solation via precursor-solution ESD process	73
3.3.5. Structural characteristics of conventional infiltration and ESD infiltration	76
3.3.6. Analysis of electrochemical performance of Ref-cell, CI-cell, EI-cell and HEI-cell	81
3.4. Conclusions	89
3.5. References	91
Chapter 4. Three-Dimensional Ceramic Multilayer Architectures for High-Performance Solid Oxide Fuel Cells	97
4.1. Introduction	97
4.2. Experimental.....	100
4.3. Results and Discussion.....	104

4.3.1.	3D ceramic architectures with microscale ceramic imprinting.....	104
4.3.2.	Superior power-generating performance with 3D architectures	110
4.3.3.	Microstructural and electrochemical analysis of 3D-architected SOFCs.....	118
4.4.	Conclusions	126
4.5.	References	128
Chapter 5. Conclusion		134
5.1.	Conclusion.....	134
5.2.	Future direction.....	136
Abstract (in Korean).....		139

List of Tables

Table 2.1. Detailed processing conditions of PA-ESD for each component fabrication.	20
Table 2.2. Performance comparison of anode-supported SOFCs fabricated by spray-based process.	38
Table 3.1. Processing variables used to deposit the various layers using electrospraying. T_s and t_{dep} are the sintering temperature and the deposition time, respectively.	58
Table 3.2. P_{max} , ASR_{ohm} , and ASR_{pol} of each cell at operating temperatures of 650 and 550°C. All ASR results are estimated from impedance spectra under $V_{cell} = 0.75$ V at 650 and 550°C.	70
Table 3.3. P_{max} , ASR_{ohm} , and ASR_{pol} of each cell at operating temperatures of 650 and 600°C. All results are obtained from impedance spectra under the condition of open circuit voltage (OCV) at 650 and 600°C.	84
Table 4.1. Detailed structural information of 3DA-cells and Planar-cells obtained from the 3D reconstruction technique.	121
Table 4.2. Comparison of electrochemical performance of the developed (this study) and previously reported 3D SOFC architectures.	122

List of Figures

- Figure 2.1. (a) Schematic illustrations of the PA-ESD process layout for the membrane deposition. (b) Processing flow diagram of SOFCs employing the tape lamination and the PA-ESD process. 19
- Figure 2.2. Variations in the microstructure of electrolytes during the sintering process (at 25, 100, 400, and 1350 °C) with different W_{YSZ}/W_{PVB} values. The top views of the YSZ electrolyte layer fabricated by the PA-ESD process are shown (scale bar: 2 μm). Cross-sectional SEM images at right end are represent YSZ structures after 1350 °C sintering (scale bar: 2 μm). 27
- Figure 2.3. Particle size distribution of the YSZ and YSZ slurry at $W_{YSZ}/W_{PVB} = 1, 2, \text{ and } 3.5$. The first peak on the particle size curve correspond to the primary YSZ particles, and the others are the secondary and tertiary particles, major aggregates of primary particles. The result of pristine YSZ sample, indicated by a dashed black line, is also shown. 28
- Figure 2.4. Variations in the microstructure of the LSC cathodes during the sintering process (at 25, 200, 400, and 950 °C) with different W_{LSC}/W_{PVP} values. The top views of the LSC cathode layer fabricated by the PA-ESD process are shown (scale bar: 2 μm). Cross-sectional SEM images at right end are represent LSC structures after 950 °C sintering (scale bar: 1 μm). 32
- Figure 2.5. Particle size distribution of the LSC and LSC slurry at

$W_{\text{LSC}}/W_{\text{PVP}} = 0.5, 1, \text{ and } 2$. The first peak on the particle size curve correspond to the primary LSC particles, and the others are the secondary and tertiary particles, major aggregates of primary particles. The result of pristine LSC sample, indicated by a dashed black line, is also shown. 33

Figure 2.6. Electrochemical characterization of an anode-supported SOFC including the spray-deposited LSC cathode layer with different $W_{\text{LSC}}/W_{\text{PVP}}$ values. (a) The $I-V-P$ curves and (b) EIS results measured at 650 °C in different cell voltages. 34

Figure 2.7. A cross-sectional SEM image of the SOFC fabricated by the optimized PA-ESD process. A whole structure composed of anode, anode functional, electrolyte, barrier, cathode functional, and cathode layers are presented. Note that these are microstructure images observed by fracturing the PA-ESD cell after the cell test. 39

Figure 2.8. Electrochemical characterization of an anode-supported SOFC fabricated by the optimized PA-ESD process. (a) The $I-V-P$ curves and (b) EIS results at different operation temperature. For the EIS curves, the inset shows the magnified view of high-temperature results. 40

Figure 2.9. Long-term test results of an anode-supported SOFC fabricated by the optimized PA-ESD process. (a) Cell voltage measurement under 0.4 A/cm² current at 650 °C and (b) $I-V-P$ curves at 0 and 100 h. 41

Figure 3.1. Schematic illustration of the fabrication process for the three different SOFCs using PLD and ESD techniques: (a) Ref, (b) nAL,

and (c) nCFL cells.	59
Figure 3.2. Results of the structural analysis of LSC and LSC-CeO ₂ deposited by precursor-solution electrospray method and sintered at 950°C for 1 h. (a) XRD patterns of two precursor solutions indexed to LSC and CeO ₂ . (b) Low- and high-magnification surface SEM images of the deposited (top) LSC nAL and (bottom) LSC-CeO ₂ nCFL. All scale bars correspond to 100 nm.	63
Figure 3.3. Surface SEM images showing microstructures of as-sintered LSC layer fabricated by the precursor-solution electrospray method with (a) different nozzle-tip diameters and (b) applied voltages.	64
Figure 3.4. Cross-sectional SEM images and schematic illustrations of various interlayer structures between the BL/EL and mCFL: (a) Ref, (b) nAL, and (c) nCFL cells. All scale bars correspond to 300 nm.	67
Figure 3.5. Comparison of the <i>I-V-P</i> curves for the three different cells (Ref, nAL, and nCFL cell) measured at (a) 650 and (b) 550°C.	71
Figure 3.6. Comparison of AC impedance spectra of the three different cells (Ref, nAL, and nCFL cell) measured at (a) 650 and (b) 550°C and a cell voltage of 0.75 V.	72
Figure 3.7. Schematics of the principles in sol-to-gel and gel-to-sol reversible reaction of humidification assisted precursor-solution electrospray deposition process.	75
Figure 3.8. Schematics, section-view SEM images and top-view SEM images under the various conditions of humidification after precursor-solution deposition.	79
Figure 3.9. SEM images and schematics of infiltrated and sintered SSC	

precursor-solution into the porous alumina structure via (a) conventional infiltration process, (b) ESD infiltration process without humidification and (c) humidification assisted ESD infiltration process.	80
Figure 3.10. Schematic illustration of fabrication of four different SOFCs multiple infiltration processes (a) Ref-, (b) CI-, (c) EI- and (d) HEI-cells.	85
Figure 3.11. XRD results of as-sintered LSCF powder and SSC precursor-solution at 1050 °C for 1 h and 1000 °C for 1 h, respectively.	86
Figure 3.12. Electrochemical characteristics of four different cells (Ref-, CI-, EI- and HEI- cell). (a) <i>I-V-P</i> curves at 650°C, (b) impedance spectra under the condition of OCV at 650°C.	87
Figure 3.13. SEM images of (a) Ref-cell, (b) CI-cell, (c) EI-cell and (d) HEI-cell after cell test.	88
Figure 4.1. Fabrication of 3D ceramic multilayer architectures. Schematic illustrations of the (a) preparation of PUA mold from a PDMS replica, (b) molding process used to fabricate a 3D NiO–YSZ substrate architecture, and (c) implementation of the multilayer thin-film deposition process. (d) Snapshots and SEM images of a PUA mold (left), as-imprinted NiO–YSZ anode tapes (top-right) and as-annealed NiO–YSZ anode tapes (bottom-right). (e) Variations of the elastic modulus of anode tapes with temperature.	108
Figure 4.2. Schematics and SEM images of as-imprinted and as-annealed states of prism- and line-shaped NiO–YSZ structures. All scale bars	

correspond to 10 μm	109
Figure 4.3. (a) Schematic illustration (left) and SEM images (right) of a YSZ-based 3DA-cell. The inset show the magnified SEM image of a pyramidal structure. (b) Potential and power density curves of 3DA-cells and Planar-cells at three different operating temperatures.	113
Figure 4.4. (a) Schematic and (b) SEM images of an YSZ-based Planar-cell.	114
Figure 4.5. Recorded test results of a YSZ-based 3DA-cell during a period of 50 h. (a) Measured cell potential in the presence of a constant current load of 0.6 A at 550 $^{\circ}\text{C}$ and (b) cell potential and power density curves at 0 and 50 h.	115
Figure 4.6. (a) Schematic illustration (left) and SEM images (right) of a CGO-based 3DA-cell. The inset show the magnified SEM image of a pyramidal structure. (b) Potential and power density curves of 3DA-cells and Planar-cells at three different operating temperatures.	116
Figure 4.7. (a) Schematic and (b) SEM images of a CGO-based Planar-cell.	117
Figure 4.8. (a) 3D reconstructed cell structure for one repeating unit of the compartment of a YSZ-based 3DA-cell. (b) Measured impedance spectra of 3DA-cell and Planar-cell at the cell potential of 0.75 V at operating temperature of 500 $^{\circ}\text{C}$. The calculated structural parameters of 3DA-cells and Planar-cells are obtained with the use of the 3D reconstruction technique. (c) Arrhenius plot of the ASR_{ohm} and ASR_{pol} of 3DA-cells and Planar-cells at various operating temperatures.	123
Figure 4.9. Comparison of the total power output in this work compared to	

the previously reported 3D SOFC architectures as a function of temperature. 124

Figure 4.10. Comparison of the maximum power density in this work compared to the previously reported 3D SOFC architectures as a function of temperature. 125

Nomenclature

V_n	Allied voltage	[V]
γ	Solvent surface tension	[N/m]
ε_0	Permittivity of free space	[F/m]
θ_0	Cone half-angle	[°]

Chapter 1. Introduction

1.1. Introduction

Three-dimensionally architected multiscale structures exist in intriguing morphologies to perform multiple functions in nature¹⁻⁵. In general, they are composed of microscale structures with functions of mechanical pivot and nanoscale structures with active performances, which satisfy both mechanical stability and functionality due to their structural uniqueness from wide range of scale^{4,6}. Examples can be found in the adhesion features of gecko feet^{7,8}, the wetting properties of spider silk^{9,10}, the self-cleaning effect of lotus leaves^{11,12} and anti-reflection characteristics of moth's eyes^{13,14}. In recent years, researches are being conducted to apply those three-dimensional multiscale structures exhibiting interesting functions to optics^{15,16}, sensors^{17,18} and energy devices¹⁹⁻²¹. Above all, the multiscale structures applied to the energy systems have difficulties in meeting stability, scalability and cost-effectiveness as well as high-performance and functionality. Therefore, challenging researches are still being tried.

Solid oxide fuel cell (SOFC), one of the most promising energy generation devices, affords various advantages such as low pollutant production, the versatility of fuel usage, high efficiency of energy conversion²²⁻²⁵. However, due to its high operating temperature (generally,

above 700 °C), there exist several problems such as high system maintenance cost, difficulty of material compatibility, difficulty in application to portable devices and chemical/mechanical degradation^{26–28}. Therefore, lowering operating temperature is one of the key issues in SOFCs²⁹. To solve this problem, various researches have been conducted to develop electrolyte materials with good ionic conductivity and electrode with high catalytic activity at low-temperature. However, the low durability of new materials that are helpful to low-temperature operation has hampered the long-term stable operation of fuel cells. Thus, in order to satisfy both stability and performance issues, structural development has been required, and studies have been performed in recent years to apply three-dimensional multiscale structures.

Multi-layer structures and infiltration applied structures are well-known multiscale electrode structures of SOFC. Multi-layer electrode structures are fabricated by inserting functional layer such as electrolyte/electrode composite layer or nanoscale interlayer into microscale electrode^{30,31}. However, it is difficult to fabricate uniform sub-micron thin films when using non-vacuum processes. On the other hand, the infiltration process facilitates the fabrication of multiscale electrodes by using precursor-solution^{32,33}, but it has limitations such as non-continuous process and difficulties of uniformity in large area.

Meanwhile, micro-SOFC using microelectromechanical systems (MEMS) process on Si substrate is a representative method to fabricate three-dimensionally structured electrolyte^{34–36}. In the recently published micro-SOFC results, surface architecturing of cup³⁷, crater³⁸ and pyramid³⁹

performed before the fabrication of the ceramic layer. However, micro-SOFCs suffer from drawbacks such as cell size limitation comes from brittleness of freestanding ceramic membrane and quick thermal degradation in terms of stability caused by Pt mainly used as an electrode^{39,40}. From the above, it is verified that the representative fabrication processes of multiscale SOFC have their own technical issues. Accordingly, demands for advanced fabrication process to overcome the remained issues have been brought up.

In this thesis, we have developed advanced multiscale electrode architecturing technologies and novel three-dimensional interface architecturing technologies that overcome the limitations of previously reported researches for the implementation of LT-SOFC. We have optimized the technology of fabricating ceramic thin films with non-vacuum processes through powder-suspension electrospray deposition and precursor-solution electrospray deposition, which are advantageous for commercialization. We also reported a novel infiltration method using continuous processes. Finally, by combining ceramic imprinting technology and thin film deposition processes, we have fabricated the fuel cells with the highest performance and stability among the three-dimensionally architected SOFCs so far reported.

In *Chapter 2*, we propose methods to optimize the structure of each component of SOFCs using a powder-suspension electrospray deposition process and confirm the stable operation of the fuel cell at high operating temperature. The electrospray deposition process has several advantages over a wide range of deposition thickness, facile control of microstructure,

and less influence on surface defects compared to the screen printing method, one of the traditional fuel cell fabrication methods. The focus of our research was on the morphology of the structure after sintering depending on the weight ratio of the ceramic powder and the polymer binder in the suspension during the electrospray deposition process. A polyvinyl butyral polymer binder was used for the fabrication of a dense electrolyte layer to block the gas permeation between the anode and the cathode, and a polyvinylpyrrolidone polymer binder was used for the cathode layer to be porous for the gas flow. The deposited cathode layer was uniformly dispersed under the condition of 1:1 weight ratio of the cathode powder and the polymer binder. In addition, we figured out through the particle size analyzer and scanning electron microscope analysis that the dispersion status of the suspension could affect not only the as deposited structure but also the sintered. As a result, a fuel cell with an optimized electrolyte and cathode structure resulted in a peak power density of 805 mW/cm^2 at an operating temperature of $650 \text{ }^\circ\text{C}$. Also, the degradation rate was 1.5 % for 100 hours at the condition of a constant current density of 0.4 A/cm^2 at $650 \text{ }^\circ\text{C}$, which verified that the performance in long-term measurement was maintained.

In *Chapter 3*, we developed two different multiscale electrode architecturing technologies, a ceramic thin film fabrication technology and a novel infiltration technology, via a precursor-solution electrospray deposition process. First, we fabricated ceramic thin films using a precursor-solution electrospray deposition process and applied them as

nanoscale interlayers between the SOFC electrolyte and the cathode layer. In our previous study, we have optimized a micro-thick structure using a powder-suspension electro-spray deposition process, while subsequent researches have fabricated thin film structures under micron thickness using a precursor-solution electro-spray deposition process. Previously reported precursor-solution electro-spray deposition researches have been difficult to fabricate thin films and control microstructures due to diameter of nozzle tip over 100 μm , high flow rates and substrate temperature as high as 200 $^{\circ}\text{C}$. In particular, the stable spray condition of the precursor solution using deionized water as a solvent, which has three times higher surface tension than ethyl alcohol, was established by using silica nozzle with 8 μm tip diameter. Nano adhesion layer (nAL) and nano cathode functional layer (nCFL) were fabricated, and the nAL-cell and nCFL-cell were prepared by inserting nanoscale interlayer between electrolyte layer and cathode layer of SOFCs. We also fabricated Ref-cell without nanoscale interlayer and evaluated the performance of all three cells. As a result, the maximum power density of nCFL-cell increased by 18 % and 13 % compared to nAL-cell and Ref-cell at 650 $^{\circ}\text{C}$, respectively. Those results were derived from two reasons: (i) the increase of the oxygen ion transport pathways due to the better adhesion by the nanoscale interlayer inserted between the electrolyte layer and the cathode layer; and (ii) the maximization of oxygen reduction reaction (ORR) sites by smaller particle size of nanoscale interlayer. Second, a novel strategy of infiltration process was developed to enhance the performance of SOFC by improving the microstructure of

electrode. The infiltration process, which is mainly used for SOFC electrodes, is a method of infiltrating and sintering a precursor-solution of a highly catalytic active material into a porous skeleton structure composed of materials having high electronic conductivity and ionic conductivity. The sintered precursor-solution is formed as thin films or homogeneous nanoparticles on a porous skeleton structure to architecture multiscale structures. Since such a wide range of materials can be selected, it is a representative process capable of manufacturing a high stable and high performance electrode at an effective cost. The traditional infiltration process was a simple method of dropping the precursor solution onto the electrode using a micropipette. However, there are issues that are difficult to infiltrate uniformly into the entire surface of the electrode and difficult to control the flow of the infiltrated precursor-solution. In this chapter, a novel infiltration process was developed to uniformly deposit the precursor-solution onto the electrode using the precursor-solution electrospray deposition process and control the infiltration rate of the precursor-solution according to the humidity. The precursor-solution is physically gelled in nanoscale spherical structures at the tip of the nozzle during electrospray deposition, and is deposited as dendrite structures on the electrode. After deposition process, the dendrite structured precursor-gel permeates into the porous electrode through the humidification process. The fuel cell with our new infiltration process resulted in higher maximum powder density of 15 % and 215 % compared to the conventionally infiltrated fuel cell and the non-infiltrated fuel cell at 650 °C, respectively. The significant increase of

performance can be explained by the improvement of the electrode reaction mechanism such as increase of electrochemical reaction sites through the sintering of uniformly infiltrated precursor-solution by humidification.

In *Chapter 4*, we demonstrate a micro-ceramic imprinting technology that combines a micro pattern imprinting and a tape lamination process, which is a method of manufacturing a SOFC anode support, and apply it to fabricate three-dimensional SOFCs using thin film deposition processes. It has been well known that the microscale surface patterning of ceramic materials is difficult because of their fragile properties. In this chapter, to solve those problems, we developed pyramid patterned anode support by lamination process of polymer-ceramic composite anode tapes and polymer mold with micro pattern. In addition, we used sputtering and pulsed laser deposition process to deposit electrolyte and cathode layer of full test cells. The cells with a flat structure without a PUA polymer mold in the lamination process and a three-dimensional pyramid structure were denoted as Planar-cell and 3DA-cell, respectively. For 3DA- cell fabrication, YSZ-based cell using YSZ electrolyte and CGO-based cell using CGO/YSZ/CGO composite electrolyte were fabricated. In other words, we confirmed that 3D architecturing is available without any limitation of materials. In addition, 3D reconstruction of Planar-cells and 3DA-cells were conducted using focused ion beam technology and Avizo program for electrochemical analysis of fuel cells. The YSZ-based 3DA-cell and CGO-based 3DA-cell resulted in maximum power of 0.523 W and 0.931 W, which is 55 % and 76 % higher than 0.338 W of YSZ-based Planar-cell and

0.530 W of CGO-based Planar-cell at 500 °C, respectively. The output power of our pyramid-patterned fuel cells were higher than the previously reported three-dimensionally architected solid oxide fuel cells. In addition, the performance degradation rate of 0.01 %/hour was obtained through the long-term stability test under the constant current density of 0.6 A/cm² at 550 °C. As a result, it was verified that the fuel cell we fabricated has high stability and high output power than the previous results.

1.2. References

1. Hamilton, W.; Seger, J.; Michod, R. E.; Levin, B. R.; Axelrod, R.; Tanese, R. Adhesive force of a single gecko foot-hair. *Nature* **405**, 671–702 (2000).
2. Bhushan, B. Biomimetics: Lessons from nature - an overview. *Philosophical Transactions of the Royal Society A: Mathematical, Physical and Engineering Sciences* **367**, 1445–1486 (2009).
3. Feng, L.; Li, S.; Li, Y.; Li, H.; Zhang, L.; Zhai, J.; Song, Y.; Liu, B.; Jiang, L.; Zhu, D. Super-hydrophobic surfaces: From natural to artificial. *Advanced Materials* **14**, 1857–1860 (2002).
4. Bae, W. G.; Kim, H. N.; Kim, D.; Park, S. H.; Jeong, H. E.; Suh, K. Y. 25th anniversary article: Scalable multiscale patterned structures inspired by nature: The role of hierarchy. *Advanced Materials* **26**, 675–699 (2014).
5. Gao, X.; Yan, X.; Yao, X.; Xu, L.; Zhang, K.; Zhang, J.; Yang, B.; Jiang, L. The dry-style antifogging properties of mosquito compound eyes and artificial analogues prepared by soft lithography. *Advanced Materials* **19**, 2213–2217 (2007).
6. Jeong, H. E.; Lee, J.-K.; Kim, H. N.; Moon, S. H.; Suh, K. Y. A nontransferring dry adhesive with hierarchical polymer nanohairs. *Proceedings of the National Academy of Sciences* **106**, 5639–5644 (2009).
7. Lee, H.; Lee, B. P.; Messersmith, P. B. A reversible wet/dry adhesive inspired by mussels and geckos. *Nature* **448**, 338–341 (2007).
8. Geim, A. K.; Dubonos, S. V.; Grigorieva, I. V.; Novoselov, K. S.; Zhukov, A. A.; Shapoval, S. Y. Microfabricated adhesive mimicking gecko foot-hair. *Nature Materials* **2**, 461–463 (2003).
9. Zheng, Y.; Bai, H.; Huang, Z.; Tian, X.; Nie, F. Q.; Zhao, Y.; Zhai, J.; Jiang, L. Directional water collection on wetted spider silk. *Nature* **463**, 640–643 (2010).
10. Bai, H.; Ju, J.; Zheng, Y.; Jiang, L. Functional fibers with unique wettability inspired by spider silks. *Advanced Materials* **24**, 2786–2791 (2012).

11. Cheng, Y. T.; Rodak, D. E.; Wong, C. A.; Hayden, C. A. Effects of micro- and nano-structures on the self-cleaning behaviour of lotus leaves. *Nanotechnology* **17**, 1359–1362 (2006).
12. Blossey, R.; Scientific, C. Self-cleaning surfaces — virtual realities. 301–306 (2003).
13. Huang, Y. F.; Chattopadhyay, S.; Jen, Y. J.; Peng, C. Y.; Liu, T. A.; Hsu, Y. K.; Pan, C. L.; Lo, H. C.; Hsu, C. H.; Chang, Y. H.; Lee, C. S.; Chen, K. H.; Chen, L. C. Improved broadband and quasi-omnidirectional anti-reflection properties with biomimetic silicon nanostructures. *Nature Nanotechnology* **2**, 770–774 (2007).
14. Forberich, K.; Dennler, G.; Scharber, M. C.; Hingerl, K.; Fromherz, T.; Brabec, C. J. Performance improvement of organic solar cells with moth eye anti-reflection coating. *Thin Solid Films* **516**, 7167–7170 (2008).
15. Kang, D.; Pang, C.; Kim, S. M.; Cho, H. S.; Um, H. S.; Choi, Y. W.; Suh, K. Y. Shape-controllable microlens arrays via direct transfer of photocurable polymer droplets. *Advanced Materials* **24**, 1709–1715 (2012).
16. Jeong, K.; Kim, J.; Lee, L. P. Biologically inspired artificial compound eyes. *Science* **312**, 557–561 (2006).
17. Kang, D.; Pikhitsa, P. V.; Choi, Y. W.; Lee, C.; Shin, S. S.; Piao, L.; Park, B.; Suh, K. Y.; Kim, T. II; Choi, M. Ultrasensitive mechanical crack-based sensor inspired by the spider sensory system. *Nature* **516**, 222–226 (2014).
18. Pang, C.; Lee, G. Y.; Kim, T. II; Kim, S. M.; Kim, H. N.; Ahn, S. H.; Suh, K. Y. A flexible and highly sensitive strain-gauge sensor using reversible interlocking of nanofibres. *Nature Materials* **11**, 795–801 (2012).
19. Cho, H.; Moon Kim, S.; Sik Kang, Y.; Kim, J.; Jang, S.; Kim, M.; Park, H.; Won Bang, J.; Seo, S.; Suh, K. Y.; Sung, Y. E.; Choi, M. Multiplex lithography for multilevel multiscale architectures and its application to polymer electrolyte membrane fuel cell. *Nature Communications* **6**, 1–8 (2015).
20. Jang, S.; Kang, J. S.; Lee, J. K.; Kim, S. M.; Son, Y. J.; Lim, A.; Cho, H.; Kim, J.; Jeong, J.; Lee, G.; Sung, Y. E.; Choi, M. Enhanced light

- harvesting in mesoscopic solar cells by multilevel multiscale patterned photoelectrodes with superpositioned optical properties. *Advanced Functional Materials* **26**, 6584–6592 (2016).
21. Kil, E. H.; Choi, K. H.; Ha, H. J.; Xu, S.; Rogers, J. A.; Kim, M. R.; Lee, Y. G.; Kim, K. M.; Cho, K. Y.; Lee, S. Y. Imprintable, bendable, and shape-conformable polymer electrolytes for versatile-shaped lithium-ion batteries. *Advanced Materials* **25**, 1395–1400 (2013).
 22. Minh, N. Q. Ceramic Fuel Cells. *Journal of the American Ceramic Society* **76**, 563–588 (1993).
 23. Park, S. Direct oxidation of hydrocarbons in a solid oxide fuel cell. *Nature* **404**, 265–267 (2000).
 24. Chen, Y.; Zhang, Y.; Lin, Y.; Yang, Z.; Su, D.; Han, M.; Chen, F. Direct-methane solid oxide fuel cells with hierarchically porous Ni-based anode deposited with nanocatalyst layer. *Nano Energy* **10**, 1–9 (2014).
 25. Ormerod, R. M. Solid oxide fuel cells. *Chemical Society Reviews* **32**, 17–28 (2003).
 26. Adler, S. B. Factors governing oxygen reduction in solid oxide fuel cell cathodes. *Chemical Reviews* **104**, 4791–4844 (2004).
 27. Singhal, S. Advances in solid oxide fuel cell technology. *Solid State Ionics* **135**, 305–313 (2000).
 28. Shai, Z.; Hale, S. M. A high-performance cathode for the next generation of solid-oxide fuel cells. *Nature* **431**, 170–174 (2004).
 29. Wachsman, E. D.; Lee, K. T. Lowering the temperature of solid oxide fuel cells. *Science* **334** 935–939 (2011).
 30. Noh, H. S.; Yoon, K. J.; Kim, B. K.; Je, H. J.; Lee, H. W.; Lee, J. H.; Son, J. W. The potential and challenges of thin-film electrolyte and nanostructured electrode for yttria-stabilized zirconia-base anode-supported solid oxide fuel cells. *Journal of Power Sources* **247**, 105–111 (2014).
 31. Park, S. Y.; Ji, H. Il; Kim, H. R.; Yoon, K. J.; Son, J. W.; Kim, B. K.; Je, H. J.; Lee, H. W.; Lee, J. H. Structural optimization of (La, Sr)CoO₃-based

- multilayered composite cathode for solid-oxide fuel cells. *Journal of Power Sources* **228**, 97–103 (2013).
32. Vohs, J. M.; Gorte, R. J. High-performance SOFC cathodes prepared by infiltration. *Advanced Materials* **21**, 943–956 (2009).
 33. Ding, D.; Li, X.; Lai, S. Y.; Gerdes, K.; Liu, M. Enhancing SOFC cathode performance by surface modification through infiltration. *Energy and Environmental Science* **7**, 552–575 (2014).
 34. Tsuchiya, M.; Lai, B. K.; Ramanathan, S. Scalable nanostructured membranes for solid-oxide fuel cells. *Nature Nanotechnology* **6**, 282–286 (2011).
 35. Huang, H.; Nakamura, M.; Su, P.; Fasching, R.; Saito, Y.; Prinz, F. B. High-performance ultrathin solid oxide fuel cells for low-temperature operation. *Journal of The Electrochemical Society* **154**, B20 (2007).
 36. Kwon, C. W.; Son, J. W.; Lee, J. H.; Kim, H. M.; Lee, H. W.; Kim, K. B. High-performance micro-solid oxide fuel cells fabricated on nanoporous anodic aluminum oxide templates. *Advanced Functional Materials* **21**, 1154–1159 (2011).
 37. Su, P. C.; Chao, C. C.; Shim, J. H.; Fasching, R.; Prinz, F. B. Solid oxide fuel cell with corrugated thin film electrolyte. *Nano Letters* **8**, 2289–2292 (2008).
 38. Kim, Y. B.; Gür, T. M.; Kang, S.; Jung, H. J.; Sinclair, R.; Prinz, F. B. Crater patterned 3-D proton conducting ceramic fuel cell architecture with ultra thin Y:BaZrO₃ electrolyte. *Electrochemistry Communications* **13**, 403–406 (2011).
 39. An, J.; Kim, Y. B.; Park, J.; Gür, T. M.; Prinz, F. B. Three-dimensional nanostructured bilayer solid oxide fuel cell with 1.3 W/cm² at 450 °C. *Nano Letters* **13**, 4551–4555 (2013).
 40. Chao, C.-C.; Hsu, C.-M.; Cui, Y.; Prinz, F. B. Improved solid oxide fuel cell performance with nanostructured electrolytes. *ACS Nano* **5**, 5692–5696 (2011).

Chapter 2.

Tailoring Ceramic Membrane Structures via Polymer-Assisted Electrospray Deposition

2.1. Introduction

Solid oxide fuel cells (SOFCs) consist of ceramic membranes and are promising power-generating electrochemical devices that operate in the high-temperature region (generally, 600 to 850 °C) because of their high energy efficiencies, low pollutant emissions, and fuel flexibilities¹⁻⁴. However, advances in the development and commercialization of SOFCs still face many obstacles because of the inherent limitations of the materials (multiple phases, multiple components, brittleness, hardness)^{5,6} as well as the limitations of ceramic processing (dispersion, molding, drying, high-temperature densification)⁷. In addition, the multi-layered membrane configuration used, which consists of porous ceramic anodes and cathodes and a dense ceramic electrolyte, adds to the technological hurdles. Most electrochemical reactions between gas species and charge carriers (electrons and ions) at both electrodes require high catalytic activity, mixed ionic-electronic conductivity, and porosity, whereas the electrolyte requires pure ionic conductivity and gas tightness for perfect electronic insulation and sufficient difference in the oxygen partial pressure, respectively⁸. Such

complex controls and considerations of materials and microstructures are necessary to fabricate robust and high-performing SOFCs. The simultaneous control of porosity and interfacial strength in heterogeneous ceramic-metallic materials is particularly challenging⁹, since different ceramic materials with different thermo-mechanical properties are used as multi-layered components.

Over the last few decades, various conventional powder-based and wet-chemical-based ceramic processes have been used to fabricate the unique multi-layered membrane structures in SOFCs¹⁰⁻¹³. For example, screen printing has been widely used for the fabrication of electrolyte and electrode structures because of its renowned versatility and reproducibility. However, the screen printing process involves precisely controlled dispersion, drying and leveling steps of the ceramic powder on a flat substrate, and the difficulties of such processes make it impossible for researchers to investigate advanced membrane features (such as ultra-thin thickness and controlled pore structure) under various substrate conditions¹⁴. Recently, much progress has been made in controlling ceramic materials and their microstructure, interfacial strength, and thickness by the use of alternative deposition methods such as vacuum-based techniques^{15,16}, solution coating^{17,18}, and powder spraying¹⁹⁻²². Many researchers have demonstrated that vacuum- and solution-based coating methods can be used to fabricate ultra-thin and ultra-dense electrolytes and highly active porous cathode layers precisely, but these methods are limited in productivity and versatility. In contrast, powder spraying technique offers some benefits related to productivity and versatility but has several weaknesses associated

with coating precision (e.g., limitations of microstructure control, thin thickness, poor step coverage). Based on these features, various powder spray methods such as thermal^{19,20}, electrostatic²¹, and ultrasonic methods²² have been suggested for the construction of each SOFC component, but the processes still need to be optimized to account for microstructure and interfacial strength of heterogeneous multi-layered structures before they can be used to produce high-performance cells.

In this chapter, we developed a versatile and robust process for the fabrication of heterogeneous multi-layered ceramic membrane structures in anode-supported SOFCs, which we have named polymer-assisted electrospray deposition (PA-ESD). Through this method, we successfully fabricated thin, dense electrolyte layers and crack-free porous cathode layers, which are critical components of SOFCs. Their structures were mainly controlled by the type and amount of polymer additive, and we obtained high-performance spray-deposition-based SOFCs as a result.

2.2. Experimental

Preparation of tape laminated anode substrates

Fine NiO (Sumitomo) and 8 mol% Y₂O₃-ZrO₂ (YSZ, Tosho; particle size $d_{50} = 250$ nm) powders were employed for the preparation of the anode tape (NiO/YSZ = 56:44 wt%), with polyvinyl butyral (PVB, Sigma-Aldrich) and dibutyl phthalate (Sigma-Aldrich) being used as a binder and a plasticizer, respectively. Two different tape sheets were prepared: (i) an anode layer in which poly(methyl methacrylate) (PMMA, Sunjin Chemical) was used as a pore-forming additive, and (ii) an anode functional layer (AFL) without PMMA. Multi-layered anode structures were made by stacking a prepared AFL tape and seven sheets of anode tapes, and then laminating the stack to form an anode green (unfired) substrate (thickness = 1 mm) for PA-ESD.

Fabrication of sprayed electrolyte and cathode layers

We designed and optimized the compositions of the electrolyte, barrier, cathode functional layer (CFL), and cathode slurries for subsequent PA-ESD as follows. The electrolyte and barrier layer slurries were prepared by mixing YSZ and Ce_{0.9}Gd_{0.1}O_{1.95} (CGO, Solvay; particle size $d_{50} = 400$ nm), respectively, with PVB binder. A CFL slurry consisting of La_{0.6}Sr_{0.4}CoO_{3- δ} (LSC, Kceracell; particle size $d_{50} = 450$ nm) and CGO at a weight ratio of

1:1 was made using polyvinyl pyrrolidone (PVP, Sigma-Aldrich) as a binder. The cathode slurry was also prepared by combining LSC powder and PVP. All slurries were prepared by mixing these composite powders with ethanol and ball milling the mixtures for 24 h. Particle sizes and distributions of the powders in ethanol were measured by laser diffraction (LS230, Beckman Coulter). As shown in **Figure 2.1a**, the electrospray system consisted of a high-voltage DC source (NanoNC), a microsyringe needle (NanoNC), and a pump controller (KD Scientific). The prepared ceramic slurry was fed into the microsyringe needle, and a direct-current voltage was applied to the microsyringe to generate a uniform cone-jet spray. The distance between the substrate and the nozzle was fixed at 6 cm, and the flow rate of the composite solution was fixed at 0.3 ml/h. The details of the PA-ESD conditions are summarized in **Table 2.1**. The processing flow of cell fabrication in **Figure 2.1b** can be described as follows. First, the YSZ electrolyte slurry was deposited on the green NiO–YSZ substrate (dimensions: 2 cm × 2 cm) using the PA-ESD process at a substrate temperature (T_{sub}) of 25 °C, followed by firing at 1350 °C for 3 h in air. After that, a CGO barrier layer was deposited over 1 h followed by sintering at 1250 °C for 2 h in air. Then, the LSC–CGO CFL and the LSC cathode layer (dimensions: 1 cm × 1 cm) were formed via PA-ESD at $T_{\text{sub}} = 80$ °C, followed by sintering in air for 1 h at 950 °C.

Electrochemical measurements and structural characterization

During cell operation, air was supplied as the oxidant and 3% humidified H₂ was supplied as the fuel, with each flowing at a rate of 200 sccm. The open-circuit voltages (OCVs) and electrochemical performances of the SOFCs were investigated by analyzing the current-potential-power ($I-V-P$) measurements and electrochemical impedance spectroscopy (EIS) obtained with an electrochemical analyzer (IviumStat, Ivium Technologies). The EIS measurements were performed at 500 to 650 °C (at 50 °C intervals) across a wide frequency range (from 10⁶ to 10⁻¹ Hz) and at different bias voltages. The microstructures of all SOFC components were examined with a scanning electron microscope (SEM, Inspect F50, FEI) before and after the cell-performance tests.

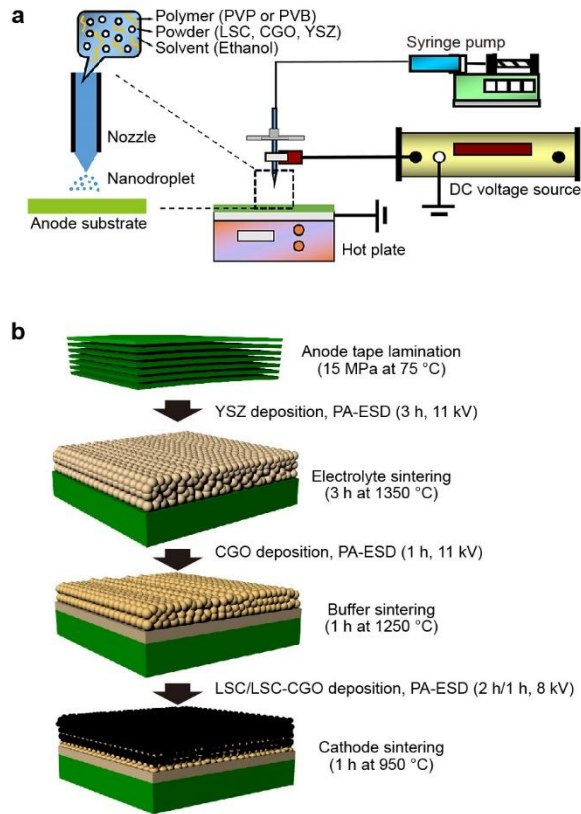


Figure 2.1. (a) Schematic illustrations of the PA-ESD process layout for the membrane deposition. (b) Processing flow diagram of SOFCs employing the tape lamination and the PA-ESD process.

Component (Material)	Solid loading (wt%)	Polymer	Spray voltage (kV)	Deposition time (h)	Nozzle-to-substrate distance (cm)	Flow rate of slurry (ml/h)
Electrolyte (YSZ)	2	PVB (2 wt%)	11	3	6	0.3
Barrier layer (CGO)	2	PVB (2 wt%)	11	1	6	0.3
CFL (LSC–CGO)	5	PVP (5 wt%)	8	1	6	0.3
Cathode (LSC)	10	PVP (10 wt%)	8	2	6	0.3

Table 2.1. Detailed processing conditions of PA-ESD for each component fabrication.

2.3. Results and Discussion

2.3.1. Principles of PA-ESD process for SOFC fabrication

In a general electrostatic spray system, shown in **Figure 2.1a**, the high electric field and imbalance of charge result in a liquid jet when the repulsive force exceeds the surface tension of the solvent. The sprayed droplets become smaller through the interactions of charge repulsion and solvent evaporation, and the small charged droplets are deposited on the target substrate along the electric field²³. Since these process features offer a versatile setting for the preparation of a high-quality layered ceramic membrane, many researchers have examined the structural variations that can be obtained by changing the spray processing parameters (flow rate, voltage, and substrate temperature)²⁴⁻²⁷. However, the general electrostatic spray system lacks the advanced capability to tailor the microstructure of the deposited ceramic layer to generate the dense, thin, or porous components of a SOFC. The formation of an inherent dendritic structure and the absence of a particle packing step can severely limit the applicability of the technique. As a result, there have hardly been any advances in the technology related to the electrospray deposition of ceramic membrane layers.

PA-ESD is based on the conventional electrospray process, but it is designed for the versatile and robust fabrication of SOFC structures, which consist of heterogeneous multi-layered ceramic membranes. In addition, it

has the advantages of an aerosol process, making it suitable for use on a curved substrate and in continuous processes because the deposition takes place without contact with the substrate. Because the required structural features can only be obtained by precise control of the morphologies and interfacial strengths of the ceramic powders, our PA-ESD process combines the general electrospray procedure with advanced powder engineering (i.e., fluidic- and solid-state controls) for dispersion, drying, and packing controls based on polymeric interactions. In this study, we first focused on the fluid-state parameters (e.g., vapor pressure, solvent surface tension, solvent and polymer fractions) to prevent the deposited nanodroplets from drying, as this is one of the most critical causes of defects and inhomogeneity during film deposition²⁸. To form enough liquid for redistribution and rearrangement of the deposited particles, we introduced a solvent and polymer structure to extend the capillary and funicular states during the electrospray drying process. Such polymer-particle composite states within a liquid provide many opportunities to control the powder microstructure, allowing one to achieve things such as the creation of either a porous or dense final product or to prevent the formation of film defects²⁹. Solid-state control was also applied to ensure the ceramic microstructure and interfacial strength of the multi-layered SOFCs. In addition to ensuring strong adhesion between the substrate and the deposited particles, the polymers also helped to form uniform arrangements of particles during the drying and annealing processes³⁰. The dispersion states of the slurries were dependent on the amount of polymer binder used, and the morphologies of the annealed particles were

determined by the polymer additive³¹⁻³³. Depending on the slurry viscosity and spraying conditions, any suitable polymer can be selected; in the study reported here, we used PVB and PVP for the electrolyte and cathode layers, respectively. In the following sections, we will show how these principles were applied so that the multi-layered ceramic materials could be controlled to exhibit dense or porous microstructures for SOFCs.

2.3.2. Microstructure control of ceramic layers for dense electrolytes

Since the OCV and ohmic resistance of a cell primarily originate from the difference in the oxygen partial pressures of the electrodes and the thickness of the electrolyte, respectively⁵, the SOFC electrolyte must form a dense, gas-impermeable thin film. To fabricate such a dense, thin electrolyte layer via the PA-ESD process, we chose PVB, which was also used as a binder for the anode green body^{34,35}, as the polymer binder of the YSZ slurry for the following reasons. First, the homogeneous polymer structure of PVB in the anode body and the YSZ film provided sufficient interfacial strength during film formation, which was critical in achieving the controlled, vertically directed densification of the electrolyte film. Second, it is known that the steric stabilization of ceramic particles can be achieved by the polymeric adsorption of the PVB chains³⁴⁻³⁶, and that the dispersion state is changed by the amount of the polymer used. In addition, the glass-transition temperature (T_g) of PVB is very low (~ 80 °C)³⁷, allowing the sprayed YSZ–PVB composite to rearrange during the annealing process, resulting in a well-packed and homogeneous film structure. Therefore, we expected to be able to increase the packing density of the annealed YSZ structures by adjusting the amount of PVB used.

We therefore examined variations in the ceramic microstructure as a function of the amount of PVB additive used. Remarkably significant control of the dense ceramic microstructure was attained when the polymer additives were incorporated together with the optimized fluid-state spray parameters. **Figure 2.2** shows the changes in the morphology of the

deposited YSZ as the weight percent of PVB (W_{PVB}) was varied. In the as-deposited state at $T = 25\text{ }^{\circ}\text{C}$, the YSZ–PVB composite maintained the spherical shape formed during the spray process, with larger spherical particles forming as the amount of PVB was gradually increased. The structural rearrangement of the continuous morphology was observed at $T = 100\text{ }^{\circ}\text{C}$, where the glass transition of PVB was seen: porous structures appeared at low PVB concentrations, while dense morphologies were observed at high PVB concentrations. These continuous structures were maintained during the burn-out ($400\text{ }^{\circ}\text{C}$) and sintering ($1350\text{ }^{\circ}\text{C}$) processes. When $W_{\text{YSZ}}/W_{\text{PVB}} = 3.5$, the YSZ particle film became a collection of porous structures after the high-temperature sintering step because there was insufficient PVB to form necks between the particles. When $W_{\text{YSZ}}/W_{\text{PVB}}$ was decreased, the particle film became denser and the pore structure was suppressed. When $W_{\text{YSZ}}/W_{\text{PVB}} = 1$, a densely annealed thin electrolyte layer was finally obtained. These results show that the particle rearrangement process near T_g of PVB determined the final sintering structure.

The optimum ratio of PVB additive could also be determined by analyzing of the particle dispersion in the YSZ slurry as a function of $W_{\text{YSZ}}/W_{\text{PVB}}$. **Figure 2.3** shows the close relationship between the particle size distribution of the YSZ slurry and its film quality. By keeping the solid loading and milling conditions constant, we were able to focus on the role of the PVB additive in the YSZ slurry. Significant tertiary YSZ aggregates were observed not only in pristine YSZ but also in $W_{\text{YSZ}}/W_{\text{PVB}} = 3.5$, i.e., when an insufficient amount of PVB was added, while the volume fraction

of primary particles was the highest when $W_{\text{YSZ}}/W_{\text{PVB}} = 1$. The narrow particle distribution and limited aggregates observed at the optimized PVB weight percent ($W_{\text{YSZ}}/W_{\text{PVB}} = 1$) resulted in a homogeneous dispersion and suitable packing of the YSZ particles, thus increasing the relative density of the sintered film. As a result, the cell with $W_{\text{YSZ}}/W_{\text{PVB}} = 3.5$ exhibited an OCV of ~ 0.96 V, while the cell with $W_{\text{YSZ}}/W_{\text{PVB}} = 1$ exhibited an OCV of ~ 1.11 V, which is close to the theoretical value of the material. Based on these results, we can conclude that the optimized PA-ESD process offers a straightforward method of fabricating very dense (i.e., gas-tight) thin YSZ films with thicknesses of $4 \mu\text{m}$.

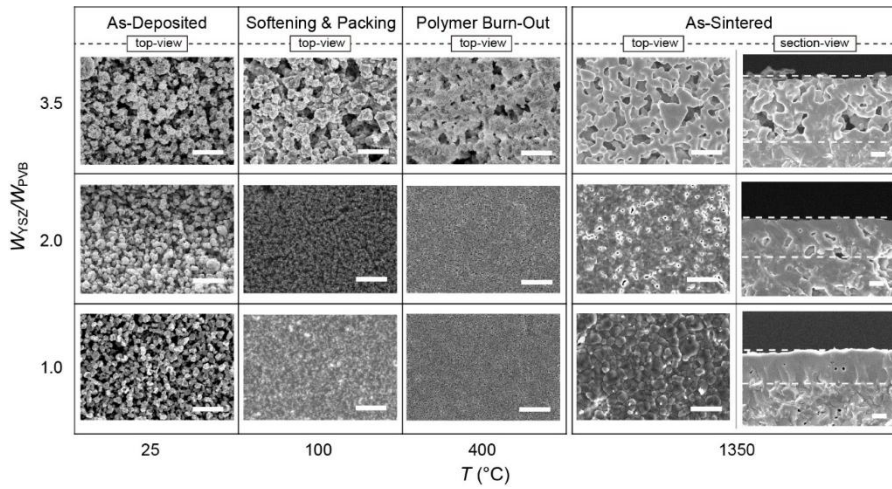


Figure 2.2. Variations in the microstructure of electrolytes during the sintering process (at 25, 100, 400, and 1350 °C) with different W_{YSZ}/W_{PVB} values. The top views of the YSZ electrolyte layer fabricated by the PA-ESD process are shown (scale bar: 2 μm). Cross-sectional SEM images at right end are represent YSZ structures after 1350 °C sintering (scale bar: 2 μm).

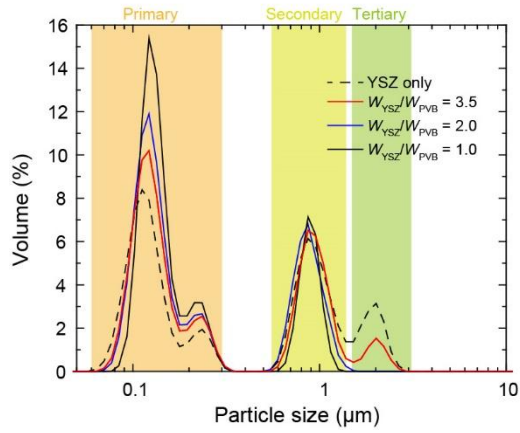


Figure 2.3. Particle size distribution of the YSZ and YSZ slurry at $W_{\text{YSZ}}/W_{\text{PVB}} = 1, 2, \text{ and } 3.5$. The first peak on the particle size curve correspond to the primary YSZ particles, and the others are the secondary and tertiary particles, major aggregates of primary particles. The result of pristine YSZ sample, indicated by a dashed black line, is also shown.

2.3.3. Microstructure control of ceramic layers for porous cathodes

As reported in the literature^{7,8}, one of the dominant losses in SOFCs is cathode polarization. Because the active area of the oxygen reduction reaction (ORR) in the SOFC cathode can be increased by applying a porous cathode layer, the cathode must have sufficient thickness and appropriate porosity to offer enough ORR sites. Therefore, when selecting the polymer binder for the cathode layer, its molecular weight (M_w) and the resulting slurry viscosity must be taken into consideration. As shown in **Figure 2.4**, we investigated variations in the porous ceramic layer as a function of the amount of polymer additive used. We chose PVP as the polymer binder in the LSC slurry for the fabrication of the SOFC cathode layer. Similar to PVB, PVP is widely used in ceramic powder-based slurry systems because of its adsorption ability^{38–40}. Compared with PVB ($M_w \approx 50,000\text{--}80,000$ g/mol), PVP has a much lower molecular weight ($M_w \approx 10,000$ g/mol), resulting in the LSC slurry having a lower viscosity and a higher solid loading.

In the cathode deposition process, the value of W_{PVP} affected the steric dispersion of LSC particles in the slurry, and different values of W_{PVP} resulted in deposited particles with different morphologies (**Figure 2.4**). When $W_{\text{LSC}}/W_{\text{PVP}} = 2$, the deposited LSC particles were large ball-shaped clusters due to the insufficient dispersion of the LSC because of the limited amount of PVP. However, when the amount of PVP was increased, more uniformly deposited LSC particles were observed. When $W_{\text{LSC}}/W_{\text{PVP}} = 1$, the deposited LSC-PVP composite rearranged and formed a film-like

structure at $T = 200\text{ }^{\circ}\text{C}$ (near T_g of PVP = $180\text{ }^{\circ}\text{C}$). When the temperature reached the burn-out point ($400\text{ }^{\circ}\text{C}$), a homogenous and crack-free porous structure was formed. Meanwhile, at $W_{\text{LSC}}/W_{\text{PVP}} = 0.5$, disordered and agglomerated structures were formed because of the high PVP content. Although a uniform film-like structure was formed at $T = 200\text{ }^{\circ}\text{C}$, a large crack formed in the burn-out step due to the excess of PVP, and an agglomerated structure formed after the sintering process ($950\text{ }^{\circ}\text{C}$). As mentioned earlier, analyzing the particle size distribution can help one to understand the principles of particle deposition via PA-ESD. Similar to the YSZ results, the first peak in the particle size curve corresponded to the primary LSC particles, while the other peaks correspond to the secondary and tertiary particles, i.e., major aggregates of the primary particles. As shown in **Figure 2.5**, the formation of significant secondary and tertiary LSC aggregates was suppressed when $W_{\text{LSC}}/W_{\text{PVP}} = 1$. Therefore, it can be confirmed that a homogeneous and crack-free porous structure was obtained because of the limited formation of aggregates and superior particle dispersion.

To check the effect of the cathode microstructure on the cathode polarization and thus the electrochemical cell performance, we tested three different cathode samples ($W_{\text{LSC}}/W_{\text{PVP}} = 0.5, 1, \text{ and } 2$). Note that a tape-laminated NiO–YSZ substrate with a screen-printed YSZ layer (thickness: $\sim 15\text{ }\mu\text{m}$) was used to minimize uncertainties due to other components in the experiment, while all layers related to cathode polarization resistance (e.g., CGO barrier, CFL and cathode) were still deposited by PA-ESD process. **Figure 2.6** shows the dependence of the electrochemical performance, I – V –

P characteristics, and EIS results on the $W_{\text{LSC}}/W_{\text{PVP}}$ ratio. Owing to the strong correlation between the number of ORR sites and the surface area of the SOFC cathode, the peak power density (or cell resistance) at $W_{\text{LSC}}/W_{\text{PVP}} = 2$ and 0.5 were not expected to be large (or small). Because the cell with $W_{\text{LSC}}/W_{\text{PVP}} = 2$ had higher porosity, its microstructure consisted of larger particles, which decreased the number of ORR sites and degraded the cathode performance [maximum power density (P_{max}) ≈ 305 mW/cm² and area-specific polarization resistance (ASR_{pol}) ≈ 3.22 $\Omega \cdot \text{cm}^2$ at 650 °C]. For the cell with $W_{\text{LSC}}/W_{\text{PVP}} = 0.5$, more voids were observed because of the disordered LSC structures, and the resulting decrease in the LSC surface area diminished the performance of the cell, such that $P_{\text{max}} \approx 300$ mW/cm² and $\text{ASR}_{\text{pol}} \approx 2.31$ at 650 °C. The maximum power densities of $W_{\text{LSC}}/W_{\text{PVP}} = 0.5$ and 2 were similar despite the different polarization resistances under OCV conditions. The $W_{\text{LSC}}/W_{\text{PVP}} = 2$ sample (consisting of large ball clusters) had a uniform microstructure, whereas the $W_{\text{LSC}}/W_{\text{PVP}} = 0.5$ sample (composed of small particles) had a non-uniform microstructure. Therefore, the activation resistance, which is related to the reaction area, was low in the $W_{\text{LSC}}/W_{\text{PVP}} = 0.5$ sample, while the ohmic component was low in the $W_{\text{LSC}}/W_{\text{PVP}} = 2$ sample, as in these systems the whole electrode network was uniform rather than disconnected. In contrast, because the cell with $W_{\text{LSC}}/W_{\text{PVP}} = 1$ had a uniformly deposited structure, it exhibited the best power performance and the lowest polarization resistance, i.e., $P_{\text{max}} \approx 400$ mW/cm² and $\text{ASR}_{\text{pol}} \approx 1.81$ at 650 °C. When LSC and PVP were mixed at the same weight ratio, the resulting cathode structure had a homogeneous particle distribution and moderate porosity, resulting in the

suppression of cathode polarization (i.e., better electrochemical performance).

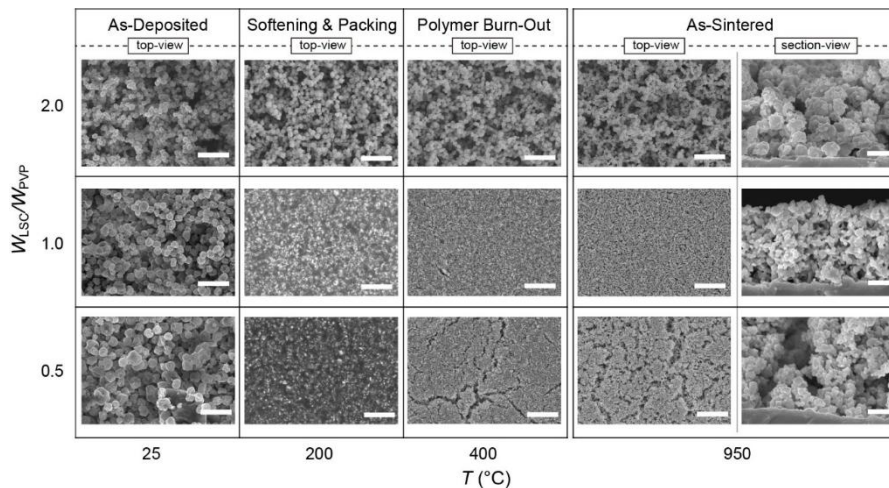


Figure 2.4. Variations in the microstructure of the LSC cathodes during the sintering process (at 25, 200, 400, and 950 °C) with different W_{LSC}/W_{PVP} values. The top views of the LSC cathode layer fabricated by the PA-ESD process are shown (scale bar: 2 μ m). Cross-sectional SEM images at right end are represent LSC structures after 950 °C sintering (scale bar: 1 μ m).

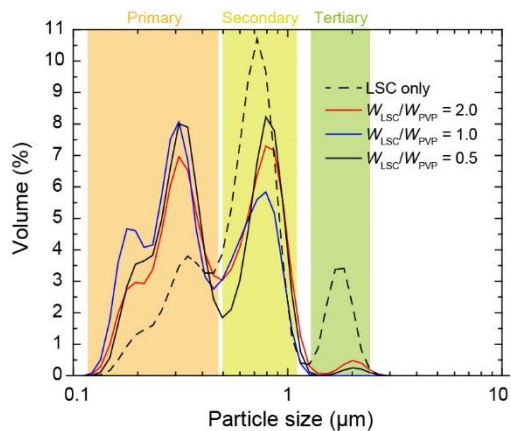


Figure 2.5. Particle size distribution of the LSC and LSC slurry at $W_{\text{LSC}}/W_{\text{PVP}} = 0.5, 1, \text{ and } 2$. The first peak on the particle size curve correspond to the primary LSC particles, and the others are the secondary and tertiary particles, major aggregates of primary particles. The result of pristine LSC sample, indicated by a dashed black line, is also shown.

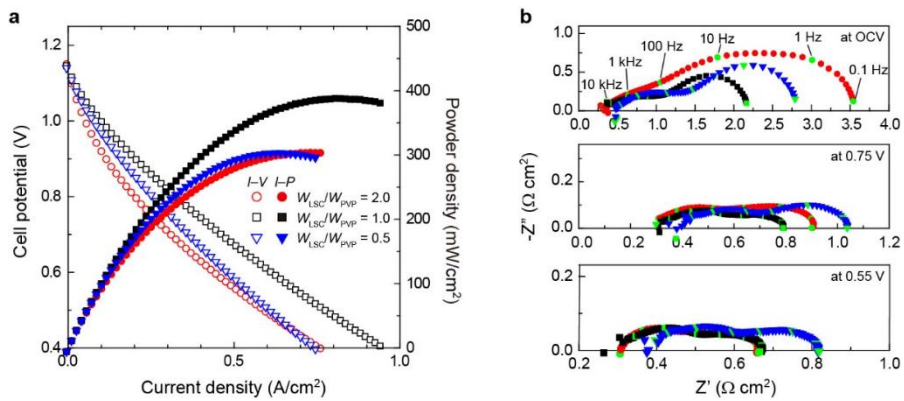


Figure 2.6. Electrochemical characterization of an anode-supported SOFC including the spray-deposited LSC cathode layer with different W_{LSC}/W_{PVP} values. (a) The $I-V-P$ curves and (b) EIS results measured at 650 °C in different cell voltages.

2.3.4. Electrochemical performance of spray-based SOFCs

We prepared a high-performance spray-deposition-based SOFC with a thin, dense electrolyte (thickness: $\sim 4 \mu\text{m}$) and a crack-free porous cathode/CFL (thickness: $\sim 10 \mu\text{m}$) using the optimized PA-ESD conditions, and the electrochemical performance of the cell was analyzed. **Figure 2.7** shows cross-sectional SEM images of an optimized cell, which consisted of multiple PA-ESD layers on a tape-laminated NiO–YSZ anode substrate. We observed that each layer had the appropriate microstructure, was well integrated, and showed strong interfacial bonding and structural uniformity. As shown in **Figure 2.8a**, such structural features resulted in a high OCV and high power-generating performance. The measured OCV of $\sim 1.11 \text{ V}$ approached the theoretical value, indicating that the thin PA-ESD-processed YSZ layer was sufficiently gas-impermeable even though it was generally thinner than a conventional powder-processed electrolyte including powder spray^{20,41–45} and screen printing^{46–48}. Compared with previously reported spray-deposition-based SOFCs (see **Table 2.2**), our spray-deposition-based SOFC delivered a substantially higher cell performance of $P_{\text{max}} = 805 \text{ mW/cm}^2$ at $650 \text{ }^\circ\text{C}$.

Figure 2.8b shows variations in the impedance spectra as a function of temperature for the final optimized cell under OCV conditions. Even though our spray-deposition-based process was used to simultaneously prepare the electrolyte and cathode layers, the PA-ESD cell showed all of the impedance characteristics (e.g., dependence on temperature and frequency) observed in a typical SOFC^{7,8,49}, indicating that it met the basic

electrochemical standards required for a power-generating device. Based on the ASR results in **Figure 2.8b**, we also performed electrochemical analysis of the newly introduced PA-ESD process as follows. (i) The area-specific ohmic resistance (ASR_{ohmic}) of the PA-ESD cell was dominated by the contribution of the YSZ electrolyte. The calculated ASR_{ohmic} with the reported YSZ conductivity ($\sim 2.4 \times 10^{-3}$ S/cm at 600 °C)⁵⁰ was $0.17 \Omega \cdot \text{cm}^2$, which is approximately equal to $0.20 \Omega \cdot \text{cm}^2$, the value measured in a PA-ESD cell. This result implies that the ohmic contributions of parameters other than the electrolyte (e.g., interface, connectivity, and porosity) were successfully suppressed. Therefore, it can be concluded that our PA-ESD process was well-optimized. (ii) The electrode polarization resistance of the PA-ESD cell was comparable to that of a conventional powder-processed cell. For example, ASR_{pol} of a LSC electrode at 600 °C is reported to be $\sim 1.2 \Omega \cdot \text{cm}^2$ ⁴⁹, which is about the same as that of the PA-ESD cell ($\sim 1.4 \Omega \cdot \text{cm}^2$) in our study. These results confirm that the cathode fabricated by the PA-ESD process had highly advanced membrane microstructures (i.e., many ORR sites, long triple-phase boundary, appropriate porosity, and well-percolated electronic and ionic structure) despite its low electrode thickness. We conclude that our spray-deposition-based dense electrolyte and porous cathode were well constructed, and they successfully played significant roles in the electrochemical reactions of the SOFC.

To check the durability of the PA-ESD cell, we tested the long-term operation under the constant current load of 0.4 A/cm^2 at 650 °C. Because the cell OCV and P_{max} are important indicators for the gas-tightness and cell degradation respectively, we recorded the OCV during the entire test

time and measured I - V curves every 100 h. **Figure 2.9** shows the results of long-term tests of our PA-ESD. Considering the P_{\max} results every 100 h, the degradation rate was $\sim 1.5\%$ over 100 h at a current density of 0.4 A/cm^2 . Such deterioration in cell performance can be attributed to (i) decrease in reaction sites, (ii) loss of nickel percolated structure, (iii) secondary phase formation at the electrode-electrolyte interface, and (iv) increase in contact resistance between cathode and interconnector, as reported in literatures^{47,48,51}. Nevertheless, it is important to note that we have completed a long-term performance test over 100 h, which are difficult to find in spray-based SOFCs, with the degradation rate of $\sim 1.5\%$, and each component built with PA-ESD process works well under the electrochemical operation over 100 h.

T (°C)	P_{\max} (mW/cm ²)	OCV (V)	Anode	Electrolyte	Cathode	Reference
650	805	1.11	Ni-YSZ	YSZ, 4 μm (Electrospray)	LSC (Electrospray)	This work
600	85	1.1	Ni-YSZ	LSGM, 50 μm (Plasma spray)	LSCF (Plasma spray)	20
800	550	1.06	Ni-YSZ	YSZ, 3 μm (Electrospray)	LSM (Brush)	26
700	234	1.02	Ni-YSZ	YSZ, 15 μm (Air spray)	LSM (Brush)	41
600	30	0.81	Ni-CGO	CGO, 8 μm (Air spray)	LSCF (Screen printing)	42
750	610	0.9	Ni-YSZ	YSZ, 20 μm (Plasma spray)	BPCF (Screen printing)	43
650	735	0.81	Ni-CGO	CGO, 10 μm (Electrospray)	LSCF (Electrospray)	44
640	41.3	1.11	Ni-YSZ	YSZ, 0.1 μm (Sputter)	LSM (Electrospray)	52
640	673	1.1	Ni-YSZ	YSZ, 0.4 μm (Sputter)	LSM (Electrospray)	53
750	599	1.0	Ni-YSZ	YSZ, 30 μm (Plasma spray)	LSCF-CSO (Plasma spray)	45
650	760	1.11	Ni-YSZ	YSZ, 6 μm (Screen printing)	SSC-CSO (Spray pyrolysis)	46
650	510	0.71	Ni-YSZ	CGO, 3 μm (Spray pyrolysis)	SSC-CSO (Screen printing)	54

Material abbreviations: [20] $\text{La}_{0.8}\text{Sr}_{0.2}\text{Ga}_{0.8}\text{Mg}_{0.2}\text{O}_3$ (LSGM), $\text{La}_{0.6}\text{Sr}_{0.4}\text{Co}_{0.2}\text{Fe}_{0.8}\text{O}_3$ (LSCF), [26,41] $\text{La}_{0.85}\text{Sr}_{0.15}\text{MnO}_3$ (LSM), [42] $\text{La}_{0.8}\text{Sr}_{0.2}\text{Co}_{0.8}\text{Fe}_{0.2}\text{O}_3$ (LSCF), [43] $\text{Ba}_{0.5}\text{Pr}_{0.5}\text{Co}_{0.8}\text{Fe}_{0.2}\text{O}_{3-\delta}$ (BPCF), [44] $\text{La}_{0.6}\text{Sr}_{0.4}\text{Co}_{0.2}\text{Fe}_{0.8}\text{O}_{3-\delta}$ (LSCF), [52,53] $\text{La}_{0.8}\text{Sr}_{0.2}\text{MnO}_3$ (LSM), [45] $\text{La}_{0.6}\text{Sr}_{0.4}\text{Co}_{0.2}\text{Fe}_{0.8}\text{O}_{3-\delta}\text{-Ce}_{0.8}\text{Sm}_{0.2}\text{O}_{2-\delta}$ (LSCF-CSO), [46,54] $\text{Sm}_{0.5}\text{Sr}_{0.5}\text{CoO}_3\text{-Sm}_{0.2}\text{Ce}_{0.8}\text{O}_{1.9}$ (SSC-CSO).

Table 2.2. Performance comparison of anode-supported SOFCs fabricated by spray-based process.

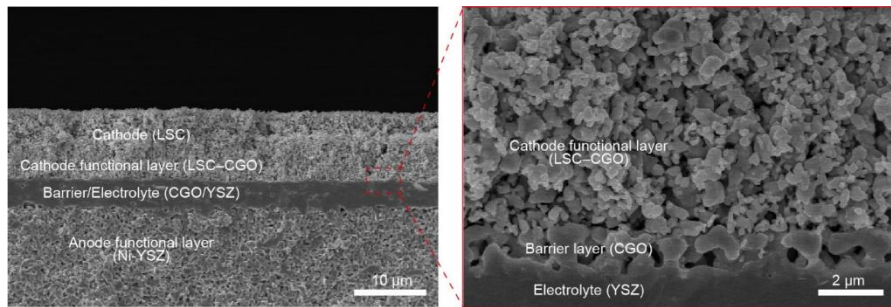


Figure 2.7. A cross-sectional SEM image of the SOFC fabricated by the optimized PA-ESD process. A whole structure composed of anode, anode functional, electrolyte, barrier, cathode functional, and cathode layers are presented. Note that these are microstructure images observed by fracturing the PA-ESD cell after the cell test.

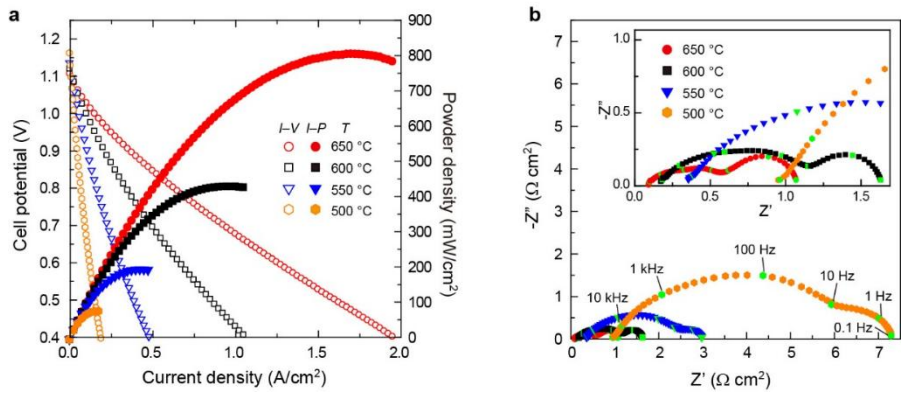


Figure 2.8. Electrochemical characterization of an anode-supported SOFC fabricated by the optimized PA-ESD process. (a) The $I-V-P$ curves and (b) EIS results at different operation temperature. For the EIS curves, the inset shows the magnified view of high-temperature results.

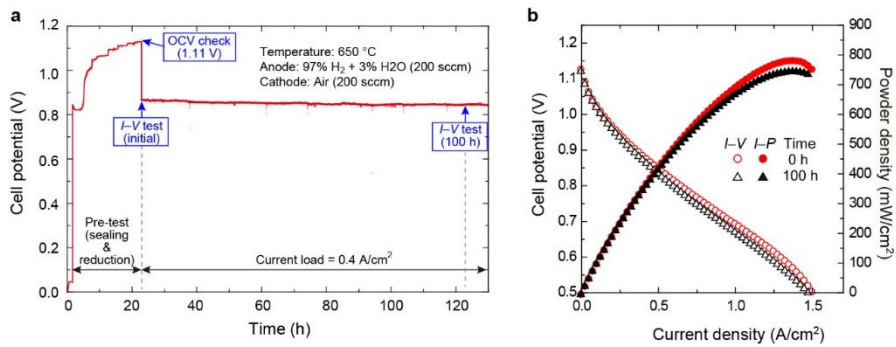


Figure 2.9. Long-term test results of an anode-supported SOFC fabricated by the optimized PA-ESD process. (a) Cell voltage measurement under 0.4 A/cm² current at 650 °C and (b) $I-V-P$ curves at 0 and 100 h.

2.4. Conclusions

In summary, we developed an advanced deposition process for fabricating a dense thin electrolyte and a crack-free porous cathode as membrane components of a SOFC. We confirmed that the microstructural morphologies of these membrane layers could be controlled by altering the amounts of the polymer additives used, which affected the dispersion state of the PA-ESD solution. We showed that the high-performance SOFC consisted of a dense, thin electrolyte layer (thickness: 4 μm) and a crack-free porous cathode layer (thickness: 10 μm), both of which were deposited via the PA-ESD process. The cell exhibited an excellent OCV of ~ 1.11 V and a P_{max} of ~ 805 mW/cm^2 at 650 $^{\circ}\text{C}$, which represents substantially higher power-generating performance than seen for previously reported SOFCs manufactured by spray-deposition-based processes. Also, we verified the long-term durability of our PA-ESD cell under the constant current load at 650 $^{\circ}\text{C}$. These results demonstrate the successful construction of a dense, thin electrolyte layer and a crack-free porous cathode layer via a spray-deposition-based process. Considering the advantages of fast, large-area fabrication and high performance, our PA-ESD process is a promising technique for the large-scale and economic development of superior SOFC membranes.

2.5. References

1. Minh, N. Q. Ceramic fuel-cells, *Journal of American Ceramic Society* **76**, 563-588 (1993).
2. Park, S.D.; Vohs, R. J.; Gorte, R. J. Direct Oxidation of hydrocarbons in a solid-oxide fuel cell. *Nature* **404**, 265-267 (2000).
3. Ormerod, R. M. Solid oxide fuel cells. *Chemical Society Reviews* **32**, 17-28 (2003).
4. Chen, Y.; Zhang, Y.; Lin, Y.; Yang, Z.; Su, D.; Han, M.; Chen, F. Direct-methane solid oxide fuel cells with hierarchically porous Ni-based anode deposited with nanocatalyst layer. *Nano Energy* **10**, 1–9 (2014).
5. Zhang, X.; Chan, S. H.; Li, G.; Ho, H. K.; Li, J.; Feng, Z. A review of integration strategies for solid oxide fuel cells. *Journal of Power Sources* **195**, 685–702 (2010).
6. Badwal, S. P. S.; Giddey, S.; Munnings, C.; Kulkarni, A. Review of progress in high temperature solid oxide fuel cells. *Journal of the Australian Ceramic Society* **50**, 23–37 (2014).
7. Park, S. Y.; Ji, H. II; Kim, H. R.; Yoon, K. J.; Son, J. W.; Kim, B. K.; Je, H. J.; Lee, H. W.; Lee, J. H. Structural optimization of (La, Sr)CoO₃-based multilayered composite cathode for solid-oxide fuel cells. *Journal of Power Sources* **228**, 97–103 (2013).
8. Smith, J. R.; Chen, A.; Gostovic, D.; Hickey, D.; Kunding, D.; Duncan, K. L.; DeHoff, R. T.; Jones, K. S.; Wachsman, E. D. Evaluation of the relationship between cathode microstructure and electrochemical behavior for SOFCs. *Solid State Ionics* **180**, 90–98 (2009).
9. Malzbender, J.; Fischer, W.; Steinbrech, R. W. Studies of residual stresses in planar solid oxide fuel cells. *Journal of Power Sources* **182**, 594–598 (2008).
10. Tietz, F.; Buchkremer, H. P.; Stöver, D. Components manufacturing for solid oxide fuel cells. *Solid State Ionics* **152–153**, 373–381 (2002).
11. Li, Z. P.; Toshiyuki, M.; Auchterlonie, G. J.; Zou, J.; John, D. Mutual

- diffusion occurring at the interface between $\text{La}_{0.6}\text{Sr}_{0.4}\text{Co}_{0.8}\text{Fe}_{0.2}\text{O}_3$ cathode and Gd-doped ceria electrolyte during IT-SOFC cell preparation. *ACS Applied Materials and Interfaces* **3**, 2772–2778 (2011).
12. Fowler, D. E.; Haag, J. M.; Boland, C.; Bierschenk, D. M.; Barnett, S. A.; Poepfelmeier, K. R. Stable, Low Polarization Resistance Solid Oxide Fuel Cell Anodes: $\text{La}_{1-x}\text{Sr}_x\text{Cr}_{1-x}\text{Fe}_x\text{O}_{3-\delta}$ ($x = 0.2\text{--}0.67$). *Chemistry of Materials* **26**, 3113–3120 (2014).
 13. Liu, Q. L.; Khor, K. A.; Chan, S. H.; Chen, X. J. Anode-supported solid oxide fuel cell with yttria-stabilized zirconia/gadolinia-doped ceria bilayer electrolyte prepared by wet ceramic co-sintering process. *Journal of Power Sources* **162**, 1036–1042 (2006).
 14. Piao, J.; Sun, K.; Zhang, N.; Xu, S. A study of process parameters of LSM and LSM-YSZ composite cathode films prepared by screen-printing. *Journal of Power Sources* **175**, 288–295 (2008).
 15. Noh, H. S.; Yoon, K. J.; Kim, B. K.; Je, H. J.; Lee, H. W.; Lee, J. H.; Son, J. W. The potential and challenges of thin-film electrolyte and nanostructured electrode for yttria-stabilized zirconia-base anode-supported solid oxide fuel cells. *Journal of Power Sources* **247**, 105–111 (2014).
 16. Jung, W.; Dereux, J. O.; Chueh, W. C.; Hao, Y.; Haile, S. M. High electrode activity of nanostructured, columnar ceria films for solid oxide fuel cells. *Energy and Environmental Science* **5**, 8682–8689 (2012).
 17. Oh, E. O.; Whang, C. M.; Lee, Y. R.; Park, S. Y.; Prasad, D. H.; Yoon, K. J.; Son, J. W.; Lee, J. H.; Lee, H. W. Extremely thin bilayer electrolyte for solid oxide fuel cells (SOFCs) fabricated by chemical solution deposition (CSD). *Advanced Materials* **24**, 3373–3377 (2012).
 18. Fan, L.; Wang, C.; Zhu, B. Low temperature ceramic fuel cells using all nano composite materials. *Nano Energy* **1**, 631–639 (2012).
 19. Killinger, A.; Gadow, R.; Mauer, G.; Guignard, A.; Vaen, R.; Stöver, D. Review of new developments in suspension and solution precursor thermal spray processes. *Journal of Thermal Spray Technology* **20**, 677–695 (2011).

20. Zhang, S. L.; Liu, T.; Li, C. J.; Yao, S. W.; Li, C. X.; Yang, G. J.; Liu, M. Atmospheric plasma-sprayed $\text{La}_{0.8}\text{Sr}_{0.2}\text{Ga}_{0.8}\text{Mg}_{0.2}\text{O}_3$ electrolyte membranes for intermediate-temperature solid oxide fuel cells. *Journal of Materials Chemistry A* **3**, 7535–7553 (2015).
21. Chen, C.; Kelder, E. M.; Schoonman, J. Functional Ceramic Films with Reticular Structures. *J. Electrochem. Soc.* **144**, 8–10 (1997).
22. Liu, L.; Kim, G. Y.; Hillier, A. C.; Chandra, A. Microstructural and electrochemical impedance study of nickel- $\text{Ce}_{0.9}\text{Gd}_{0.1}\text{O}_{1.95}$ anodes for solid oxide fuel cells fabricated by ultrasonic spray pyrolysis. *Journal of Power Sources* **196**, 3026–3032 (2011).
23. Jaworek, A.; Sobczyk, A. T. Electro spraying route to nanotechnology: An overview. *Journal of Electrostatics* **66**, 197–219 (2008).
24. Marinha, D.; Rossignol, C.; Djurado, E. Influence of electro spraying parameters on the microstructure of $\text{La}_{0.6}\text{Sr}_{0.4}\text{Co}_{0.2}\text{Fe}_{0.8}\text{O}_{3-\delta}$ films for SOFCs. *Journal of Solid State Chemistry* **182**, 1742–1748 (2009).
25. Sharma, R. K.; Burriel, M.; Djurado, E. $\text{La}_4\text{Ni}_3\text{O}_{10-\delta}$ as an efficient solid oxide fuel cell cathode: Electrochemical properties versus microstructure. *Journal of Materials Chemistry A* **3**, 23833–23843 (2015).
26. Nomura, H.; Parekh, S.; Selman, J. R.; Al-Hallaj, S. Fabrication of YSZ electrolyte for intermediate temperature solid oxide fuel cell using electrostatic spray deposition: II - Cell performance. *Journal of Applied Electrochemistry* **35**, 1121–1126 (2005).
27. Rossignol, C.; Roman, B.; Benetti, G. D.; Djurado, E. Elaboration of thin and dense CGO films adherent to YSZ by electrostatic spray deposition for IT-SOFC applications. *New Journal of Chemistry* **35**, 716–723 (2011).
28. Rietveld, I. B.; Kobayashi, K.; Yamada, H.; Matsushige, K. Electro spray deposition, model, and experiment: Toward general control of film morphology. *Journal of Physical Chemistry B* **110**, 23351–23364 (2006).
29. Cho, Y.; Vu, B. Q.; Bedair, T. M.; Park, B. J.; Joung, Y. K.; Han, D. K. Crack prevention of biodegradable polymer coating on metal facilitated by a nano-coupled interlayer. *Journal of Bioactive and Compatible Polymers*

- 29**, 515–526 (2014).
30. Shri Prakash, B.; Senthil Kumar, S.; Aruna, S. T. Properties and development of Ni/YSZ as an anode material in solid oxide fuel cell: A review. *Renewable and Sustainable Energy Reviews* **36**, 149–179 (2014).
 31. Tseng, W. J.; Lin, C. L. Effect of polyvinyl butyral on the rheological properties of BaTiO₃ powder in ethanol-isopropanol mixtures. *Materials Letters* **57**, 223–228 (2002).
 32. Zhang, J.; Jiang, D.; Lin, Q. Poly(vinyl pyrrolidone), a dispersant for non-aqueous processing of silicon carbide. *Journal of the American Ceramic Society* **88**, 1054–1056 (2005).
 33. Dos Santos-Gómez, L.; Losilla, E. R.; Martín, F.; Ramos-Barrado, J. R.; Marrero-López, D. Novel microstructural strategies to enhance the electrochemical performance of La_{0.8}Sr_{0.2}MnO_{3-δ} cathodes. *ACS Applied Materials and Interfaces* **7**, 7197–7205 (2015).
 34. Park, J. H.; Han, S. M.; Yoon, K. J.; Kim, H.; Hong, J.; Kim, B. K.; Lee, J. H.; Son, J. W. Impact of nanostructured anode on low-temperature performance of thin-film-based anode-supported solid oxide fuel cells. *Journal of Power Sources* **315**, 324–330 (2016).
 35. Noh, H. S.; Lee, H.; Kim, B. K.; Lee, H. W.; Lee, J. H.; Son, J. W. Microstructural factors of electrodes affecting the performance of anode-supported thin film yttria-stabilized zirconia electrolyte (~ 1 μm) solid oxide fuel cells. *Journal of Power Sources* **196**, 7169–7174 (2011).
 36. Cho, C. W.; Cho, Y. S.; Yeo, J. G.; Kim, J.; Paik, U. Effects of PVB on the gelation behavior of BaTiO₃ -based dielectric particles and glass suspension. *Journal of the European Ceramic Society* **23**, 2315–2322 (2003).
 37. Bhattacharjee, S.; Paria, M. K.; Maiti, H. S. Polyvinyl butyral as a dispersant for barium titanate in a non-aqueous suspension. *Journal of Materials Science* **28**, 6490–6495 (1993).
 38. Park, I.; Ahn, J.; Im, J.; Choi, J.; Shin, D. Influence of rheological characteristics of YSZ suspension on the morphology of YSZ films

- deposited by electrostatic spray deposition. *Ceramics International* **38**, S481–S484 (2012).
39. Dhaliwal, A. K.; Hay, J. N. The characterization of polyvinyl butyral by thermal analysis. *Thermochimica Acta* **391**, 245–255 (2002).
 40. Howe, K. S.; Clark, E. R.; Bowen, J.; Kendall, K. A novel water-based cathode ink formulation. *International Journal of Hydrogen Energy* **38**, 1731–1736 (2013).
 41. Ding, J.; Liu, J. An anode-supported solid oxide fuel cell with spray-coated yttria-stabilized zirconia (YSZ) electrolyte film. *Solid State Ionics* **179**, 1246–1249 (2008).
 42. Ding, C.; Lin, H.; Sato, K.; Tsutai, Y.; Iguchi, M.; Hashida, T. Preparation and characterization of $\text{Ce}_{0.9}\text{Gd}_{0.1}\text{O}_{1.95}$ electrolyte films by spray coating process. *Journal of Solid Mechanics and Materials Engineering* **4**, 325–334 (2010).
 43. Wang, Y.; Legoux, J. G.; Neagu, R.; Hui, S.; Marple, B. R. Suspension plasma spray and performance characterization of half cells with NiO-YSZ anode and YSZ electrolyte. *Journal of Thermal Spray Technology* **21**, 7–15 (2012).
 44. Lee, J.; Park, I.; Lee, H.; Shin, D. Effects of embossing structure on the performance of intermediate- temperature solid oxide fuel cells with gadolinium-doped ceria electrolyte. *Journal of Power Sources* **212**, 35–42 (2012).
 45. Marr, M.; Kuhn, J.; Metcalfe, C.; Harris, J.; Kesler, O. Electrochemical performance of solid oxide fuel cells having electrolytes made by suspension and solution precursor plasma spraying. *Journal of Power Sources* **245**, 398–405 (2014).
 46. Shimada, H.; Yamaguchi, T.; Suzuki, T.; Sumi, H.; Hamamoto, K.; Fujishiro, Y. High power density cell using nanostructured Sr-doped SmCoO_3 and Sm-doped CeO_2 composite powder synthesized by spray pyrolysis. *Journal of Power Sources* **302**, 308–314 (2016).
 47. Jørgensen, M. J.; Holtappels, P.; Appel, C. C. Durability test of SOFC

- cathodes. *Journal of Applied Electrochemistry* **30**, 411–418 (2000).
48. Jung, H. Y.; Choi, S. H.; Kim, H.; Son, J. W.; Kim, J.; Lee, H. W.; Lee, J. H. Fabrication and performance evaluation of 3-cell SOFC stack based on planar 10 cm × 10 cm anode-supported cells. *Journal of Power Sources* **159**, 478–483 (2006).
49. Marani, D.; Sudireddy, B. R.; Bentzen, J. J.; Jørgensen, P. S.; Kiebach, R. Colloidal stabilization of cerium-gadolinium oxide (CGO) suspensions via rheology. *Journal of the European Ceramic Society* **35**, 2823–2832 (2015).
50. Ried, P.; Lorenz, C.; Brönstrup, A.; Graule, T.; Menzler, N. H.; Sitte, W.; Holtappels, P. Processing of YSZ screen printing pastes and the characterization of the electrolyte layers for anode supported SOFC. *Journal of the European Ceramic Society* **28**, 1801–1808 (2008).
51. Monceau, D.; Filal, M.; Tebtoub, M.; Petot, C.; Petot-Ervas, G. Kinetic demixing of ceramics in an electrical field. *Solid State Ionics* **73**, 221–225 (1994).
52. Choi, S. H.; Kim, S. W.; Hwang, C. S.; Lee, M. H. Freestanding micro-SOFCs with electrodes prepared by electrostatic spray deposition. *Fuel Cells* **14**, 332–335 (2014).
53. Choi, S. H.; Hwang, C. S.; Lee, M. H. Performance Enhancement of Freestanding Micro-SOFCs with Ceramic Electrodes by the Insertion of a YSZ-Ag Interlayer. *ECS Electrochemistry Letters* **3**, F57–F59 (2014).
54. Reolon, R. P.; Halmenschlager, C. M.; Neagu, R.; De Fraga Malfatti, C.; Bergmann, C. P. Electrochemical performance of gadolinia-doped ceria (CGO) electrolyte thin films for ITSOFC deposited by spray pyrolysis. *Journal of Power Sources* **261**, 348–355 (2014).

Chapter 3.

Multiscale Electrode Architecturing

Technologies via Precursor-Solution

Electrospray Deposition

3.1. Introduction

Low-temperature solid oxide fuel cells (SOFCs) with nanostructured ceramic multilayer architecture provide many advantages, such as higher cell efficiency and system reliability, and reduced maintenance costs ¹⁻⁵. The Ohmic and polarization resistance losses in SOFCs can be reduced by nanostructuring the multilayer ceramic structure of the fuel cells ⁶ and by increasing the number of electrochemical reaction sites (i.e., triple-phase boundaries) ^{7,8}. In recent years, many studies have used nanoscale thin-film electrolytes and increased the number of active sites for the oxygen reduction reaction (ORR) to reduce Ohmic and polarization resistances, respectively ^{9,10}.

Nanoscale thin films and particles have been fabricated by various vacuum-deposition and solution-based processes ¹¹⁻¹³. However, nanoscale thin-film SOFCs suffer from drawbacks, such as severe agglomeration and structural instability owing to the large specific surface area of the

nanostructured materials ¹⁴⁻¹⁶. It is difficult to disperse agglomerated nanoparticles to fabricate a thin film or a homogeneous catalyst structure. In addition, the fabricated thin-film nanostructures often show defects or fail during operation, thereby deteriorating the performance of the entire cell ⁶. Furthermore, advanced thin-film deposition methods, such as atomic-layer deposition and pulsed-laser deposition (PLD) have limited applicability owing to their high cost, use of expensive vacuum devices, limited range of available materials, and small deposition area ^{6,14,17}.

Electrospray deposition (ESD) methods can overcome the limitations of vacuum-based thin-film technologies and allow the development of economically viable nanostructured SOFCs ^{18,19}. In the electrospray method, a voltage is applied to a precursor solution with various morphologies, which dissociates the droplets and deposits a thin film via an electrostatic repulsion force. This method has been used to produce fuel cells ¹⁹⁻²², batteries ^{23,24}, sensors ^{25,26}, filters ^{27,28}, and catalysts ^{29,30} as it is suitable for use with a wide variety of solutions and substrates. Many previous electrospraying studies have been used to fabricate various structures of SOFCs ^{18,19,31-40}. Most of the results have been used to form microscale porous electrodes ^{19,31-33} or dense electrolyte ^{19,34} structures using powder-based suspensions, and some of which have been applied as micro-/submicro-scale structures (e.g., electrodes ³⁵⁻³⁸, electrolytes ^{39,40}, interfacial layers ^{18,38}, etc.) using precursor-based solutions. However, due to inherent limitations of the precursor-based solution electrospraying (e.g., high polymer contents, low solid loadings, and high-temperature crystallization) ⁴¹, the interface structure is unstable and there is a limit to the application of

composite materials. Therefore, it is difficult to achieve stable electro spraying conditions with precursor-solution electro spraying.

To solve this problem, this study develops a methodology for fabricating a multiscale cathode structure in low-temperature SOFCs by using a precursor-solution electro spray technique. The developed method does not require vacuum and was able to fabricate advanced cathode structures with thin-film cathode interlayers and homogeneously formed nano-catalysts from uniform infiltration, which could not be fabricated using conventional electro spray methods. The crystal structure, morphology, and electrochemical properties of multiscale cathode were investigated. SOFCs with multiscale cathode were fabricated, and their electrochemical power density was measured to demonstrate the feasibility of using such cathode interlayers and uniformly infiltrated nano-catalysts in high-performance low-temperature SOFCs.

3.2. Experimental

Electrospraying for ceramic thin film fabrication technology

$\text{La}_{0.6}\text{Sr}_{0.4}\text{CoO}_{3-\delta}$ and CeO_2 precursor solutions were prepared using exact stoichiometric amounts of the metal nitrates $\text{La}(\text{NO}_3)_3 \cdot 6\text{H}_2\text{O}$, $\text{Sr}(\text{NO}_3)_2$, $\text{Co}(\text{NO}_3)_2 \cdot 6\text{H}_2\text{O}$, and $\text{Ce}(\text{NO}_3)_3 \cdot 6\text{H}_2\text{O}$ in deionized water as a base solvent. Ethylene glycol and citric acid were added to this solution as a reducing agent and surfactant, respectively. The total concentration of metal nitrates was 0.6 mol L^{-1} , and the citric acid:ethylene glycol:metal ion concentration ratio was 9:3:1. After mixing the solution, 0.6 mol L^{-1} of ammonium hydroxide was added to control the pH. All metal nitrates and additives were purchased from Sigma-Aldrich. The powder-suspension electrospray method was used to fabricate a microscale cathode functional layer (mCFL) and cathode current-collecting layer (CCCL), as described previously¹⁹. The mCFL slurry consisted of LSC (Kceracell; $d_{50} = 400 \text{ nm}$) and $\text{Ce}_{0.9}\text{Gd}_{0.1}\text{O}_{1.95}$ (CGO; Rhodia; $d_{50} = 200 \text{ nm}$), while the CCCL slurry contained only LSC powder. The solid loadings of the mCFL and CCCL slurries were 5 and 10 wt %, respectively. Polyvinylpyrrolidone was used as a binder in a 1:1 ratio with the powder. All powder-suspension slurries were mixed with ethanol and ball-milled for 24 h. The electrospray system consisted of a high-voltage power supply (NanoNC), a pump controller (KD Scientific), and a micronozzle (NanoNC). For precursor-solution electrospraying, the nozzle-to-substrate distance (H) was set to 4 cm, and the slurry flow rate (q) was fixed at $25 \mu\text{L h}^{-1}$. In contrast, for powder-

suspension electrospaying, the nozzle-to-substrate distance was set to 6 cm, and the slurry flow rate was fixed at 0.3 mL h⁻¹. **Table 3.1** details the process conditions of each electrospay technique.

Cell fabrication to verify the effect of ceramic thin film fabrication technology

As shown in the flowchart in **Figure 3.1**, SOFCs with three different structures were fabricated to investigate the effect of the nanoscale interlayer on the composite cathode. The anode-supported substrate was purchased from RIST and cut into 2 cm × 2 cm pieces for preparing the full cell⁴². This anode-supported substrate consisted of a 5- μ m-thick Y₂O₃-stabilized ZrO₂ (YSZ) electrolyte film, a Ni-YSZ cathode functional layer, and a Ni-YSZ anode support. Details regarding the cell fabrication can be found in a previous study¹⁹. A 250-nm-thick CGO film was deposited on the YSZ electrolyte layer (EL) by PLD as a buffer layer (BL); the cell components were identical for all samples, except for the cathode interlayers.

Three different cells were prepared using precursor-solution electrospaying with two different nanoscale interlayers in the composite cathode: (i) an LSC interlayer, hereafter referred to as the nanoscale-adhesion layer (nAL); and (ii) an LSC–CeO₂ composite interlayer, hereafter referred to as the nanoscale-cathode-functional layer (nCFL). Each precursor solution was deposited by electrospaying on the CGO/YSZ/Ni-YSZ substrate (active area = 1 cm × 1 cm) under the same conditions and

then sintered at 950°C for 1 h. A reference cell without nanoscale interlayers (denoted as Ref-cell) was also prepared as a control. The cells with LSC and LSC-CeO₂ interlayers are denoted as nAL-cell and nCFL-cell, respectively. For all three cells, mCFL and CCCL were deposited using a powder-suspension electrospray with thicknesses of 2 and 4 μm, respectively. **Table 3.1** shows details of the electrospray conditions used to prepare the multilayer cathode.

Electrospraying for infiltration technology

We prepared the Sm_{0.5}Sr_{0.5}CoO_{3-δ} (SSC) precursor-solution for the infiltration process using exact stoichiometric amounts. Sm(NO₃)₃·6H₂O, Sr(NO₃)₂, Co(NO₃)₂·6H₂O were used in a concentration ratio of 1:1:2 and deionized water (DI water) was used as a base solvent. 0.5 mol L⁻¹ precursor-solution was prepared by using urea as surfactant. All metal nitrates and additive were purchased from Sigma-Aldrich. Spherical-shape Al₂O₃ (alumina, d₅₀ = 800 nm, US Research) powder was used as the material of the scaffold structure to analyze the structural difference of the conventional infiltration method and the ESD infiltration method. Alumina powder and polymer dispersant were mixed in a weight ratio of 1:1 to fabricate the scaffold structure, then printed on dense YSZ substrate by blading method and sintered at 1100 °C for 2 h. A powder-suspension ESD method, described in chapter 2, was used to fabricate the backbone cathode. To prepare the cathode slurry, (La_{0.6}Sr_{0.4})_{0.95}Co_{0.2}Fe_{0.8}O_{3-δ} (LSCF, d₅₀ = 400-800 nm, Fuel cell materials) powder and polyvinylpyrrolidone as a binder

were used. The solid loading of LSCF was 10 wt%, and the binder was used in a 1:1 weight ratio with the powder. The base solvent of the cathode slurry was ethyl alcohol. After the mixing of the cathode slurry, ball-milling was carried out for 24 h. A syringe pump controller (KD Scientific), a micro-syringe needle (NanoNC) and a high-voltage power supply (NanoNC) were used for the powder-suspension ESD method and the precursor-solution ESD method. For the processing condition of precursor-solution ESD method, applied voltage of 13 kV, nozzle-tip diameter of 8 μm , flow rate of 30 $\mu\text{l h}^{-1}$, 4 cm distance between nozzle and substrate and room temperature substrate temperature were used. While, for the processing condition of powder-suspension ESD method, applied voltage of 6 kV, nozzle-tip diameter of 250 μm , flow rate of 0.2 ml h^{-1} , 4 cm distance between nozzle and substrate and substrate temperature of 120 $^{\circ}\text{C}$ were used.

Cell fabrication to verify the effect of infiltration technology

To compare the electrochemical performance of a multiscale cathode fabricated via a novel infiltration method using humidification and a conventional infiltration method, we fabricated SOFCs with four different cathode structures. Anode-supported substrate was prepared from RIST and cut into 2 cm \times 2 cm to prepare full cell⁴². The substrate consists of a Ni-YSZ anode support, a Ni-YSZ anode functional layer and a 5- μm -thick YSZ electrolyte layer. A 250-nm-thick CGO buffer electrolyte layer was

deposited on the substrate using an RF sputtering process. The sputtering process was performed under the condition of RF power of 100 W, substrate temperature of 700 °C and the pressure of 5 mTorr using ambient Ar gas. LSCF was used as a backbone cathode material in all four cells, and was deposited using a powder-suspension ESD method. After sintered at 1050 °C for 1 h, it was fabricated to a thickness of 4 μm (active area = 1 cm × 1 cm). Ref-cell was fabricated without infiltration process, and CI-cell, EI-cell and HEI-cell were fabricated with 5 μl of SSC precursor-solution infiltration process. Infiltration for CI-cell fabrication was performed by precursor-solution dropping method using micro-pipette (Discovery comfort, HTL). Infiltration process of EI-cell and HEI-cell was conducted using precursor-solution ESD method, and the deposition time was 1 h. All four cells were fabricated under the condition of 20 % RH at 25 °C and HEI-cell was additionally humidified for 1 h under the condition of 70 % RH at 25 °C. Especially in HEI-cell fabrication, digital incubator (Rcom) was used for precise humidity control. Three different cells, except Ref-cell, were heat-treated at 1000 °C for 1 h after infiltration.

Cell characterization

Electrochemical testing of the prepared cells was performed with humidified 3% H₂ as the fuel, and air was supplied as the oxidant at a rate of 200 mL min⁻¹. The cells were evaluated considering the current density-potential-power density (*I-V-P*) characteristics from 500 °C to 650 °C at

50 °C intervals. Impedance spectra were obtained using electrochemical impedance spectroscopy (IviumStat, Ivium Technologies) over the frequency range of 0.1 to 1×10^6 Hz. The crystalline structures of the cathode interlayer materials were analyzed using X-ray diffractometry (XRD; D8 Advance, Bruker) with Cu $K\alpha$ radiation. The microstructures and thicknesses of the thin-films were investigated using scanning electron microscopy (SEM; Merlin, Zeiss).

Layer	r (μm)	V_n (kV)	H (cm)	q (mL h^{-1})	t_{dep} (h)	T_s ($^{\circ}\text{C}$)
nAL	8	13	4	0.025	1	950
nCFL	8	13	4	0.025	1	950
mCFL	250	8	6	0.3	0.5	950
CCCL	250	8	6	0.3	1	950

Table 3.1. Processing variables used to deposit the various layers using electrospaying. T_s and t_{dep} are the sintering temperature and the deposition time, respectively.

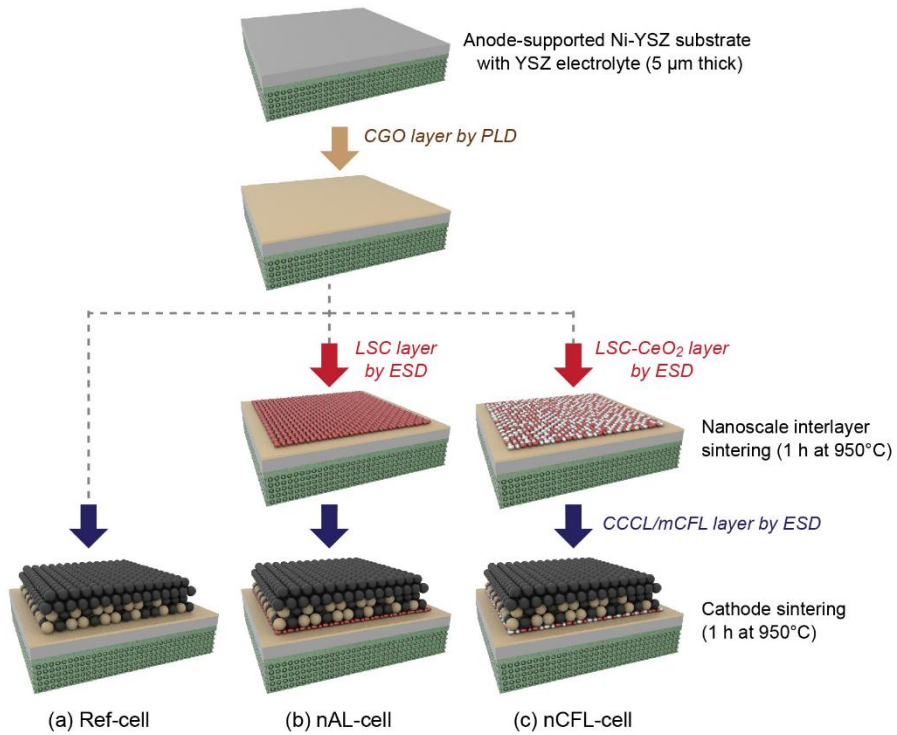


Figure 3.1. Schematic illustration of the fabrication process for the three different SOFCs using PLD and ESD techniques: (a) Ref, (b) nAL, and (c) nCFL cells.

3.3. Results and Discussion

In this chapter, we developed two different multiscale electrode architecturing technologies, a ceramic thin film fabrication technology and a novel infiltration technology, via a precursor-solution ESD process. To specifically analyze the results of two different technologies, we separately described the results and discussion of each technologies. The results and discussion of optimization of precursor-solution ESD and applying to a ceramic thin film fabrication technology were described from part 3.3.1. to 3.3.3., and the results and discussion of applying to a novel infiltration technology were described from part 3.3.4. to 3.3.6..

3.3.1. Principles of precursor-solution electrospray deposition process

The processing of the newly proposed nanoscale cathodes interlayers can be divided into: (1) preparation of the precursor solution; and (2) fabrication of the layers using the modified electrospray process with the prepared precursor solutions. As described in the experimental section, we prepared LSC and LSC-CeO₂ precursor solutions for preparing the nAL and nCFL, respectively. XRD analysis was performed after subjecting the precursor solutions to various heat-treatment conditions in order to optimize the process to achieve the desired crystalline phases of LSC and CeO₂. As shown in **Figure 3.2a**, the crystalline phase of LSC was successfully obtained after heat treatment at 950°C for 1 h. The mixed

precursor solution for preparing the nCFL also produced well-crystallized LSC and CeO₂ phases under the same heat-treatment conditions, where the two independent phases were observed, without any notable secondary phases.

The precursor-solution electro spray process is inherently unsuitable for forming nanolayers as the cone-jet mode is difficult to achieve using a precursor solution⁴³⁻⁴⁶. In particular, water, which is the most common solvent used to dissolve precursors for SOFC materials, has a large surface tension (three times higher than that of ethanol)^{47,48}. Furthermore, the precursor solution with a low solids loading and high organic content should be supplied at a low flow rate; this makes the Taylor cone unstable, and results in a dripping mode or multi-jet mode of electro spraying, which are undesirable for formation of nanolayers. The empirical relationship between the processing parameters [i.e., solvent surface tension (γ), nozzle diameter (r), nozzle-to-tip distance, etc.] and the applied voltage (V_n) shown below describes the inherent limitations of the conventional electro spray technique with the precursor solution:

$$V_n = C \left(\frac{2r\gamma \cdot \cos \theta_o}{\varepsilon_o} \right)^{1/2} \cdot \ln \left(\frac{4H}{r} \right), \quad (1)$$

where C is the constant, ε_o is the permittivity of free space, and θ_o is the cone half-angle⁴⁹. Therefore, in this study, we modified the precursor-solution electro spray method to make it more suitable for fabricating nanoscale layers. Here, we chose a fused-silica capillary with a diameter of several micrometers, instead of the typical stainless-steel nozzle with a

diameter of several hundred micrometers. In addition, we optimized several electro spray processing parameters, such as the applied voltage, nozzle-to-substrate distance, and flow rate, in order to achieve nanoscale layers from a precursor solution. **Figure 3.3** shows various nanoscale layers fabricated using the precursor-solution electro spray method as a function of several processing variables. We achieved a stable cone-jet mode during electro spraying using a silica capillary with 8- μm diameter, 13-kV applied voltage, and water-based precursor solutions for LSC and LSC-CeO₂, resulting in homogeneous film deposition. **Table 3.1** lists the optimized precursor-solution electro spray conditions.

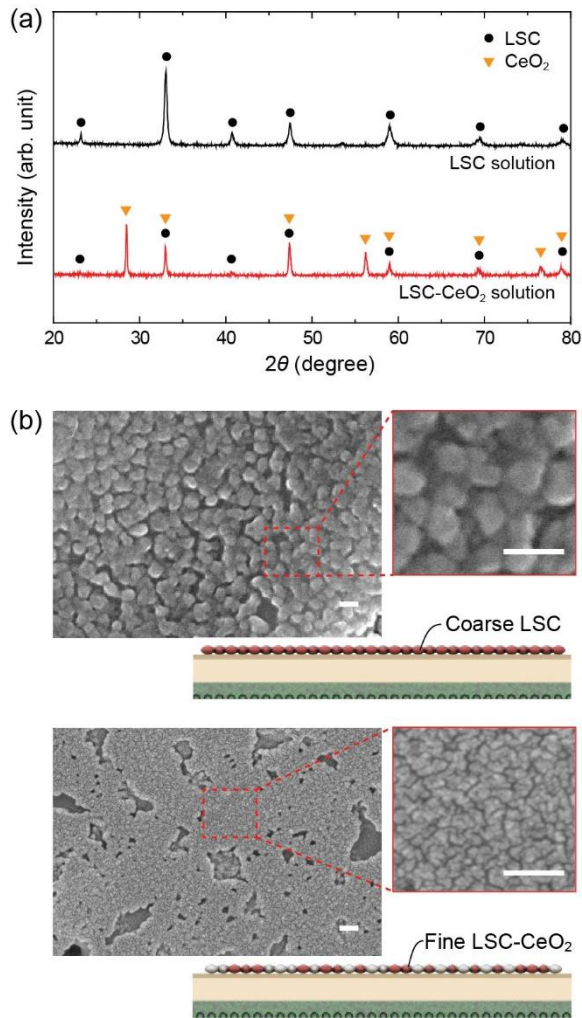


Figure 3.2. Results of the structural analysis of LSC and LSC-CeO₂ deposited by precursor-solution electrospray method and sintered at 950°C for 1 h. (a) XRD patterns of two precursor solutions indexed to LSC and CeO₂. (b) Low- and high-magnification surface SEM images of the deposited (top) LSC nAL and (bottom) LSC-CeO₂ nCFL. All scale bars correspond to 100 nm.

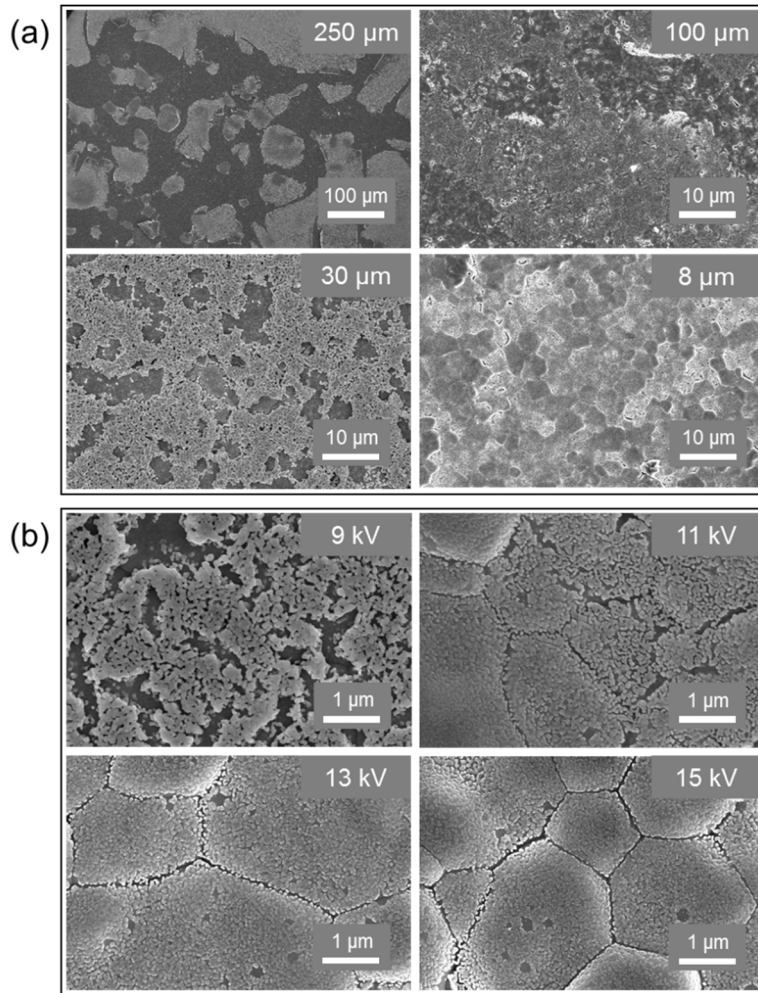


Figure 3.3. Surface SEM images showing microstructures of as-sintered LSC layer fabricated by the precursor-solution electrospray method with (a) different nozzle-tip diameters and (b) applied voltages.

3.3.2. Structural analysis of fabricated nanoscale interlayers

As shown in **Figure 3.2b**, uniform LSC and LSC–CeO₂ thin films were fabricated, but different grain sizes were observed. The single-phase LSC layer had a grain size of ~80 nm, which was around four times that of the LSC–CeO₂ composite layer (~20 nm). In the case of the LSC–CeO₂ layer, as CeO₂ has a higher densification temperature than LSC^{50,51}, it was distributed homogeneously between the LSC nanoparticles and inhibited the sintering and grain growth of LSC nanoparticles^{52,53}.

Figure 3.4 shows cross-sectional SEM images and corresponding schematic illustrations of the full test cells prepared as described in the experimental section. The LSC and LSC–CeO₂ nanoscale interlayers showed both similarities and differences from a mechanical and electrochemical viewpoint. Both interlayers had grain boundaries less than 80 nm, which is at least one-fifth the size of grains forming the mCFL. Both layers thus served a mechanical-structural function and enhanced the interfacial adhesion between the powder-based mCFL and the PLD-based CGO BL. The different compositions of the single-phase LSC and multiphase LSC–CeO₂ layers enabled them to perform different roles at the cathode. The LSC–CeO₂ composite layer is expected to form numerous triple-phase boundaries (between the electron conducting and ion conducting phases, and the gas phase in the pore), thereby providing more electrochemical reaction sites for the ORR to occur³. Furthermore, as this composite structure has an intermediate coefficient of thermal expansion between those of the CGO/YSZ layer and the LSC cathode, it can reduce

mechanical degradation associated with the thermal expansion mismatch between the electrolyte and cathode layers⁵⁴. According to the roles of the two interlayers, we hereafter refer to the LSC and LSC–CeO₂ layers as nAL (nanoscale-adhesion layer) and nCFL (nanoscale-cathode-functional layer), respectively. The cross-sectional SEM images shown in **Figure 3.4** after the final sintering process indicated that the nAL and nCFL structures improved interfacial connectivity and increased the number of electrochemical reaction pathways in the cathode structure.

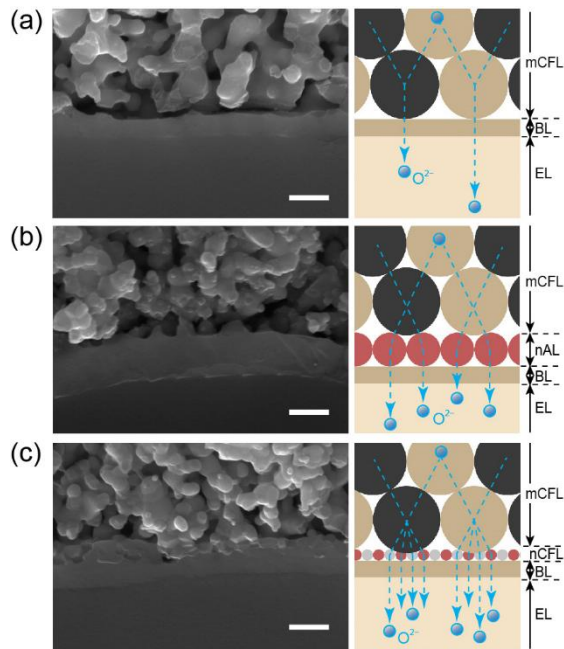


Figure 3.4. Cross-sectional SEM images and schematic illustrations of various interlayer structures between the BL/EL and mCFL: (a) Ref, (b) nAL, and (c) nCFL cells. All scale bars correspond to 300 nm.

3.3.3. Electrochemical performance of fuel cells including nanoscale interlayers

To investigate the electrochemical performance of the nAL and nCFL fabricated using the modified precursor-solution electro spray method, the three different SOFCs (Ref, nAL, and nCFL cells) were tested. All SOFC cells had the same multilayer structure, including the Ni-YSZ anode, YSZ EL, CGO BL, LSC-CGO mCFL, and LSC CCCL, while the nanoscale interlayer between the BL and mCFL differed for each sample. We obtained *I-V-P* curves, which evaluate the ability of the cell to generate power, of the individual test cells at 650 and 550°C with hydrogen and air as the fuel and oxidant, respectively. As shown in **Figure 3.5**, the open-circuit voltage of all test cells was above 1.1 V, which is close to the theoretical value, confirming that the cells were gas impermeable, i.e., the EL was fully dense and the cells were perfectly sealed. The nAL and nCFL cells with their unique nanoscale interlayers showed maximum power density (P_{\max}) values of 1.108 and 1.150 W cm⁻² at 650°C, which corresponded to an increase of ~18% and ~13%, respectively, compared to the P_{\max} of Ref-cell.

Figure 3.6 shows the corresponding impedance spectra measured at the two different temperatures under a cell voltage (V_{cell}) of 0.75 V. Using the impedance spectra, the total cell area-specific resistance (ASR_{cell}) was decomposed into the Ohmic (ASR_{ohm}) and the polarization (ASR_{pol}) components, where $\text{ASR}_{\text{cell}} = \text{ASR}_{\text{ohm}} + \text{ASR}_{\text{pol}}$. These values are summarized in **Table 3.2**, along with the P_{\max} values. The increase in P_{\max} of the two cells containing the nanoscale interfacial layers for both

measured temperatures was a result of the decrease in both ASR_{ohm} and ASR_{pol} , which decreased by $\sim 17\%$ and $\sim 7\%$, respectively, on average compared to those of Ref-cell. In particular, the nCFL-cell showed significantly lower ASR_{ohm} and ASR_{pol} values, by $\sim 28\%$ and $\sim 7\%$, respectively at 650°C , suggesting that this structure provided more effective ASR reduction than nAL.

The significant reduction in ASR observed for the two test cells with the nanoscale interlayers can be explained by their microstructure (**Figure 3.2 and 3.4**). The nanoscale interlayers deposited between the BL and mCFL resulted in an increased number of nanoscale ion diffusion paths and ORR-active sites, resulting in improved cell performance. As the nCFL contained LSC–CeO₂ nanoparticles with a much smaller size than the nAL nanoparticles, they offered faster oxygen-ion transport and higher ORR activity, further reducing the ASR⁵⁵. In addition, the increased interfacial strength between the PLD-based BL and the powder-based mCFL due to the incorporation of the nanoscale interlayers resulted in a further reduction in ohmic resistance.

Cell type	650°C			550°C		
	P_{\max} (W cm ⁻²)	ASR _{ohm} (Ω·cm ²)	ASR _{pol} (Ω·cm ²)	P_{\max} (W cm ⁻²)	ASR _{ohm} (Ω·cm ²)	ASR _{pol} (Ω·cm ²)
Ref-cell	0.976	0.096	0.184	0.292	0.320	0.762
nAL-cell	1.108	0.080	0.169	0.314	0.301	0.730
nCFL-cell	1.150	0.069	0.171	0.330	0.263	0.679

Table 3.2. P_{\max} , ASR_{ohm}, and ASR_{pol} of each cell at operating temperatures of 650 and 550°C. All ASR results are estimated from impedance spectra under $V_{\text{cell}} = 0.75$ V at 650 and 550°C.

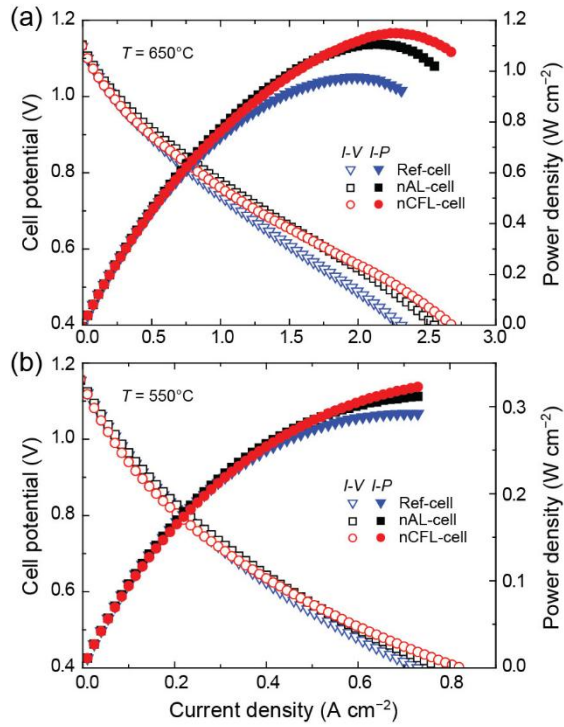


Figure 3.5. Comparison of the I - V - P curves for the three different cells (Ref, nAL, and nCFL cell) measured at (a) 650 and (b) 550°C.

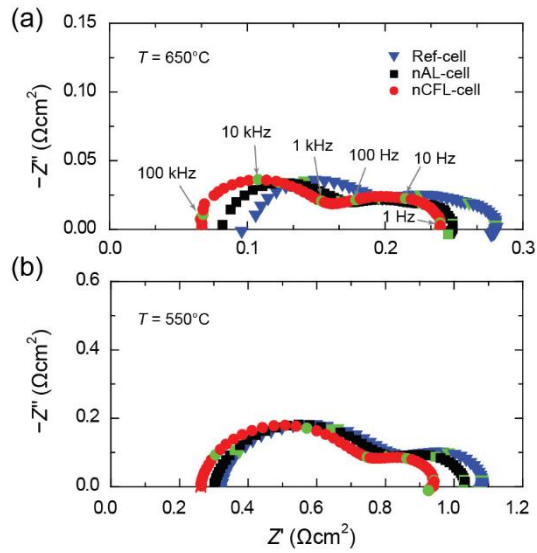


Figure 3.6. Comparison of AC impedance spectra of the three different cells (Ref, nAL, and nCFL cell) measured at (a) 650 and (b) 550°C and a cell voltage of 0.75 V.

3.3.4. Principles of gelation and solution via precursor-solution ESD process

In general, the infiltration process is difficult to proceed when the viscosity of the precursor-solution is high or gelation occurs. Thus, the traditional infiltration process was performed when the precursor-solution was in a liquid state. However, since the precursor-solution during infiltration is already fluid, there exists limited feature in controlling flow in-situ and is one of the major issues existing in the infiltration process of the conventional dropping process. Therefore, an original approach is demanded, and we introduced an ESD method to solve the problems.

The precursor-solution ESD method was able to fabricate ceramic thin films with a thickness of 100 nm or less which cannot be realized by the conventional powder-suspension ESD method through the spray of precursor-solution itself. We established stable spray conditions using a nozzle tip with a diameter of 8 μm which is dramatically reduced than the conventional 250 μm . This is because the surface tension of the DI water, which is the base solvent of the precursor-solution, is larger than three times that of the ethyl alcohol, which is used as the base solvent of the powder-suspension^{47,48}. As the diameter of nozzle tip decreased, the flow rate also decreased significantly, and the droplet size also became smaller^{44,47}. We have developed a novel infiltration process using reduced droplet size feature. As shown in **Figure. 3.7**, the new infiltration process using humidification can be divided into (1) gelation of precursor-solution in the end of the nozzle-tip, (2) deposition of gelled nano-droplets onto a

porous skeleton structure and (3) infiltration into the porous skeleton structure with solution of nano-droplets by humidification. There are two types of gelation phenomena that lose fluidity and viscosity: chemical gelation by covalent bonding and physical gelation by aggregation. Among them, the gelation phenomenon at the end of the nozzle-tip can be regarded as physical gelation, because the nano-droplets formed at the end of nozzle-tip by electrodynamic stress have a gel characteristic through solvent evaporation^{19,46}. As shown in the middle schematics of **Figure 3.7**, the gelled nano-droplets are deposited as a dendrite structure on the skeleton structure. Then, when humidifying the sample chamber, the physically gelled precursor-solution becomes solution again because the base solvent of the precursor-solution is DI water. The fluidity of the gels deposited with the dendrite structure increases by solution, and the precursor-solution is infiltrated into the porous skeleton structure. This infiltration process using the precursor-solution ESD method is denoted as ESD infiltration process.

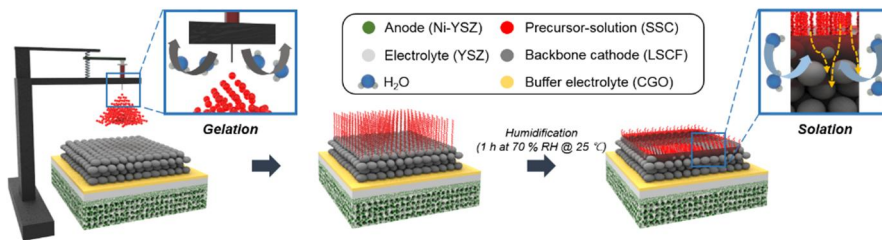


Figure 3.7. Schematics of the principles in sol-to-gel and gel-to-sol reversible reaction of humidification assisted precursor-solution electrospray deposition process.

3.3.5. Structural characteristics of conventional infiltration and ESD infiltration

Humidification conditions were used as variables to control the degree of infiltration, which was difficult to implement in conventional infiltration process. As shown in **Figure 3.8**, precursor-solution ESD method was used to deposit solution on the porous structure, and the samples were exposed for 1 h at 20 %, 30 %, 50 % and 70 % RH at 25 °C, respectively. Structural differences due to four conditions of humidification were analyzed by SEM images. Section-view SEM image shows that the gelled precursor-solution is retained as a dendrite structure on the porous structure in the as-deposited condition. The maintenance of the dendrite structure during SEM analysis demonstrated that it consists of gels with no fluidity. And it is verified that the infiltration gradually progressed as the amount of the humidification increases from 30 % to 50 % and 70 %. From the section-view SEM images in **Figure 3.8**, at the humidification condition of 30 %, it is observed that the precursor-solution was not infiltrated at the bottom of the porous structure, but at 50 % and 70 % condition, the precursor-solution was fully infiltrated into the porous structure. Similarly, the top-view SEM images show that the precursor-solution layer deposited on the porous structure permeates downward from 30 % to 50 % and 70 % condition, respectively. Capability of control the degree of infiltration according to the humidifying conditions is meaningful feature because it allows the structural control independently of the solution viscosity and surface

wettability.

In **Figure 3.9**, the multiscale structures were fabricated using the conventional infiltration process, the ESD infiltration process without humidification, and the ESD infiltration process with 70 % RH humidification for 1 h at 25 °C, and their morphologies were analyzed. 0.1 mol L⁻¹ SSC precursor-solution was used as infiltrating solution and the backbone structure was pre-sintered using spherical shape alumina particles. All three samples were fabricated in the same structure up to the backbone structure. Then, after the infiltration, all samples were heat-treated for 4 h at 1000 °C. **Figure 3.9a** shows the penetration behavior of the conventional infiltration process. It is verified from the schematics that the precursor-solution spreads from the point where it drops. The morphology of the SSC particles attached on the alumina sphere after sintering shows that the nano-catalysts are formed in a band shape similar to the flow of the liquid. And **Figure 3.9b** shows the results of ESD infiltration without humidification. It is confirmed that the nano-catalysts are attached only to the upper end of the alumina spheres and the loaded nano-catalysts are invisible in the alumina structure located at middle height. This is because the precursor-solution uniformly deposited on the alumina structure cannot permeates into the porous structure without assistance of humidification. **Figure 3.9c** shows the results of infiltration through humidification assisted ESD infiltration process. As shown in schematics and SEM images, it is verified that the SSC nano-catalysts are uniformly formed on all alumina spheres. Two factors were brought up for the structural differences of SSC nano-

catalysts after sintering. The first is the direction of penetration. In the conventional infiltration process, the precursor-solution is excessively present in the dropping region, and gradually spreads in the x- and y- axis directions due to the capillary force. While, in the ESD infiltration process, the precursor-solution impregnates into the z-axis by gravity and capillary force during humidification because it is deposited all over the substrate. Therefore, the ESD infiltration process shows better uniform distribution of precursor-solution on x-, y- and z- axis compared to the conventional infiltration. The second is the degree of solution by humidification. In the humidification assisted ESD infiltration process, the movement of the precursor-solution accelerates to the z-axis through the solution phenomenon, but in the ESD infiltration process without humidification, the precursor-solution deposited on the alumina spheres undergoes gelation and sintering without permeation into z-axis. From the above two phenomena, fabricated multiscale structures by three different infiltration processes have different structural characteristics. Then, the effect of applying it to fuel cell electrodes was analyzed.

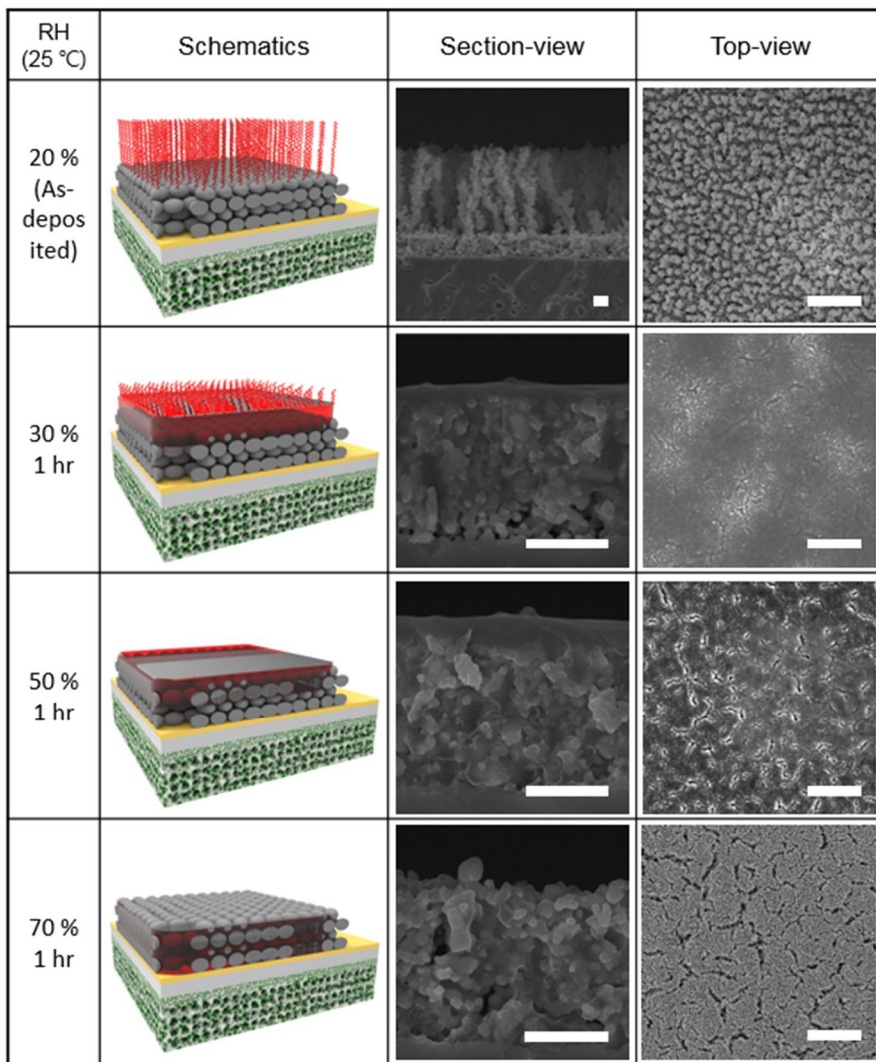


Figure 3.8. Schematics, section-view SEM images and top-view SEM images under the various conditions of humidification after precursor-solution deposition.

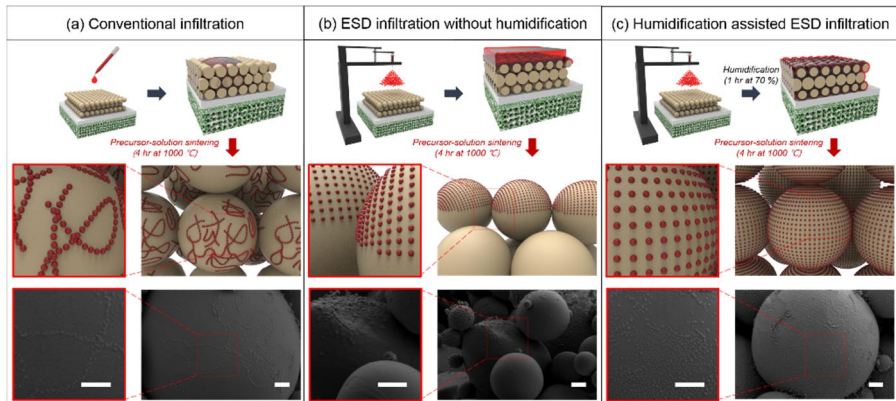


Figure 3.9. SEM images and schematics of infiltrated and sintered SSC precursor-solution into the porous alumina structure via (a) conventional infiltration process, (b) ESD infiltration process without humidification and (c) humidification assisted ESD infiltration process.

3.3.6. Analysis of electrochemical performance of Ref-cell, CI-cell, EI-cell and HEI-cell

Four individual cells were fabricated to identify the electrochemical effects of three different infiltration processes. Flowchart **Figure 3.10** shows the fabrication processes of each cell. All the cells were deposited with a CGO buffer electrolyte layer on a commercial anode-supported cell using a sputtering process, and an LSCF backbone cathode was deposited on a CGO layer via precursor-suspension ESD method. For infiltration process, 0.5 mol L^{-1} SSC precursor-solution was used, and the amount was the same as $5 \text{ }\mu\text{l}$. **Figure 3.11** shows the XRD results of SSC and LSCF after sintering, and it is confirmed that the desired crystalline phases were obtained without any secondary phases in both SSC and LSCF. We obtained electrochemical results of all test cells from $650 \text{ }^\circ\text{C}$ to $500 \text{ }^\circ\text{C}$ at intervals of $50 \text{ }^\circ\text{C}$ under the conditions of supplying air and hydrogen as the oxidant and fuel, respectively. According to the varied infiltration processes, we abbreviate the cell with no infiltration process, with conventional infiltration process, with ESD infiltration process without humidification and with humidification assisted ESD infiltration process as Ref-cell, CI-cell, EI-cell and HEI-cell, respectively.

Figure 3.12 shows electrochemical analysis results of four cells. From the I-V-P curves in **Figure 3.12a**, all cells resulted in an open circuit voltage of 1.1 V to confirm the gas impermeable condition of the electrolyte layer and sealant. The HEI-cell with the developed infiltration

process using humidification showed a peak power density of 1018 mW cm⁻² at 650 °C and maximum performance enhancement of 215 %, 15 % and 18 % over the Ref-cell, CI-cell and EI-cell, respectively. **Figure 3.12b** shows the electrochemical impedance spectra under the condition of OCV at 650 °C. From the upper nyquist plot, it is verified that the total area-specific resistance (ASR_{total}) decreases in the order of Ref-cell, CI-cell, EI-cell and HEI-cell, and from the lower nyquist plot, reduced ohmic area-specific resistance (ASR_{ohm}) in the order of Ref-cell, EI-cell, CI-cell and HEI-cell was confirmed. The HEI-cell resulted in 0.088 Ω cm² ASR_{ohm} under the condition of OCV at 650 °C, which is 71 %, 9 % and 17 % reduced value than the Ref-cell, CI-cell and EI-cell, respectively. One of the critical roles in ASR_{ohm} reduction is the enhanced interfacial strength of CGO electrolyte later and LSCF cathode layer by infiltrated SSC nano-catalysts. At EI-cell, SSC precursor-solution could not penetrate into the electrolyte/cathode interface compared to CI-cell and HEI-cell due to the non-humidification condition. In the case of HEI-cell, since the precursor-solution was uniformly penetrated into the electrolyte/cathode interface of the whole electrode area, the interfacial adhesion property was improved and the ASR_{ohm} was also diminished compared with the CI-cell which infiltrating solution had to be dispersed along the xy plane from the solution dropping point. And, the HEI-cell showed 0.820 Ω cm² ASR_{pol} under the condition of OCV at 650 °C, which is 50 %, 11 % and 4 % decreased value than the Ref-cell, CI-cell and EI-cell, respectively. The ASR_{pol} values decreased in the order of Ref-cell, CI-cell, EI-cell and HEI-

cell. This result can be explained by the individual SEM images of four cells. The SEM images of CI-cell (**Figure 3.13b**), EI-cell (**Figure 3.13c**) and HEI-cell (**Figure 3.13d**) show that the infiltrated SSC nano-catalyst were loaded on the LSCF backbone cathode, but single LSCF backbone cathode exists in the SEM images of Ref-cell (**Figure 3.13a**). In addition, it is verified that the sintered SSC nano-catalysts were uniformly dispersed in HEI-cell, but mainly deposited on the surface of the backbone structure in EI-cell and randomly dispersed in CI-cell. This structural tendency is similar to the result shown in **Figure 3.9**. Therefore, from the morphology of the multiscale electrodes, the result of ASR_{pol} values could be explained. The detailed electrochemical results are summarized in **Table 3.3**.

As a result, homogeneously infiltrated SSC nano-catalysts reduced ASR_{ohm} and ASR_{pol} , leading to increased power of fuel cell. We believe that this advanced architecturing technology of multiscale SOFCs can accelerate the commercialization of SOFCs in the future.

Cell type	At 650°C			At 600°C		
	P_{\max} (mW cm ⁻²)	ASR _{ohm} (Ω·cm ²)	ASR _{pol} (Ω·cm ²)	P_{\max} (mW cm ⁻²)	ASR _{ohm} (Ω·cm ²)	ASR _{pol} (Ω·cm ²)
Ref-cell	323	0.304	1.624	222	0.443	3.292
CI-cell	887	0.097	0.925	544	0.171	1.641
EI-cell	861	0.106	0.856	540	0.179	1.538
HEI-cell	1018	0.088	0.820	624	0.158	1.425

Table 3.3. P_{\max} , ASR_{ohm}, and ASR_{pol} of each cell at operating temperatures of 650 and 600°C. All results are obtained from impedance spectra under the condition of open circuit voltage (OCV) at 650 and 600°C.

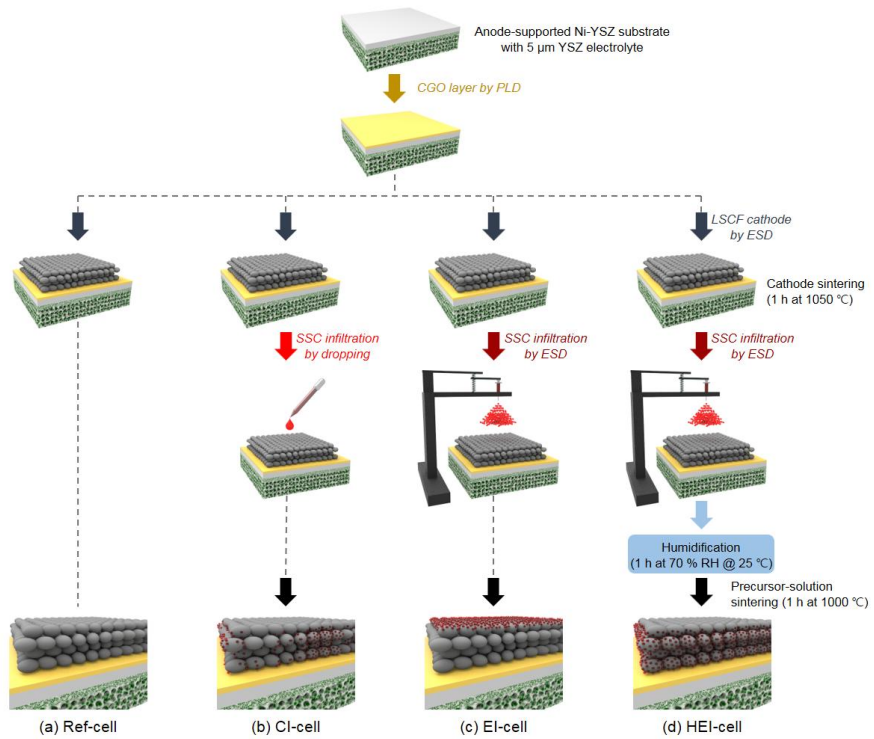


Figure 3.10. Schematic illustration of fabrication of four different SOFCs multiple infiltration processes (a) Ref-, (b) CI-, (c) EI- and (d) HEI- cells.

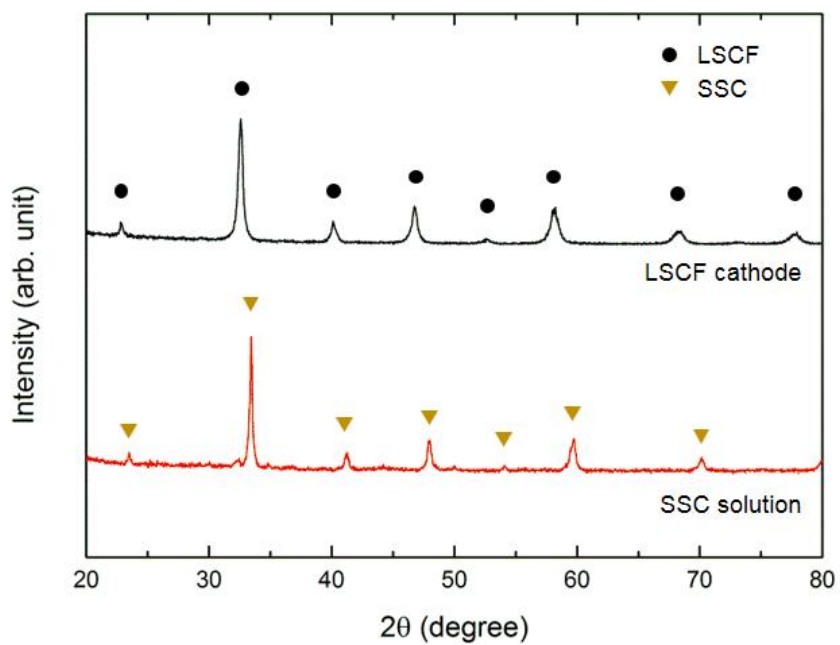


Figure 3.11. XRD results of as-sintered LSCF powder and SSC precursor-solution at 1050 °C for 1 h and 1000 °C for 1 h, respectively.

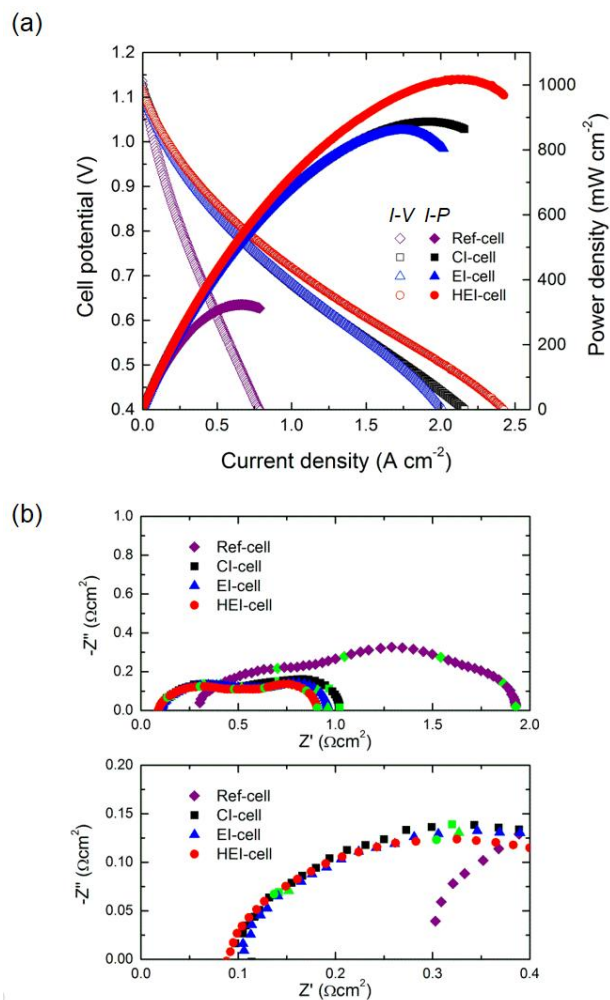


Figure 3.12. Electrochemical characteristics of four different cells (Ref-, Cl-, EI- and HEI- cell). (a) I - V - P curves at 650°C, (b) impedance spectra under the condition of OCV at 650°C.

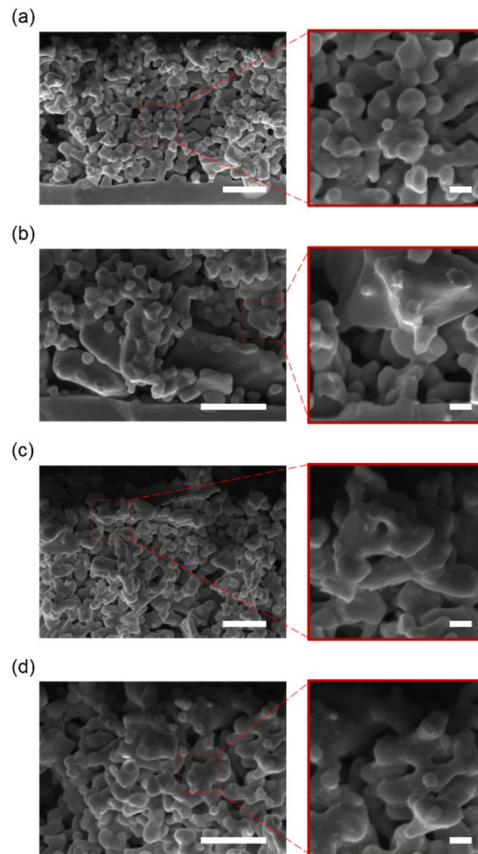


Figure 3.13. SEM images of (a) Ref-cell, (b) CI-cell, (c) EI-cell and (d) HEI-cell after cell test.

3.4. Conclusions

In summary, we developed a ceramic thin film fabrication technology and an infiltration technology using a novel modified precursor-solution electrospray method and demonstrated improved SOFC performance with significant reduction of Ohmic and polarization resistances.

From the optimization of precursor-solution ESD, fabricated ceramic thin film showed no surface defects and formed a uniform layer. In order to reduce the particle size, we fabricated an LSC–CeO₂ thin film with particle size of <20 nm from a mixed precursor solution. These ceramic thin film structures were used as nanoscale interlayers between the PLD-based BL and the powder-based mCFL to improve the electrochemical transport and mechanical adhesion. The nAL and nCFL cells both showed significantly higher maximum power density than the reference cell, which was attributed to better adhesion between the BL and mCFL, an increase in the number of ORR active sites, and enhanced oxygen-ion transport, which reduced losses due to the ASR_{ohm} and ASR_{pol}.

Then, from a novel infiltration technology, the multiscale structure fabricated by the ESD infiltration process using humidification showed uniformly dispersed nano-catalysts compared with the conventional infiltration process using dropping and the ESD infiltration process without humidification. The HEI-cell resulted in a peak power density of 583 mW cm⁻² at 650 °C, which is 80 %, 86 % and 42 % higher than that of Ref-cell, CI-cell and EI-cell, respectively. ASR_{total} was also reduced due to the

decrease of ASR_{ohm} and ASR_{pol} derived from strengthened electrolyte/cathode interfacial adhesion by uniformly infiltrated SSC precursor-solution on the entire surface of the electrode and uniformly generated SSC nano-catalysts, which have high catalytic activity, on the backbone cathode, respectively.

High-performance SOFCs with advanced cathode structures were demonstrated using the modified precursor-solution electrospray method, which is thought to have many advantages compared to vacuum-deposition processes. We propose that this is an effective method for producing highly active and well-integrated nanoscale interlayers and homogeneously formed nano-catalyst. The method can be easily modified to produce structures of various materials by using tailored precursor mixtures. We expect that this method can be used in the development of next-generation SOFCs with higher reliability and performance due to more stable cathodes with improved mechanical properties and electrochemical performance.

3.5. References

1. Wachsman, E. D.; Lee, K. T. Lowering the temperature of solid oxide fuel cells. *Science* **332**, 935-939 (2011).
2. Adler, S. B. Factors governing oxygen reduction in solid oxide fuel cell cathodes. *Chemical Reviews* **104**, 4791-4843 (2004).
3. Singhal, S. C. Advances in solid oxide fuel cell technology. *Solid State Ionics* **135**, 305-313 (2000).
4. Shao, Z.; Halle, S. M. A high-performance cathode for the next generation of solid-oxide fuel cells. *Nature* **431**, 170-173 (2004).
5. Minh, N. Q. Ceramic Fuel Cells. *Journal of the American Ceramic Society* **76**, 563-588 (1993).
6. Evans, A.; Bieberle-Hutter, A.; Rupp, J. L. M.; Gauckler, L. J. Review on microfabricated micro-solid oxide fuel cell membranes. *Journal of Power Sources* **194**, 119-129 (2009).
7. Park, J. H.; Han, S. M.; Yoon, K. J.; Kim, H.; Hong, J.; Kim, B. K.; Lee, J. H.; Son, J. W. Impact of nanostructured anode on low-temperature performance of thin-film-based anode-supported solid oxide fuel cells. *Journal of Power Sources* **315**, 324-330 (2016).
8. Bae, K.; Jang, D. Y.; Jung, H. J.; Kim, J. W.; Son, J. W.; Shim, J. H. Micro ceramic fuel cells with multilayered yttrium-doped barium cerate and zirconate thin film electrolytes. *Journal of Power Sources* **248**, 1163-1169 (2014).
9. An, J.; Kim, Y. B.; Park, J.; Gür, T. M.; Prinz, F. B. Three-dimensional nanostructured bilayer solid oxide fuel cell with 1.3 W/cm² at 450 °C. *Nano Letters* **13**, 4551-4555 (2013).
10. Noh, H. S.; Yoon, K. J.; Kim, B. K.; Je, H. J.; Lee, H. W.; Lee, J. H.; Son, J. W. Thermo-mechanical stability of multi-scale-architected thin-film-based solid oxide fuel cells assessed by thermal cycling tests. *Journal of Power Sources* **249**, 125-130 (2014).
11. Soyez, G.; Eastman, J. A.; Thompson, L. J.; Bai, G. R.; Baldo, P. M.;

- McCormick, A. W.; DiMelfi, R. J.; Elmustafa, A. A.; Tambwe, M. F.; Stone, D. S. Grain-size-dependent thermal conductivity of nanocrystalline yttria-stabilized zirconia films grown by metal-organic chemical vapor deposition. *Applied Physics Letters* **77**, 1155–1157 (2000).
12. Oh, E. O.; Whang, C. M.; Lee, Y. R.; Park, S. Y.; Prasad, D. H.; Yoon, K. J.; Son, J. W.; Lee, J. H.; Lee, H. W. Extremely thin bilayer electrolyte for solid oxide fuel cells (SOFCs) fabricated by chemical solution deposition (CSD). *Advanced Materials* **24**, 3373–3377 (2012).
13. Choi, Y.-G.; Park, J.-Y.; Son, J.-W.; Lee, J.-H.; Je, H.-J.; Kim, B.-K.; Lee, H.-W.; Yoon, K. J. Ceria-based electrolyte reinforced by sol–gel technique for intermediate-temperature solid oxide fuel cells. *International Journal of Hydrogen Energy* **38**, 9867–9872 (2013).
14. Noh, H.-S.; Hong, J.; Kim, H.; Yoon, K. J.; Kim, B.-K.; Lee, H.-W.; Lee, J.-H.; Son, J.-W. Scale-up of thin-film deposition-based solid oxide fuel cell by sputtering, a commercially viable thin-film technology. *Journal of The Electrochemical Society* **163**, F613–F617 (2016).
15. Sholklapper, T. Z.; Jacobson, C. P.; Visco, S. J.; Dejonghe, L. C. Synthesis of dispersed and contiguous nanoparticles in solid oxide fuel cell electrodes. *Fuel Cells* **8**, 303–312 (2008).
16. Jiang, S. P. Nanoscale and nano-structured electrodes of solid oxide fuel cells by infiltration: Advances and challenges. *International Journal of Hydrogen Energy* **37**, 449–470 (2012).
17. Chao, C.-C.; Hsu, C.-M.; Cui, Y.; Prinz, F. B. Improved solid oxide fuel cell performance with nanostructured electrolytes. *ACS Nano* **5**, 5692–5696 (2011).
18. Sharma, R. K.; Burriel, M.; Dessemond, L.; Bassat, J.-M.; Djurado, E. Design of interfaces in efficient $\text{Ln}_2\text{NiO}_{4+\delta}$ ($\text{Ln} = \text{La}, \text{Pr}$) cathode for SOFCs application. *J. Mater. Chem. A* 12451–12462 (2016). doi:10.1039/C6TA04845E
19. Kim, J. H.; Shin, S. S.; Noh, H. S.; Son, J. W.; Choi, M.; Kim, H. Tailoring ceramic membrane structures of solid oxide fuel cells via polymer-assisted

- electrospray deposition. *Journal of Membrane Science* **544**, 234–242 (2017).
20. Martin, S.; Garcia-Ybarra, P. L.; Castillo, J. L. Electrospray deposition of catalyst layers with ultra-low Pt loadings for PEM fuel cells cathodes. *Journal of Power Sources* **195**, 2443–2449 (2010).
 21. Martin, S.; Garcia-Ybarra, P. L.; Castillo, J. L. High platinum utilization in ultra-low Pt loaded PEM fuel cell cathodes prepared by electrospraying. *International Journal of Hydrogen Energy* **35**, 10446–10451 (2010).
 22. Martinez-Vazquez, B.; Sanchez, D. G.; Castillo, J. L.; Friedrich, K. A.; Garcia-Ybarra, P. L. Scaling-up and characterization of ultralow-loading MEAs made-up by electrospray. *International Journal of Hydrogen Energy* **40**, 5384–5389 (2015).
 23. Yin, Y. X.; Xin, S.; Wan, L. J.; Li, C. J.; Guo, Y. G. Electrospray synthesis of silicon/carbon nanoporous microspheres as improved anode materials for lithium-ion batteries. *Journal of Physical Chemistry C* **115**, 14148–14154 (2011).
 24. Xu, Y.; Zhu, Y.; Han, F.; Luo, C.; Wang, C. 3D Si/C fiber paper electrodes fabricated using a combined electrospray/electrospinning technique for Li-ion batteries. *Advanced Energy Materials* **5**, 1–7 (2015).
 25. Li, Y.; Li, P.; Yang, M.; Lei, S.; Chen, Y.; Guo, X. A surface acoustic wave humidity sensor based on electrosprayed silicon-containing polyelectrolyte. *Sensors and Actuators, B: Chemical* **145**, 516–520 (2010).
 26. Diagne, H. A.; Lumvreras, M. Elaboration and characterization of tin oxide lanthanum oxide mixed layers prepared by electrostatic spray pyrolysis technique. *Sensors and Actuators, B* **3957**, 1–8 (2001).
 27. Xu, J.; Liu, C.; Hsu, P. C.; Liu, K.; Zhang, R.; Liu, Y.; Cui, Y. Roll-to-roll transfer of electrospun nanofiber film for high-efficiency transparent air filter. *Nano Letters* **16**, 1270–1275 (2016).
 28. Yun, K. M.; Hogan, C. J.; Matsubayashi, Y.; Kawabe, M.; Iskandar, F.; Okuyama, K. Nanoparticle filtration by electrospun polymer fibers. *Chemical Engineering Science* **62**, 4751–4759 (2007).

29. Li, A.; Luo, Q.; Park, S. J.; Cooks, R. G. Synthesis and catalytic reactions of nanoparticles formed by electrospray ionization of coinage metals. *Angewandte Chemie - International Edition* **53**, 3147–3150 (2014).
30. Joshi, B. N.; Yoon, H.; Na, S. H.; Choi, J. Y.; Yoon, S. S. Enhanced photocatalytic performance of graphene-ZnO nanoplatelet composite thin films prepared by electrostatic spray deposition. *Ceramics International* **40**, 3647–3654 (2014).
31. Lee, H.; Lee, S.; Lee, T.; Park, S.; Shin, D. Long term stability of porosity gradient composite cathode controlled by electro-static slurry spray deposition. *International Journal of Hydrogen Energy* **42**, 3748–3752 (2017).
32. Choi, S. H.; Kim, S. W.; Hwang, C. S.; Lee, M. H. Freestanding micro-SOFCs with electrodes prepared by electrostatic spray deposition. *Fuel Cells* **14**, 332–335 (2014).
33. Lee, H.; Choi, J.; Park, I.; Shin, D. Electrochemical performance of continuously gradient composite cathode fabricated by electro-static slurry spray deposition. *International Journal of Hydrogen Energy* **39**, 14322–14327 (2014).
34. Park, I.; Ahn, J.; Im, J.; Choi, J.; Shin, D. Influence of rheological characteristics of YSZ suspension on the morphology of YSZ films deposited by electrostatic spray deposition. *Ceramics International* **38**, S481–S484 (2012).
35. Lee, H.; Park, I.; Park, J.; Lee, G.; Shin, D. Effects of dual porosity honeycomb structure in SSC-SDC composite cathode for SOFCs. *International Journal of Hydrogen Energy* **40**, 11998–12002 (2015).
36. Sar, J.; Dessemond, L.; Djurado, E. Electrochemical properties of graded and homogeneous $\text{Ce}_{0.9}\text{Gd}_{0.1}\text{O}_{2-\delta}$ - $\text{La}_{0.6}\text{Sr}_{0.4}\text{Co}_{0.2}\text{Fe}_{0.8}\text{O}_{3-\delta}$ composite electrodes for intermediate-temperature solid oxide fuel cells. *International Journal of Hydrogen Energy* **41**, 17037–17043 (2016).
37. Princivalle, A.; Perednis, D.; Neagu, R.; Djurado, E. Microstructural investigations of nanostructured $\text{La}(\text{Sr})\text{MnO}_{3-\delta}$ films deposited by

- electrostatic spray deposition. *Chemistry of Materials* **16**, 3733–3739 (2004).
38. Marinha, D.; Dessemond, L.; Cronin, J. S.; Wilson, J. R.; Barnett, S. A.; Djurado, E. Microstructural 3D reconstruction and performance evaluation of LSCF cathodes obtained by electrostatic spray deposition. *Chemistry of Materials* **23**, 5340–5348 (2011).
 39. Huang, J. B.; Chang, C. L.; Hsu, C. S.; Hwang, B. H. Electrostatic spray deposition of doped ceria films. *Fuel Cells* **10**, 1095–1099 (2010).
 40. Kim, J.; Park, Y.; Sung, D. J.; Moon, S.; Lee, K. B.; Hong, S. I. Preparation of thin film YSZ electrolyte by using electrostatic spray deposition. *International Journal of Refractory Metals and Hard Materials* **27**, 985–990 (2009).
 41. Birnie III, D. P. Spin Coating Technique. *Sol-Gel Technologies for Glass Producers and Users* 49–55 (2004).
 42. Kim, S. J.; Choi, M. B.; Park, M.; Kim, H.; Son, J. W.; Lee, J. H.; Kim, B. K.; Lee, H. W.; Kim, S. G.; Yoon, K. J. Acceleration tests: Degradation of anode-supported planar solid oxide fuel cells at elevated operating temperatures. *Journal of Power Sources* **360**, 284–293 (2017).
 43. Hong, S. C.; Lee, G.; Ha, K.; Yoon, J.; Ahn, N.; Cho, W.; Park, M.; Choi, M. Precise morphology control and continuous fabrication of perovskite solar cells using droplet-controllable electrospray coating system. *ACS Applied Materials and Interfaces* **9**, 7879–7884 (2017).
 44. Rietveld, I. B.; Kobayashi, K.; Yamada, H.; Matsushige, K. Electrospray deposition, model and experiment: Toward general control of film morphology. *The journal of physical chemistry B* **110**, 23351–23364 (2006).
 45. Park, I.; Kim, S. B.; Hong, W. S.; Kim, S. S. Classification of electrohydrodynamic spraying modes of water in air at atmospheric pressure. *Journal of Aerosol Science* **89**, 26–30 (2015).
 46. Jaworek, A.; Sobczyk, A. T. Electrospraying route to nanotechnology: An overview. *Journal of Electrostatics* **66**, 197–219 (2008).
 47. Park, I.; Hong, W. S.; Kim, S. B.; Kim, S. S. Experimental investigations

- on characteristics of stable water electrospray in air without discharge. *Physical Review E* **95**, 1–8 (2017).
48. Jiang, H.; Zhao, Y.; Wang, J.; Zhao, F.; Liu, R.; Hu, Y. Density and surface tension of pure ionic liquid 1-butyl-3-methyl-imidazolium l-lactate and its binary mixture with alcohol and water. *Journal of Chemical Thermodynamics* **64**, 1–13 (2013).
 49. Smith, D. P. H. The Electrohydrodynamic Atomization of Liquids. *IEEE Transactions on Industry Applications* **IA-22**, 527–535 (1986).
 50. Dieterle, L.; Bockstaller, P.; Gerthsen, D.; Hayd, J.; Ivers-Tiffée, E.; Guntow, U. Microstructure of nanoscaled $\text{La}_{0.6}\text{Sr}_{0.4}\text{CoO}_{3-\delta}$ cathodes for intermediate-temperature solid oxide fuel cells. *Advanced Energy Materials* **1**, 249–258 (2011).
 51. Kleinlogel, C.; Gauckler, L. J. Sintering of nanocrystalline CoO_2 ceramics. *Advanced Materials* **13**, 1081–1085 (2001).
 52. Zhang, X.; Liu, L.; Zhao, Z.; Tu, B.; Ou, D.; Cui, D.; Wei, X.; Chen, X.; Cheng, M. Enhanced oxygen reduction activity and solid oxide fuel cell performance with a nanoparticles-loaded cathode. *Nano Letters* **15**, 1703–1709 (2015).
 53. Hwang, H. J.; Moon, J. W.; Lee, S.; Lee, E. A. Electrochemical performance of LSCF-based composite cathodes for intermediate temperature SOFCs. *Journal of Power Sources* **145**, 243–248 (2005).
 54. Park, S. Y.; Ji, H. I.; Kim, H. R.; Yoon, K. J.; Son, J. W.; Kim, B. K.; Je, H. J.; Lee, H. W.; Lee, J. H. Structural optimization of (La, Sr) CoO_3 -based multilayered composite cathode for solid-oxide fuel cells. *Journal of Power Sources* **228**, 97–103 (2013).
 55. Steele, B. C. H.; Bae, J. M. Properties of $\text{La}_{0.6}\text{Sr}_{0.4}\text{Co}_{0.2}\text{Fe}_{0.8}\text{O}_{3-x}$ (LSCF) double layer cathodes on gadolinium-doped cerium oxide (CGO) electrolytes - II. Role of oxygen exchange and diffusion. *Solid State Ionics* **106**, 255–261 (1998).

Chapter 4.

Three-Dimensional Ceramic Multilayer Architectures for High-Performance Solid Oxide-Fuel Cells

4.1. Introduction

Conventional imprint lithography is well known as one of the most popular pattern transfer techniques along with photolithography, and has been extensively used as an economical microfabrication process in a broad range of industries¹⁻³. This process is based on the basic principle of creating patterns by engraving structures onto a resin coated on a substrate with heat or ultraviolet (UV) radiation while pressing the patterned original mold or replica⁴⁻⁶. In particular, the imprinting process that utilizes the fluidity and mechanical deformation of a resin in high-temperature/high-pressure conditions can be performed in a liquid and polymeric solid phases. Correspondingly, it has excellent versatility in the fabrication of micro- and nanoscale pattern structures with low cost and high throughput⁷⁻⁹.

These imprinting processes have been used in a variety of ways as a new problem-solving tool in cutting-edge research studies on renewable energy, thus achieving novel, three-dimensional (3D) architectures. There

are a number of previous results that have confirmed the unique physical/chemical phenomena (*e.g.*, photon management¹⁰⁻¹², plasmonics¹³⁻¹⁵, wettability control¹⁶⁻¹⁸, dry adhesive¹⁹⁻²¹, etc.) and improved cell performance (or efficiency)^{22,23} by fabricating micro- and/or nanoscale patterns in various cell configurations. Following the basic principles of the imprinting process based on the fluidity and mechanical deformation of a resin, most research activities have been focused on organic-based processes and their applications at room-temperature conditions (*e.g.*, photovoltaic cells²⁴⁻²⁶, proton-exchange membrane fuel cells^{8,22,23}, batteries²⁷⁻²⁹, etc.). By contrast, some research fields that utilize ceramic materials with brittle and rigid physical properties have been unable to apply such imprinting process, and have not benefited from it.

Solid oxide fuel cells (SOFC, also known as ceramic fuel cells), have generated increased scientific interest as one of the next-generation, high-efficiency energy device, that generally have a multilayer planar structure composed of two porous electrodes and a dense electrolyte^{30,31}. Despite the fact that all components are solid-state, and in view of the need to increase the reactive surface area (A_{cathode}) in SOFCs, only a limited number of studies with 3D SOFC structures has been applied to the field of micro-SOFCs³²⁻³⁶. However, these surface patterning techniques have often been performed with conventional top-down fabrication processes, such as etching or laser processing^{35,37}. In the case where silicon substrates have been used, on which it is easier to etch compared to oxides, the achievement of various surface patterning and cell configuration has been simpler in micro-SOFCs^{32-34,36}, but their poor material compatibility and

structural weakness have caused serious problems on cell power output and stability^{34,35}. Accordingly, no prior publications exist in the case of laser processing that reported the expected, notable performance enhancements. This owing to the low-resolution and quality characteristics of this technique that ultimately implements surface patterns by melting or evaporating thick ceramic layers^{37,38}. As a result, the use of conventional top-down fabrication processes to achieve 3D SOFC architectures have not been able to overcome their inherent limitations owing to the unique mechanical properties of ceramics as the core materials of SOFCs, including their brittleness and stiffness.

Herein, we develop a microscale ceramic imprinting (MCI) process using the polymer-to-ceramic matrix transition, including mechanically deformable polymer additives and rearrangeable ceramic particulates. This imprinting process, which can be used regardless of material or cell configuration changes, can fabricate a variety of 3D ceramic multilayer architectures. Furthermore, by applying thin-film deposition techniques, we finally demonstrate notable advances in the 3D architectures of SOFCs pertaining to power performance, stability, and scalability. Using 3D reconstruction and electrochemical impedance spectroscopy (EIS) techniques, we quantitatively analyze the electrochemical characteristics of 3D SOFC architectures, and investigate the origins of performance improvements that result from the 3D interface structures.

4.2. Experimental

Fabrication of microscale patterned polymer molds

The silicon master with wet-etched square-pyramid pattern (a square base with all edges of length 5 μm , pattern spacing of 2.5 μm) was prepared to fabricate the polymer mold. To fabricate the polydimethylsiloxane (PDMS, Sylgard 184, Dow Corning) replica from the silicon master, the PDMS elastomer base and curing agent were mixed at the weight ratio of 10:1. The mixed solution was poured on the master, and was thermally cured for 1 h at 70 °C. The cured PDMS replica was carefully removed from the master mold and was precisely cut for the fabrication of the polyurethane acrylate (PUA, PUA MINS 311RM, Minuta Tech) mold. Subsequently, a small amount of PUA was dropped onto a PDMS replica, and a polyethylene terephthalate film with a thickness of 250 μm was lightly pressed against the dropped PUA resin. The assembly was then cured with ultraviolet (UV) light (Fusion Cure System, Minuta Tech) for 5 min. After the removal of the PDMS replica, we performed the final curing of the cured PUA mold with UV exposure for 12 h.

Fabrication of microscale patterned anode-support

Ceramic tape-casting and thermal lamination processes were used to fabricate an anode-support for 3DA-cells and Planar-cells. A slurry was

prepared for the tape casting composed of 8 mol % $\text{Y}_2\text{O}_3\text{-ZrO}_2$ (YSZ, Tosho) and NiO (Sumitomo) powders at the weight ratio of 44:56. Ethyl alcohol and toluene were used as base solvents, and dibutyl phthalate (Sigma Aldrich), KD-1 (Sigma Aldrich), and polyvinyl butyral (Sigma Aldrich) were utilized as the plasticizer, dispersant, and binder, respectively. Anode tape sheets were prepared for the anode substrate, which included the pore-forming additive, polymethyl methacrylate (Sunjin Chemical), and an anode-functional layer (AFL) without a pore former. For the one-step imprinting process, a multilayered anode-substrate was fabricated with a thickness of 1 mm by stacking several sheets of NiO-YSZ tapes, a sheet of AFL, and the pyramidally patterned PUA mold at a pressure of 14.89 MPa at 80 °C for 15 min. The pyramidally patterned anode body was sintered at 1300 °C for 4 h. The sintered anode support was cut into $2 \times 2 \text{ cm}^2$ pieces for the preparation of the full cell.

Fabrication of solid oxide fuel cells

The following deposition process was employed for cell fabrication, and was conducted using various thin-film deposition techniques. A radiofrequency (RF) sputtering system (2-inch system, Korea Vacuum Tech) and pulsed-laser deposition (PLD) process were employed for the respective deposition of electrolyte and cathode materials. A nanoscale anode functional layer (nAFL) composed by NiO-YSZ was deposited over the sintered anode support with the use of magnetron RF sputtering (NiO:YSZ = 56:44 wt %). To densify the nAFL and prevent Ni

agglomeration, the anode support was annealed for 1 h at 1200 °C. Both YSZ and $\text{Ce}_{0.9}\text{Gd}_{0.1}\text{O}_{1.95}$ (CGO) layers were deposited over the densified nAFL using sputtering. In all of the sputtering process, the RF power of 100 W and the substrate temperature of 700 °C were applied, and the ambient argon gas was used at a pressure of 5 mTorr. The deposition time of nAFL, YSZ, and CGO layers, were set at 12, 6, and 2 h, respectively. To fabricate a dense electrode with an area of $1 \times 1 \text{ cm}^2$, $\text{La}_{0.6}\text{Sr}_{0.4}\text{CoO}_{3-\delta}$ (LSC) was deposited over the CGO layer using PLD for 2 h at an ambient oxygen pressure of 300 mTorr and a substrate temperature of 700 °C.

Characterization of anode support and full cells

The variations of the elastic modulus of the anode substrate was measured using a transverse rupture strength testing machine (5982, INSTRON) as a function of temperature (25 to 1300°C). An anode substrate of width 5 mm, length 10 mm, and thickness 1 mm was prepared as a specimen for each temperature of the thermal annealing profile including debinding and sintering steps. During the electrochemical performance test, air and 3 % humidified hydrogen were fed as the oxidant and the fuel at a rate of 200 mL min^{-1} . The open-circuit voltage (V_{OC}) and electrochemical performances of the cells were analyzed at three different temperatures, and electrochemical impedance spectroscopy was conducted with an electrochemical analyzer (Iviumstat, Ivium Technologies) at the broad frequency range of 0.1 to 1×10^6 Hz. To observe the microstructures of the cells, we used a scanning electron microscopy (SEM, Merlin, ZEISS).

Focused-ion beam (FIB, Helios NanoLab 600, FEI) was used to prepare the specimen for transmission electron microscope (TEM). For the acquisition of high-resolution images of the cells, transmission electron microscopy (TEM, Talos F200X, FEI), and TEM combined with energy dispersive X-ray spectroscopy analyses were conducted.

Microstructure analysis with 3D reconstruction

The 3D reconstruction processes of 3DA-cells and Planar-cells were conducted using a FIB–SEM, dual beam system (Helios Nanolab G3 UC, FEI). To prepare the specimen for FIB tomography, epoxy resin (EpoVac System, Struers) was infiltrated onto the cathode and was cured for a day. After overnight curing, repeated FIB slicing and SEM imaging were performed with a thickness of 30 nm along the z -axis. 3D reconstructions from both cells were analyzed based on additional processes (*e.g.*, aligning, sectioning, trimming and characterizing), and the structural variables were measured with the Avizo 9.0 software package (FEI VSG).

4.3. Results and Discussion

4.3.1. 3D ceramic architectures with microscale ceramic imprinting

Typical ceramic materials composed of strong covalent/ionic bonds yield high-elastic moduli and low-ductility responses. These hard and brittle mechanical properties suppress the plastic deformation compared to other soft and ductile materials, polymers, and metals. Thus, ceramics have a limited capability to deal with defects, fractures, and molding. As a result, it is very difficult for us to fabricate large-sized structures, or precisely implement microscale architectures using only ceramic matrices. A SOFC, a typical ceramic-based energy device, has been studied as a two-dimensional multilayer membrane with small-sized and plain-shaped structures owing to the property limitations of the ceramics. Considering that nonceramic energy devices have recently led to innovative breakthroughs, reducing the internal resistance and increasing the reactive interface area in applications of 3D architectures, these limitations of the SOFC structure are unfortunate^{10,22}. To achieve the advantages of 3D architectures in ceramics, we developed the MCI process using the polymer-to-ceramic matrix transition, and applied it to the anode substrate in SOFCs. **Figure 4.1a–c** shows the process flow for the fabrication of a 3D SOFC architectures in three steps: i) the preparation of an imprinting mold, ii) pattern imprinting on an anode substrate, and iii) multilayer thin-film deposition. As shown in **Figure 4.1a**, we obtained the first

polydimethylsiloxane (PDMS) replica from a silicon master, and we fabricated a final polyurethane acrylate (PUA) mold using a cured PDMS replica. The final imprinting mold has an equilateral, square pyramidal pattern with an edge length of 5 μm and a pitch of 2.5 μm (see **Figure 4.1d**, left column). Because a UV-curable PUA mold has an elastic modulus of 350–10,000 MPa, which is hundreds times larger compared to PDMS, its mold patterns are not significantly deformed during the high-pressure conditions of the imprinting step³⁹. These features of the PUA mold are advantageous for the pattern transfer process in ceramics. Along with the preparation of the rigid imprinting molds, the substrate preparation capable of plastic deformation and particle rearrangement in the imprinting process constitutes another key process. Although tape casting is a classical ceramic processing technique, we modified the processing conditions to consider rearrangement and packing of ceramic particles suitable for the MCI process. The polyvinyl butyral binder applied in this process has a low glass-transition temperature (approximately 80 °C) similar to the thermal lamination condition of the anode tapes. Accordingly, we could simultaneously proceed with the multilayer lamination of the anode tapes, and the application of the MCI processes on these tapes⁴⁰. It also helps the rearrangement and packing of ceramic powder during lamination and subsequent heat treatment, thus ensuring that the transferred pattern structures are well maintained. This whole process can be explained by the principle of matrix transition and variations of the elastic modulus (E) of anode tapes as follows. **Figure 4.1e** shows the detailed fabrication steps of the anode-tapes and the relevant elastic modulus of anode tapes using the

MCI process. The measured elastic modulus of anode tapes are in good agreement with the reported experiments⁴¹⁻⁴³ and clearly show the polymer-to ceramic matrix transition with respect to the processing temperature. The imprinting step requiring plastic deformation has a polymer matrix ($E \sim 10$ MPa) in which dominates the mechanical properties of the anode substrate, while the green ceramic substrate ($E \sim 20$ GPa) after the subsequent heat treatment manifests the electrochemical properties of the ceramics. The shape of the fabricated pyramidal pattern is shown in the scanning electron microscopy (SEM) images of **Figure 4.1d** that confirm that pattern imprinting was successfully performed before and after annealing. **Figure 4.2** shows the imprinted interface with various shapes (*e.g.*, lines, prisms). Based on these, we can confirm that the MCI process is useful for fabricating microscale ceramic architectures without depending on pattern shapes. As a final step of this process, we fabricated the diffusion-barrier layer (DBL), electrolyte, and cathode layer, using thin-film deposition techniques, such as sputter and pulsed-laser deposition (PLD), to facilitate microscale 3D architectures and maximize cell performance. As shown in **Figure 4.1c**, the nanoscale anode functional layer (nAFL) contains few pores and a reduced surface roughness. This layer was deposited on a substrate by a sputtering process for reliable deposition of a dense electrolyte layer and a porous cathode layer. The nAFL layer was annealed at 1200 °C for 1 h, prevented the cracking of the electrolyte by metal agglomeration in a reducing atmosphere, and produced a substrate with fewer surface defects⁴⁴. The electrolyte and DBL were then deposited with a different, subsequent sputtering process. We finally obtained a 3D SOFC

architecture based on the deposition of a $\text{La}_{0.6}\text{Sr}_{0.4}\text{CoO}_{3-\delta}$ (LSC) cathode layer with a thickness of 3 μm using a PLD process. To understand the structural and electrochemical characteristics of a 3D SOFC architecture, a reference cell with planar interfacial structure was also prepared in this study using the same material and processing conditions. Hereafter, we respectively abbreviate 3D and reference planar-surface cell architectures as “3DA-cells” and “Planar-cells”.

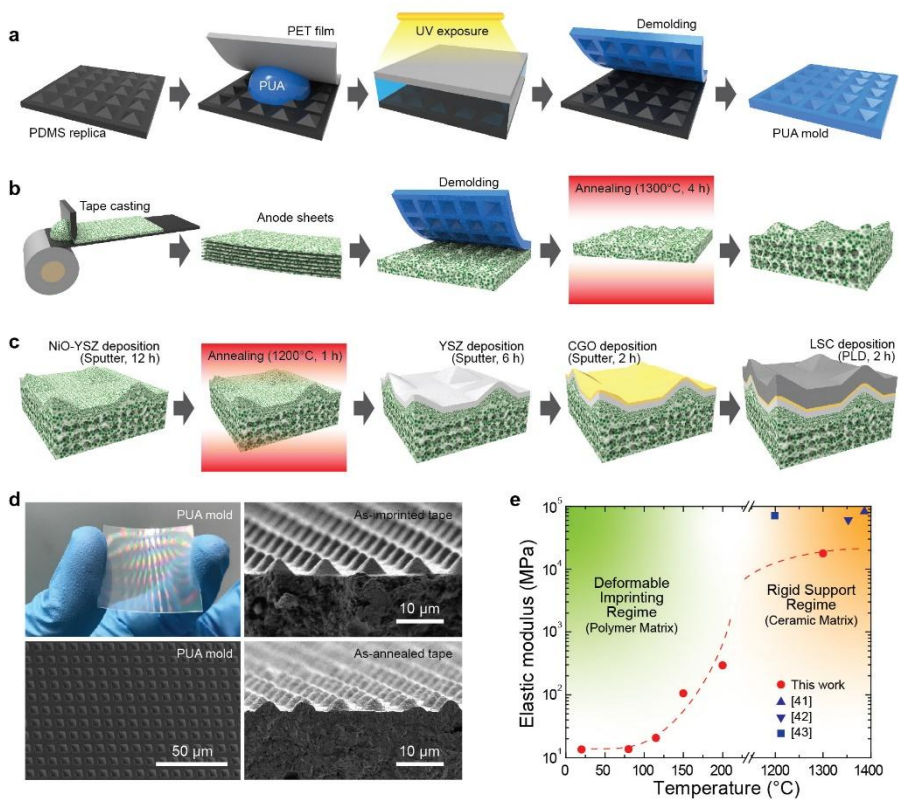


Figure 4.1. Fabrication of 3D ceramic multilayer architectures. Schematic illustrations of the (a) preparation of PUA mold from a PDMS replica, (b) molding process used to fabricate a 3D NiO–YSZ substrate architecture, and (c) implementation of the multilayer thin-film deposition process. (d) Snapshots and SEM images of a PUA mold (left), as-imprinted NiO–YSZ anode tapes (top-right) and as-annealed NiO–YSZ anode tapes (bottom-right). (e) Variations of the elastic modulus of anode tapes with temperature.

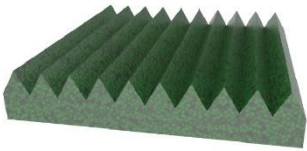
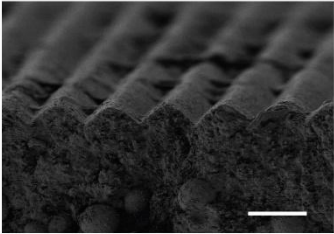
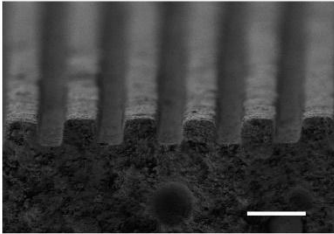
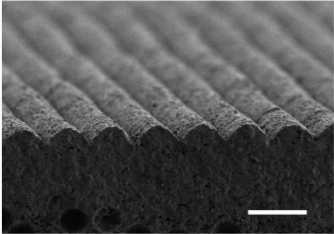
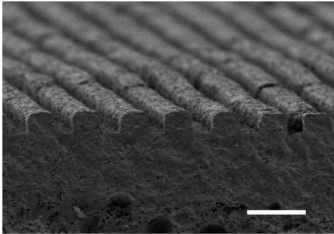
	Prism	Line
Schematic illustration		
SEM image (as-imprinted)		
SEM image (as-annealed)		

Figure 4.2. Schematics and SEM images of as-imprinted and as-annealed states of prism- and line-shaped NiO–YSZ structures. All scale bars correspond to 10 μm .

4.3.2. Superior power-generating performance with 3D architectures

Figure 4.3a shows the configuration and microstructure of the 3DA-cell obtained after the entire fabrication process is completed. To achieve a stable electrochemical reaction at a temperature (T) of 500 °C or higher, we chose $\text{Ce}_{0.9}\text{Gd}_{0.1}\text{O}_{1.95}$ (CGO) and Y_2O_3 -stabilized ZrO_2 (YSZ) as thin DBL (thickness, $t = 200$ nm) and dense electrolyte ($t = 1.5$ μm), respectively. We applied them as CGO/YSZ multilayers on the NiO–YSZ anode substrate. Compared with the microstructure of the Planar-cell in **Figure 4.4**, we clearly clarify that the pyramidal pattern of the 5 μm edge-length was successfully fabricated in the 3DA-cell from the anode to the cathode layers. As shown in **Figure 4.3b**, we tested two different SOFCs (3DA-cells and Planar-cells), and obtained their cell potential (V_{cell}) and power density (PD) curves as a function of temperature using hydrogen and air as fuel and oxidants, respectively. The open-circuit voltage (V_{OC}) of both cells were approximately 1.1 V. These were close to the theoretical values, and thus verified that the dense electrolyte and gas-tight sealing were successfully applied. Interestingly, the 3DA-cell exhibits superior electrochemical performance, which is improved by at least 17.6 % to 54.6 % compared to the Planar-cell in the entire temperature range. At the operating temperatures of 500 and 600 °C, the 3DA-cells yield maximum power densities (PD_{max}) of 0.523 and 1.417 W cm^{-2} , while the Planar-cells yield respective PD_{max} values equals to 0.338 and 1.205 W cm^{-2} . The issues on structural and electrochemical stability of a 3DA-cell, which can be result from the improved cell performance, were also examined based on a long-

term cell operation at 550 °C under constant current load (0.6 A). As shown in **Figure 4.5**, this 3DA-cell exhibited degradation rates which were less than 0.01 % per hour in the 50 h tests. Based on these outcomes, this cell type is considered to have reasonable cell stability that is comparable to conventional powder-based planar-type SOFCs. In particular, most of the micro-SOFCs reported thus far have high Ohmic and electrode polarization resistances, and thus use noble metal catalysts or adopt free-standing membrane structures, which are very small in size, high in processing cost, and extremely low in cell stability^{34,35}. By contrast, our 3DA-cells reported herein employed a 3D interface architecture that maximized the reaction area within the same projection area, and thus minimized the electrochemical resistance, while they maintained electrochemical cell stability in typical cell structures. We believe that this 3D structure achieved based on the use of the MCI and thin-film deposition processes can be fabricated in various ways, regardless of the material and cell configuration. Herein, we successfully reproduced the electrochemical advances of these 3D structures with CGO as the electrolyte material for use in challenging low-temperature operations. CGO materials with higher oxygen-ion conductivity at low temperatures were chosen as the main electrolyte instead of YSZ, and an ultra-thin YSZ film was then introduced as an electron-barrier layer to solve the leakage current of CGO in low oxygen partial pressure conditions. Considering the final structure of this 3DA-cell in **Figure 4.6a**, we verified that the MCI process facilitate the fabrication of such complex configurations in a CGO-based 3DA-cell. The configuration and microstructure of this Planar-cell is also shown in **Figure**

4.7, thus allowing us to identify the unique 3D architectures of the 3DA-cells and the difference in the microstructures between cells. **Figure 4.6b** shows the electrochemical power-generating performance of two CGO-based cells with or without the 3D structures. This CGO-based 3DA-cell exhibits notable PD_{\max} values equal to 0.233 and 0.931 W cm^{-2} at 400 and 500 °C, respectively, which yield better performance by approximately 86 and 76 % compared to the corresponding Planar-cell at the same temperature.

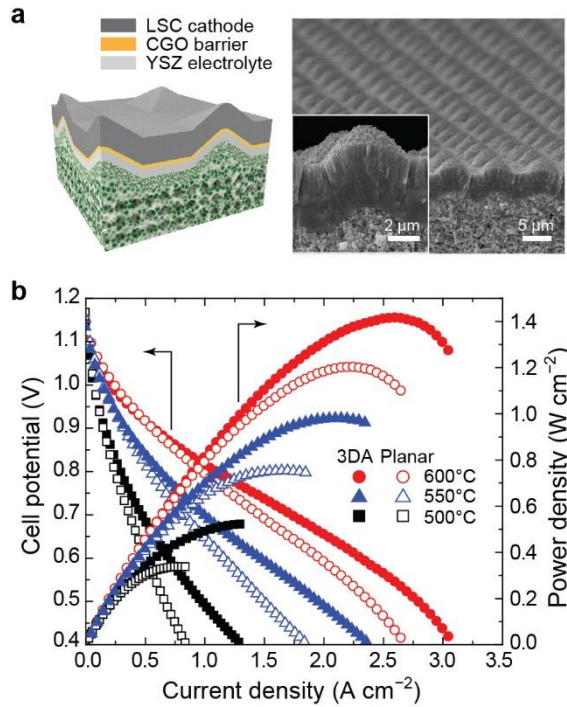


Figure 4.3. (a) Schematic illustration (left) and SEM images (right) of a YSZ-based 3DA-cell. The inset show the magnified SEM image of a pyramidal structure. (b) Potential and power density curves of 3DA-cells and Planar-cells at three different operating temperatures.

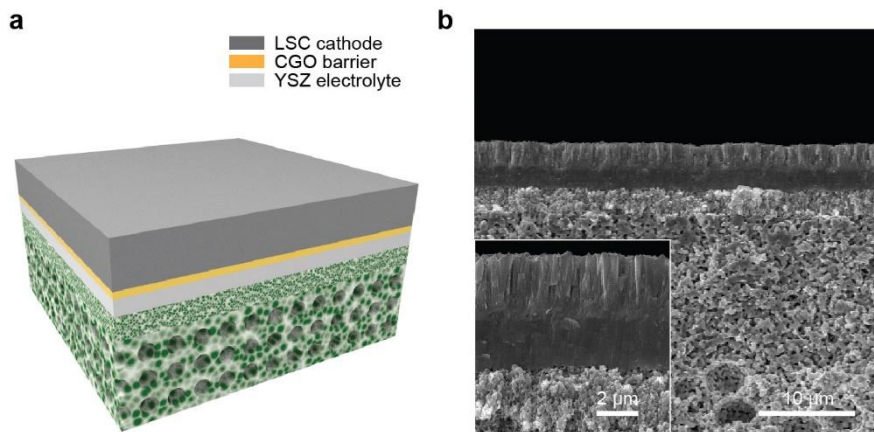


Figure 4.4. (a) Schematic and (b) SEM images of an YSZ-based Planar-cell.

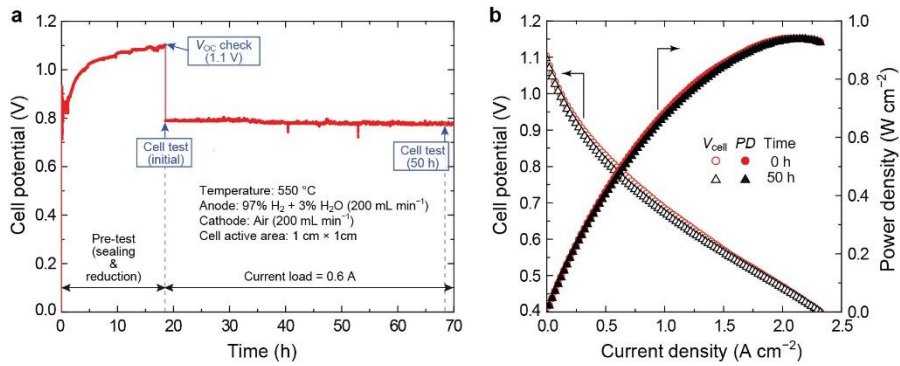


Figure 4.5. Recorded test results of a YSZ-based 3DA-cell during a period of 50 h. (a) Measured cell potential in the presence of a constant current load of 0.6 A at 550 °C and (b) cell potential and power density curves at 0 and 50 h.

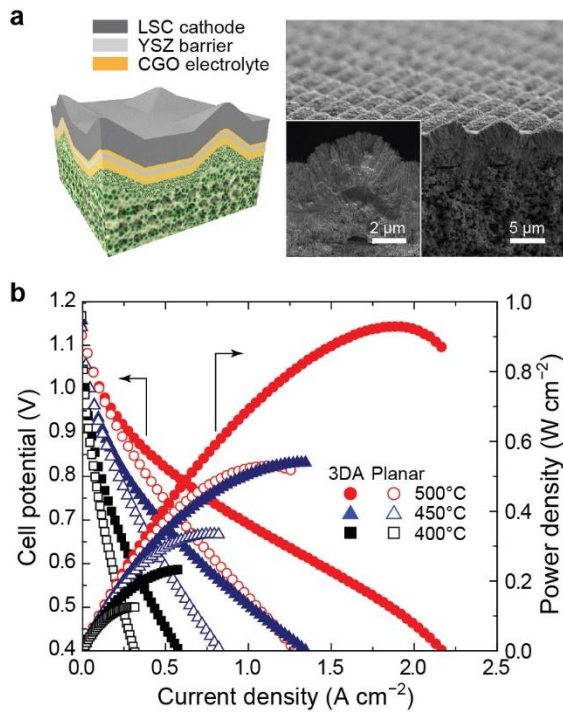


Figure 4.6. (a) Schematic illustration (left) and SEM images (right) of a CGO-based 3DA-cell. The inset show the magnified SEM image of a pyramidal structure. (b) Potential and power density curves of 3DA-cells and Planar-cells at three different operating temperatures.

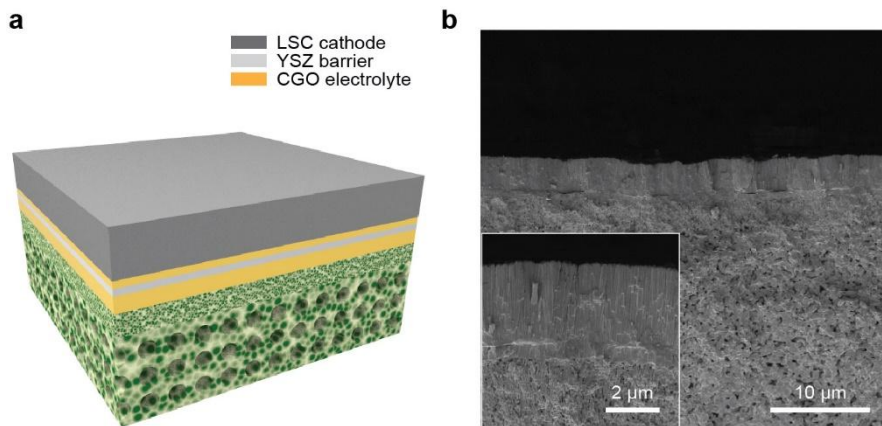


Figure 4.7. (a) Schematic and (b) SEM images of a CGO-based Planar-cell.

4.3.3. Microstructural and electrochemical analysis of 3D-architected SOFCs

We investigated the origins of the excellent electrochemical performances of the 3DA-cells based on various quantitative analyses. As mentioned above, our 3DA-cells have 3D interface structures based on the use of the MCI and thin-film deposition processes. Therefore, we used more rigorous and comprehensive methods to analyze electrochemical data related to electrochemical performance improvements in 3DA-cells. The 3D reconstruction technique with focused-ion beam (FIB) and SEM helped us clearly quantify the configuration and dimensions of the architectures of the 3D ceramic multilayers which were implemented in the 3DA-cells. We analyzed the 3DA-cell and the Planar cell with respective dimensions of $6.09 \times 6.09 \times 13.08 \mu\text{m}^3$ and $6.09 \times 6.09 \times 12.51 \mu\text{m}^3$ in the x , y , and z directions. As shown in **Figure 4.8a** and **Table 4.1**, the segmentation and reconstruction of each layer was successfully performed, and all quantitative values related to the 3D structure were obtained. As we expected, the measured surface area of a 3DA-cell was approximately 23 % larger than that of the Planar-cell. This increase in the surface area of the 3DA-cell is approximately 71 % of the theoretical value (*i.e.*, overall surface area of the pyramidally shaped imprinting mold), which is reasonable considering the densification occurring in the thermal annealing process. The thickness reduction of the electrolyte deposited by the sputter was also confirmed. Using the same sputtering conditions, we confirmed that the increased interface area of the 3DA-cell has a smaller electrolyte

thickness by approximately 28 % compared to the Planar-cell. We quantitatively verified that these structural changes of the 3D reaction interface were closely related to the electrochemical characteristics based on the measured EIS spectra of each cell as a function of temperature. As shown in the EIS results of **Figure 4.8b**, we examined the evoked effects following the increases of the interfacial area and decreases of the electrolyte thickness in 3DA-cells based on the analysis of their polarization ASR (ASR_{pol}) and Ohmic ASR (ASR_{ohm}) responses. The ASR_{pol} value of the 3DA-cells at 0.75 V was $0.395 \Omega \cdot \text{cm}^2$, which was approximately 19 % lower than that of the Planar-cell (*i.e.*, $0.488 \Omega \cdot \text{cm}^2$). This result was attributed to the increased reaction sites of the 3DA-cell for oxygen-reduction reaction (ORR) compared to the Planar-cell. Similarly, the ASR_{ohm} of the 3DA-cell was $0.161 \Omega \cdot \text{cm}^2$ at 0.75 V, which was approximately 52 % lower than that of the Planar-cell ($0.337 \Omega \cdot \text{cm}^2$). The increase in interfacial area and the decrease in electrolyte thickness simultaneously contributed to the Ohmic resistance associated with oxygen-ion transport. The reduction of ASR_{ohm} in the 3DA-cell is thus explained. **Figure 4.8c** shows the ASR values of the CGO- and YSZ-based 3DA-cells in the forms of Arrhenius plots in the Ohmic and polarized parts over a broad temperature range. The overall resistance of the 3DA-cell was lower than that of the Planar-cell in every aspect, but the reduction in resistance due to the 3D interfacial effect appears to be greater in the low-temperature region and in the Ohmic part. The reduction in the polarization resistance due to the 3D interface is also more effective at low temperatures, but the improvement in the cell performance is limited owing to the

polarization resistance which increases considerably in the low-temperature region.

The SOFC with the 3D structure implemented in this study is an innovative achievement of ceramic processing that is completed based on the combination of the MCI and thin-film deposition processes. We successfully fabricated a SOFC with increased electrochemical performance and stability that ranged from low to intermediate temperatures, regardless of material and cell configuration. Although there are some reports on the 3D structures in the field of SOFCs^{32–38,45–47}, our 3DA-cells are superior to the existing ones in terms of the total power output (P_{total}) and degradation rate of the cell. As shown in **Figure 4.9**, **Figure 4.10** and **Table 4.2**, we summarize the electrochemical performance of our 3DA-cells and the previously reported 3D SOFC architectures in the literature^{32–38,45,46} with respect to the various electrochemical benchmarks (*e.g.*, V_{OC} , PD_{max} , P_{total} , and degradation rate). As shown in **Figure 4.9**, the total power output and cell stability of the silicon-based 3DA-SOFCs (blue region) is very poor owing to the limitations of cell size and configuration, while the macroscale 3DA-cell (orange region), which includes laser processing and imprinting, has limitations in the cases of low PD_{max} and high-temperature operations owing to the thick electrolyte layer. By contrast, this study achieved the highest PD_{max} value at the largest area ($1 \times 1 \text{ cm}^2$) compared to previous reports, thus showing a *W*-scale output that is two to three orders of magnitude higher compared to corresponding values reported in the literature^{32–36}. At the same time, we note that our results attained a satisfactory cell stability based on the achievement of a

reasonable degradation rate of 0.1 % per hour, despite the complicated 3D structure.

Cell type	Sample dimension (μm)	Interface area of LSC and CGO ($\mu\text{m}^2/\mu\text{m}^3$)	Film thickness (μm)	
			YSZ electrolyte	CGO DBL
3DA-cell	$6.09 \times 6.09 \times 13.08$	1.286	1.29	0.20
Planar-cell	$6.09 \times 6.09 \times 12.51$	1.047	1.79	0.33

Table 4.1. Detailed structural information of 3DA-cells and Planar-cells obtained from the 3D reconstruction technique.

Ref	A_{cathode} (mm ²)	V_{OC} (V)	PD_{max} (W cm ⁻²)	P_{total} (W)	T (°C)	Degradation test	Patterning process	Substrate type
[32]	0.01	0.85	0.186	2×10^{-5}	450	N/A	Etching	Si substrate (free- standing membrane)
[33]	0.36	1.09	0.861	3×10^{-3}	450	N/A		
[34]	0.002	1.05	1.300	2×10^{-5}	450	30% loss per h		
[35]	0.01	1.10	1.340	1.3×10^{-4}	500	20% loss per h		
[36]	1.262	1.04	0.317	4×10^{-3}	400	Stable V_{OC} , 30 h		
[37]	50	1.1	0.280	0.140	800	N/A		
[38]	50	1.1	0.251	0.126	800	N/A	Spray coating	YSZ electrolyte support
[45]	50	1.14	0.066	3.3×10^{-2}	800	N/A		
[46]	64	~1.1	0.095	6.1×10^{-2}	800	N/A	Powder imprint	Ni-YSZ support
This work	100	1.10	1.417	1.417	600	N/A	Microscale Ceramic Imprinting	
	100	1.10	0.982	0.982	550	0.01% loss per h		
	100	1.10	0.523	0.523	500	N/A		

Table 4.2. Comparison of electrochemical performance of the developed (this study) and previously reported 3D SOFC architectures.

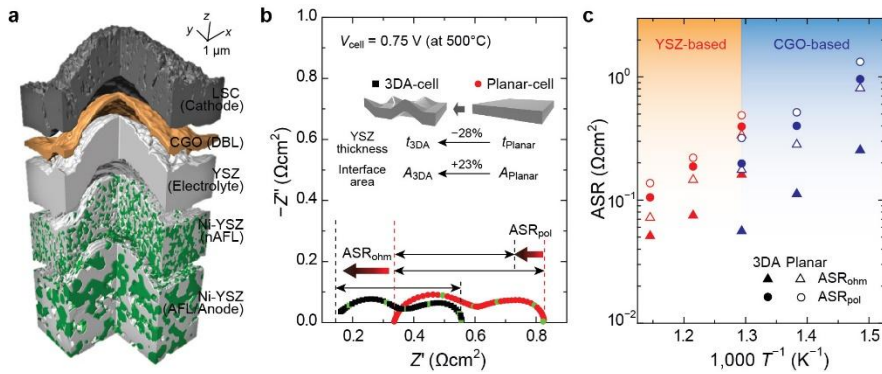


Figure 4.8. (a) 3D reconstructed cell structure for one repeating unit of the compartment of a YSZ-based 3DA-cell. (b) Measured impedance spectra of 3DA-cell and Planar-cell at the cell potential of 0.75 V at operating temperature of 500 °C. The calculated structural parameters of 3DA-cells and Planar-cells are obtained with the use of the 3D reconstruction technique. (c) Arrhenius plot of the ASR_{ohm} and ASR_{pol} of 3DA-cells and Planar-cells at various operating temperatures.

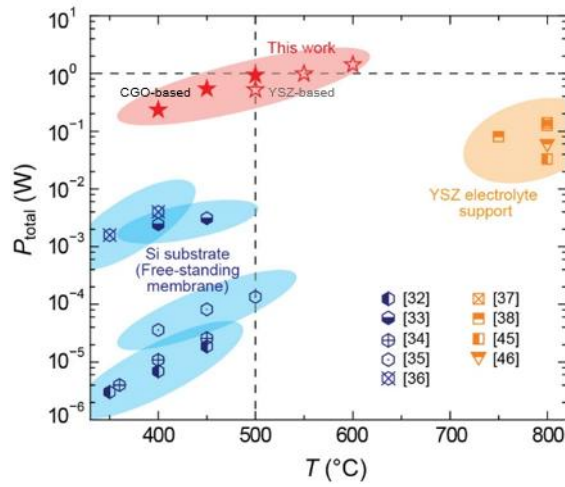


Figure 4.9. Comparison of the total power output in this work compared to the previously reported 3D SOFC architectures as a function of temperature.

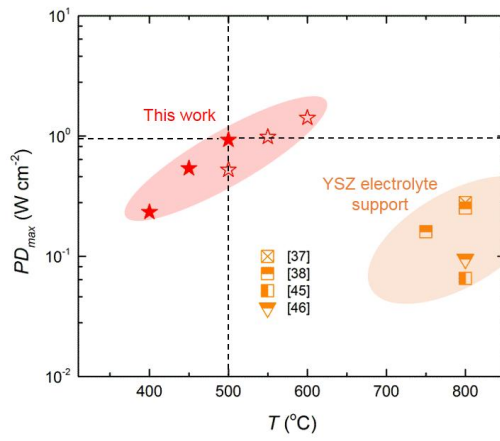


Figure 4.10. Comparison of the maximum power density in this work compared to the previously reported 3D SOFC architectures as a function of temperature.

4.4. Conclusions

In summary, we developed a novel MCI process to achieve a 3D interface of ceramic materials, and integrated it with vacuum thin-film deposition to develop high-performance SOFCs. Although ceramic materials have been limited in applications of the imprinting process using elastic and/or plastic deformation, we successfully performed microscale imprinting of ceramics based on the utilization of complementary polymer additives and polymer-to-ceramic matrix transition. Particularly, this technique enables the implementation of a one-step process of thermal lamination and the microscale pattern imprinting of polymer–ceramic composite sheets to fabricate easily an anode substrate with 3D interface architectures. Herein, a pyramidally shaped pattern with an edge length of 5 μm was implemented over a large area ($1 \times 1 \text{ cm}^2$). Furthermore, the SOFC with a 3D interface was fabricated using various ways, regardless of the material and cell configurations, based on its combination with a multilayer thin-film deposition process. These cells yielded PD_{max} values which were approximately equal to 1 W cm^{-2} at $550 \text{ }^\circ\text{C}$, and a performance improvement of approximately 30 % compared to typical Planar-cell types using the same material and deposition process. The quantitative analyses with the 3D reconstruction and EIS techniques showed that the increased surface area of a 3DA-cell resulted in the reduction of the electrolyte thickness and the increase of the ORR active sites. Correspondingly, the total ASR was reduced by approximately 32 % compared to the planar

reference cell types. The 3D SOFC architectures fabricated herein exhibited an outstanding electrochemical performance among the SOFCs reported previously in terms of the various electrochemical benchmarks (*i.e.*, PD_{\max} , P_{total} , and degradation rate). The development of a novel MCI process and its application to ceramic fuel cells with microscale interfaces marked a milestone in the microscale ceramic process. Accordingly, these will be applied as a core technology to achieve an innovative breakthrough in various ceramic devices in the future.

4.5. References

1. Chou, S. Y.; Keimel, C.; Gu, J. Ultrafast and direct imprint of nanostructures in silicon. *Nature* **417**, 835–837 (2002).
2. Chou, S. Y.; Krauss, P. R.; Renstrom, P. J. Imprint lithography with 25 nm resolution. *Science* **272**, 85–87 (1996).
3. Guo, L. J. Nanoimprint lithography: Methods and material requirements. *Advanced Materials* **19**, 495–513 (2007).
4. Choi, S. J.; Yoo, P. J.; Baek, S. J.; Kim, T. W.; Lee, H. H. An ultraviolet-curable mold for Sub-100-nm lithography. *Journal of the American Chemical Society* **126**, 7744–7745 (2004).
5. Jung, G. Y.; Ganapathiappan, S.; Ohlberg, D. A. A.; Olynick, D. L.; Chen, Y.; Tong, W. M.; Williams, R. S. Fabrication of a 34 x 34 crossbar structure at 50 nm half-pitch by UV-based nanoimprint lithography. *Nano Letters* **4**, 1225–1229 (2004).
6. Schulz, H.; Lyebyedyev, D.; Scheer, H.-C.; Pfeiffer, K.; Bleidiessel, G.; Grützner, G.; Ahopelto, J. Master replication into thermosetting polymers for nanoimprinting. *Journal of Vacuum Science & Technology B: Microelectronics and Nanometer Structures* **18**, 3582 (2002).
7. Kong, J.; Chapline, M. G.; Dai, H. Capillary force lithography. *Advanced Materials* **13**, 1386–1389 (2001).
8. Jang, S.; Kim, M.; Kang, Y. S.; Choi, Y. W.; Kim, S. M.; Sung, Y. E.; Choi, M. Facile multiscale patterning by creep-assisted sequential imprinting and fuel cell application. *ACS Applied Materials and Interfaces* **8**, 11459–11465 (2016).
9. Zhang, F.; Chan, J.; Low, H. Y. Biomimetic, hierarchical structures on polymer surfaces by sequential imprinting. *Applied Surface Science* **254**, 2975–2979 (2008).
10. Kang, S. M.; Jang, S.; Lee, J. K.; Yoon, J.; Yoo, D. E.; Lee, J. W.; Choi, M.; Park, N. G. Moth-eye TiO₂ layer for improving light harvesting efficiency in perovskite solar cells. *Small* **12**, 2443–2449 (2016).

11. Smith, A. J.; Wang, C.; Guo, D.; Sun, C.; Huang, J. Repurposing Blu-ray movie discs as quasi-random nanoimprinting templates for photon management. *Nature Communications* **5**, 1–5 (2014).
12. Boccard, M.; Battaglia, C.; Hänni, S.; Söderström, K.; Escarré, J.; Nicolay, S.; Meillaud, F.; Despeisse, M.; Ballif, C. Multiscale transparent electrode architecture for efficient light management and carrier collection in solar cells. *Nano Letters* **12**, 1344–1348 (2012).
13. Franklin, D.; Chen, Y.; Vazquez-Guardado, A.; Modak, S.; Boroumand, J.; Xu, D.; Wu, S. T.; Chanda, D. Polarization-independent actively tunable colour generation on imprinted plasmonic surfaces. *Nature Communications* **6**, 1–8 (2015).
14. Lin, D.; Tao, H.; Trevino, J.; Mondia, J. P.; Kaplan, D. L.; Omenetto, F. G.; Dal Negro, L. Direct transfer of subwavelength plasmonic nanostructures on bioactive silk films. *Advanced Materials* **24**, 6088–6093 (2012).
15. Spinelli, P.; Ferry, E.; Van De Groep, J.; Van Lare, M.; Verschuuren, A.; Schropp, I.; Atwater, A.; Polman, A.; Spinelli, P.; Ferry, V. E.; Van De Groep, J.; Van Lare, M.; Verschuuren, M. A.; Schropp, R. E. I.; Atwater, H. A.; Polman, A. Plasmonic light trapping in thin-film Si solar cells. *Journal of Optics* **14**, (2012).
16. Bae, W. G.; Kim, S. M.; Choi, S. J.; Oh, S. G.; Yoon, H.; Char, K.; Suh, K. Y. In situ realization of asymmetric ratchet structures within microchannels by directionally guided light transmission and their directional flow behavior. *Advanced Materials* **26**, 2665–2670 (2014).
17. Zhang, F.; Low, H. Y. Anisotropic wettability on imprinted hierarchical structures. *Langmuir* **23**, 7793–7798 (2007).
18. Kobayashi, T.; Shimizu, K.; Kaizuma, Y.; Konishi, S. Formation of superhydrophobic/superhydrophilic patterns by combination of nanostructure-imprinted perfluoropolymer and nanostructured silicon oxide for biological droplet generation. *Applied Physics Letters* **98**, (2011).
19. Ho, A. Y. Y.; Yeo, L. P.; Lam, Y. C.; Rodríguez, I. Fabrication and analysis of gecko-inspired hierarchical polymer nanosetae. *ACS Nano* **5**,

- 1897–1906 (2011).
20. Lee, S. H.; Kim, S. W.; Kang, B. S.; Chang, P. S.; Kwak, M. K. Scalable and continuous fabrication of bio-inspired dry adhesives with a thermosetting polymer. *Soft Matter* **14**, 2586–2593 (2018).
 21. Raut, H. K.; Baji, A.; Hariri, H. H.; Parveen, H.; Soh, G. S.; Low, H. Y.; Wood, K. L. Gecko-inspired dry adhesive based on micro-nanoscale hierarchical arrays for application in climbing devices. *ACS Applied Materials and Interfaces* **10**, 1288–1296 (2018).
 22. Cho, H.; Moon Kim, S.; Sik Kang, Y.; Kim, J.; Jang, S.; Kim, M.; Park, H.; Won Bang, J.; Seo, S.; Suh, K. Y.; Sung, Y. E.; Choi, M. Multiplex lithography for multilevel multiscale architectures and its application to polymer electrolyte membrane fuel cell. *Nature Communications* **6**, 1–8 (2015).
 23. Kim, S. M.; Kang, Y. S.; Ahn, C.; Jang, S.; Kim, M.; Sung, Y. E.; Yoo, S. J.; Choi, M. Prism-patterned Nafion membrane for enhanced water transport in polymer electrolyte membrane fuel cell. *Journal of Power Sources* **317**, 19–24 (2016).
 24. Lee, J. H.; Kim, D. W.; Jang, H.; Choi, J. K.; Geng, J.; Jung, J. W.; Yoon, S. C.; Jung, H.-T. Enhanced solar-cell efficiency in bulk-heterojunction polymer systems obtained by nanoimprinting with commercially available AAO membrane filters. *Small* **5**, 2139–2143 (2009).
 25. Jang, S.; Kang, J. S.; Lee, J. K.; Kim, S. M.; Son, Y. J.; Lim, A.; Cho, H.; Kim, J.; Jeong, J.; Lee, G.; Sung, Y. E.; Choi, M. Enhanced light harvesting in mesoscopic solar cells by multilevel multiscale patterned photoelectrodes with superpositioned optical properties. *Advanced Functional Materials* **26**, 6584–6592 (2016).
 26. Li, Y.; Meng, L.; Yang, Y.; Xu, G.; Hong, Z.; Chen, Q.; You, J.; Li, G.; Yang, Y.; Li, Y. High-efficiency robust perovskite solar cells on ultrathin flexible substrates. *Nature Communications* **7**, 1–10 (2016).
 27. Kil, E. H.; Choi, K. H.; Ha, H. J.; Xu, S.; Rogers, J. A.; Kim, M. R.; Lee, Y. G.; Kim, K. M.; Cho, K. Y.; Lee, S. Y. Imprintable, bendable, and shape-

- conformable polymer electrolytes for versatile-shaped lithium-ion batteries. *Advanced Materials* **25**, 1395–1400 (2013).
28. Xu, Y.; Zhou, M.; Wen, L.; Wang, C.; Zhao, H.; Mi, Y.; Liang, L.; Fu, Q.; Wu, M.; Lei, Y. Highly ordered three-dimensional Ni-TiO₂ nanoarrays as sodium ion battery anodes. *Chemistry of Materials* **27**, 4274–4280 (2015).
 29. Li, W.; Zhou, Y.; Howell, I. R.; Gai, Y.; Naik, A. R.; Li, S.; Carter, K. R.; Watkins, J. J. Direct imprinting of scalable, high-performance woodpile electrodes for three-dimensional lithium-ion nanobatteries. *ACS Applied Materials and Interfaces* **10**, 5447–5454 (2018).
 30. Ormerod, R. M. Solid oxide fuel cells. *Chemical Society Reviews* **32**, 17–28 (2003).
 31. Singhal, S. Advances in solid oxide fuel cell technology. *Solid State Ionics* **135**, 305–313 (2000).
 32. Kim, Y. B.; Gür, T. M.; Kang, S.; Jung, H. J.; Sinclair, R.; Prinz, F. B. Crater patterned 3-D proton conducting ceramic fuel cell architecture with ultra thin Y:BaZrO₃ electrolyte. *Electrochemistry Communications* **13**, 403–406 (2011).
 33. Su, P. C.; Chao, C. C.; Shim, J. H.; Fasching, R.; Prinz, F. B. Solid oxide fuel cell with corrugated thin film electrolyte. *Nano Letters* **8**, 2289–2292 (2008).
 34. An, J.; Kim, Y. B.; Park, J.; Gür, T. M.; Prinz, F. B. Three-dimensional nanostructured bilayer solid oxide fuel cell with 1.3 W/cm² at 450 °C. *Nano Letters* **13**, 4551–4555 (2013).
 35. Chao, C.-C.; Hsu, C.-M.; Cui, Y.; Prinz, F. B. Improved solid oxide fuel cell performance with nanostructured electrolytes. *ACS Nano* **5**, 5692–5696 (2011).
 36. Baek, J. D.; Yu, C. C.; Su, P. C. A silicon-based nanothin film solid oxide fuel cell array with edge reinforced support for enhanced thermal mechanical stability. *Nano Letters* **16**, 2413–2417 (2016).
 37. Cai, G.; Gu, Y.; Ge, L.; Zhang, Y.; Chen, H.; Guo, L. Modification of electrolyte surface with ‘windows’ and ‘dimples array’ structure for SOFC

- based on YSZ electrolyte. *Ceramics International* **43**, 8944–8950 (2017).
38. Cai, G.; Zhang, Y.; Dai, H.; He, S.; Ge, L.; Chen, H.; Guo, L. Modification of electrode/electrolyte interface by laser micro-processing for solid oxide fuel cell. *Materials Letters* **195**, 232–235 (2017).
 39. Kim, S. M.; Kang, S. M.; Lee, C.; Jang, S.; Kim, J.; Seo, H.; Bae, W. G.; Yang, S.; Yoon, H. Repeated shape recovery of clustered nanopillars by mechanical pulling. *Journal of Materials Chemistry C* **4**, 9608–9612 (2016).
 40. Kim, J. H.; Shin, S. S.; Noh, H. S.; Son, J. W.; Choi, M.; Kim, H. Tailoring ceramic membrane structures of solid oxide fuel cells via polymer-assisted electrospray deposition. *Journal of Membrane Science* **544**, 234–242 (2017).
 41. Sarantaridis, D.; Chater, R. J.; Atkinson, A. Changes in physical and mechanical properties of SOFC Ni–YSZ composites caused by redox cycling. *Journal of The Electrochemical Society* **155**, B467 (2008).
 42. Biswas, S.; Nithyanantham, T.; Saraswathi, N. T.; Bandopadhyay, S. Evaluation of elastic properties of reduced NiO-8YSZ anode-supported bi-layer SOFC structures at elevated temperatures in ambient air and reducing environments. *Journal of Materials Science* **44**, 778–785 (2009).
 43. Pihlatie, M.; Kaiser, A.; Mogensen, M. Mechanical properties of NiO/Ni-YSZ composites depending on temperature, porosity and redox cycling. *Journal of the European Ceramic Society* **29**, 1657–1664 (2009).
 44. Noh, H. S.; Son, J. W.; Lee, H.; Ji, H. Il; Lee, J. H.; Lee, H. W. Suppression of Ni agglomeration in PLD fabricated Ni-YSZ composite for surface modification of SOFC anode. *Journal of the European Ceramic Society* **30**, 3415–3423 (2010).
 45. Dai, H.; He, S.; Chen, H.; Guo, L. A novel method of modifying electrolyte surface at mesoscale for intermediate-temperature solid oxide fuel cells. *Ceramics International* **42**, 2045–2050 (2016).
 46. Tsumori, F.; Xu, Y.; Miura, H.; Osada, T. Improvement of solid oxide fuel cell by imprinted micropatterns on electrolyte. *Micro & Nano Letters* **8**,

571–574 (2013).

47. Tokumaru, K.; Tsumori, F.; Kudo, K.; Osada, T.; Shinagawa, K.
Development of multilayer imprint process for solid oxide fuel cells.
Japanese Journal of Applied Physics **56**, 2–6 (2017).

Chapter 5.

Conclusion

5.1. Conclusion

In summary, we have developed multiscale LT-SOFCs with various three-dimensional architecturing technologies. First, each layer of the fuel cell was fabricated via an ESD process, a continuous process at the atmospheric pressure, which can produce uniform membranes. In particular, we analyzed the role of polymer dispersant on the microstructure after sintering process to establish a methodology of fabrication of a dense electrolyte layer and a uniform porous cathode layer. From those methods, the full cell was fabricated using the ESD process on the anode support. Next, we suggested an advanced precursor-solution ESD process that is suitable to form nanoparticles for the multiscale electrode architecturing. The previously reported precursor-solution ESD method was difficult to fabricate thin films due to high substrate temperature and high flow rate. However, by decreasing nozzle-tip diameter, we established stable spray condition on a room-temperature substrate. The optimized precursor-solution ESD process was applied to the researches of nanoscale interlayer and the development of novel infiltration process. The fuel cell with the LSC-CeO₂ nanoscale interlayer showed higher cell performance than the

reference cell due to the increased triple phase boundary and strengthened adhesion properties. In addition, we developed a humidification-assisted ESD infiltration process that can uniformly infiltrate the precursor-solution into the entire electrode area and control the degree of infiltration through the combination with the humidification system. From the effect of homogeneously formed nano-catalysts, the cell with the ESD infiltration process using humidification showed higher maximum power density than the cell with the conventional infiltration process. Finally, to maximize the effect of multiscale electrode architecturing technologies, a fuel cell with a three-dimensional interface structure was required. We used polymer-to-ceramic matrix transition strategy for three-dimensional interface architecturing. An anode support with a three-dimensional interface structure was fabricated by a microscale ceramic imprinting method. Then, combined with thin film technology, a three-dimensionally architected SOFC was fabricated. The YSZ-based 3DA-cell showed higher performance than the YSZ-based planar-cell and resulted in high stability. As a result, the LT-SOFC was implemented by fabricating a CGO-based 3DA-cell with a power output of 1 W at an operating temperature of 500 °C.

5.2. Future direction

We have developed three-dimensional electrode architecturing technologies and a three-dimensional interface architecturing technology to implement an LT-SOFC. In this part, we will describe the future strategies for the advancement of each technology and the integration of technologies.

At three-dimensional interface architecturing in chapter 4, fuel cell performance enhances in proportion to the increased interface area. Therefore, it is advantageous to use a pattern with a large interface area to enhance the cell performance. The pyramid pattern used in this study has a theoretical area increase rate of 32.5 % compared to the flat structure. While, if a prism pattern or a line pattern was used, it could be advantageous to improve the performance since the area increase rate is 41.4 % and 100 %, respectively. And also, as shown above, a prism or line shaped anode support could be fabricated. However, the valley structure of the prism pattern and the vertical lateral structure of the line pattern cause serious problems in the subsequent electrolyte deposition process. The SOFC electrolyte has to be dense to prevent gas mixing, but cracks in the valley structure of the prism and poor step coverage characteristics of the vertical lateral structure of the line cause defects in the electrolyte structure and result in low performance. Therefore, it is necessary to use a pattern that has no valley or sharp structure and is suitable for conformal coating. We believe that a high-aspect ratio cone pattern and a tetrahedral structure pattern could be breakthrough alternatives, and plan to experiment.

Next, we will discuss the combination of three-dimensional interface architecturing technology and other deposition processes besides thin film technology. The process of depositing the electrolyte layer on the anode support before annealing is limited. If screen printing is used, which is the traditional method of fabricating electrolytes, the three-dimensional architectures on the anode support may be removed due to the pressure of the blade through the mesh. And, if lamination method with tape casted electrolyte sheet is used, large pores will be generated at the interface between anode and electrolyte. Spin coating and atomic layer deposition (ALD) processes are also difficult to apply because of high surface roughness of patterned anode support. Therefore, the applicable electrolyte deposition processes are sputtering, PLD and ESD. Since the ESD process is an aerosol deposition method, it is not affected by the surface roughness and can maintain the pattern structure. From the use of ESD process, we fabricated a dense YSZ electrolyte layer on the prism shaped anode support. CGO diffusion barrier layer and cathode layer were deposited to fabricate full cell. The fabricated SOFC showed ~ 1.1 V OCV, which is close to the theoretical value, and higher cell performance than the flat shape cell. However, structural asymmetry from a flat electrolyte/cathode interface could be controversial in electrochemical analysis and require further studies.

So far, various technologies have been suggested in this thesis to lower the SOFC operating temperature. Researches to lower the SOFC operating temperature through the development and integration of multiscale architecturing technologies should be advanced. We hope that our

technology will contribute to accelerating the application of SOFC to mobile systems such as electric vehicles and unmanned aerial vehicles.

3차원 아키텍처링을 이용한 멀티스케일 저온형 고체산화물 연료전지

서울대학교 대학원 기계항공공학부

신 성 수

요약

차세대 에너지 변환 분야인 연료전지는 공해물질 배출이 없는 친환경 전기화학 소자이며 중량대비 에너지 출력이 높은 특징이 있다. 그 중 고체산화물 연료전지는 발전효율이 가장 높으며 수소 이외의 연료를 내부 개질을 통해 사용할 수 있다는 장점이 존재한다. 하지만 전통적인 고체산화물 연료전지는 700 °C 이상의 고온 구동에 의한 열적 성능 저하 현상, 높은 시스템 유지 비용, 이동형 소자로의 적용이 어려운 문제점이 존재하고, 따라서 저온형 고체산화물 연료전지 구현을 위한 구조 개선 등의 연구가 주목을 받고 있다. 본 학위 논문에서는 저온형 고체산화물 연료전지 구현을 위해 기존 연구의 한계를 극복한 멀티스케일 진극 아키텍처링 기술과 새로운 3차원 계면 아키텍처링 기술을 개발하였다.

먼저, 분말-현탁액 전기분사 증착 공정을 이용해 고체산화물 연료전지 각 요소들의 구조를 최적화하고, 최적화된 구조들로 제작된 연료전지의 고온에서의 안정적인 구동을 확인하였다. 우리가 집중해서 연구한 부분은 전기분사 증착 공정 시 현탁액 안의 세라믹

파우더와 고분자 바인더의 질량비에 따라 소결 후의 구조물 모양이 달라지는 현상이었다. 이에 연료극과 공기극 사이의 기체 이동을 차단하기 위한 치밀한 전해질 층 제작을 위해 polyvinyl butyral 고분자 바인더를 사용하였고, 공기 유동을 위해 다공성이어야 하는 양극 층 제작을 위해 polyvinylpyrrolidone 고분자 바인더를 사용하였다. 양극 분말과 고분자 바인더의 1:1 질량비 조건에서 균일하게 분산이 된 양극 층을 제작할 수 있었으며, 입도 분석과 전자주사현미경 분석을 통해 현탁액의 분산 정도가 증착 직후 구조뿐만 아니라 소결된 구조에도 영향을 미치는 것을 확인할 수 있었다. 결국 최적화된 전해질 구조, 양극 구조를 갖는 연료전지는 작동온도 650 °C에서 805 mW/cm²의 최고출력밀도를 기록하였으며, 작동온도 650 °C, 0.4 A/cm²의 일정한 전류밀도 조건에서 100 시간동안 1.5 %의 열화율을 기록, 장기 안정성 측면에서도 뛰어난 것을 확인하였다.

다음으로, 전구체 용액 전기분사 증착 공정을 통해 세라믹 박막 제작 기술과 새로운 침투 공정 기술, 두 가지 다른 공정 기술을 개발하여 멀티스케일 전극을 구현하였다. 첫 번째로, 세라믹 박막 제작 기술을 통해 나노중간층을 제작하고 고체산화물 연료전지 전해질 층과 양극 층 사이에 적용을 한 연구를 진행하였다. 이전 연구에서는 분말-현탁액 전기분사 증착 공정을 이용해 마이크로 두께의 구조물을 제작하였다면, 후속 연구에서는 전구체 용액 전기분사 증착 공정을 이용해 마이크론 이하 두께의 박막 구조물을 제작하였다. 특히, 본 연구에서는 8 μm 틱 지름의 실리카 노즐을 사용하여 에탄올에 비해 표면장력이 세 배 정도인 탈이온수를 용매로 사용하는 전구체 용액의 안정적인 분무 조건을 확립하게

되었다. 이를 통해 제작된 nano adhesion layer (nAL)과 nano cathode functional layer (nCFL)을 고체산화물 연료전지 전해질 층과 양극 층 중간에 삽입하여 nAL-cell과 nCFL-cell을 제작하였고, 나노중간층이 없는 Ref-cell을 제작하여 세 가지 연료전지의 성능을 평가하였다. 그 결과 nCFL-cell의 경우 nAL-cell과 Ref-cell에 비해 작동온도 650 °C에서 각각 18 %, 13 % 증가한 최고출력밀도를 기록하였으며, 이는 전해질 층과 양극 층 사이에 삽입된 나노중간층에 의해 물리적인 접착이 좋아짐에 따른 산소 이온 이동경로의 증가와 감소한 LSC 입자 크기에 따른 산소환원반응 면적의 극대화에 의한 것이다. 두 번째로, 새로운 침투 공정을 통해 전극 구조를 개선함으로써 고체산화물 연료전지 성능을 향상시키는 연구를 진행하였다. 전통적인 침투 공정은 마이크로피펫을 이용하여 전구체 용액을 전극 위에 떨어뜨리는 간단한 방법으로 진행되었다. 하지만 전극 전 표면에 균일하게 침투되지 않는 문제점이 존재하고, 침투된 전구체 용액의 유동을 조절하기 힘들다는 단점이 존재한다. 본 연구에서는 전구체 용액 전기분사 증착 공정을 이용해 전극 전 표면에 균일하게 증착을 하고 가습의 정도에 따라 전구체 용액 침투의 정도를 조절할 수 있는 새로운 침투 공정 방법을 개발하여 연료전지에 적용하였다. 우리의 새로운 침투 공정을 적용시킨 연료전지는 전통적인 침투 공정을 사용한 연료전지와 침투 공정을 사용하지 않은 연료전지에 비해 작동온도 650 °C에서 각각 15 %, 215 % 증가한 최고출력밀도를 기록하였으며, 이는 가습을 통해 균일하게 침투된 전구체 용액이 소결 거동을 거치면서 산소환원반응 면적 증가 등 전극 반응 메커니즘에 도움을 주었기 때문이다.

마지막으로, 고체산화물 연료전지 음극 지지체 제작 방법인 테이프

라미네이션 방법과 마이크로 패턴 임프린팅 기술을 결합한 마이크로 세라믹 임프린팅 기술을 개발하여 박막 증착 공정을 이용해 3차원 고체산화물 연료전지를 제작하는 연구를 진행하였다. 세라믹 물질은 열에 강하고 경도가 높으나 부서지기 쉬운 성질이 있기 때문에 마이크로 단위의 표면 패터닝이 힘들다고 알려져 있다. 본 논문에서는 이를 해결하기 위해 고분자-세라믹 복합체 상태인 음극 테이프와 마이크로 패턴이 새겨진 고분자 몰드의 라미네이션을 진행하여 피라미드 패턴이 된 음극 지지체를 제작하였다. 음극 지지체 위에는 스퍼터링과 pulsed laser deposition 공정을 이용해 연료전지를 제작하였다. 라미네이션 과정에서 PUA 고분자 몰드가 없는 평면 구조의 연료전지를 Planar-cell이라 하고 3차원 피라미드 모양으로 제작된 연료전지를 3DA-cell이라 하였다. 3DA-cell 제작에 있어서 YSZ 전해질 구조 연료전지와 CGO/YSZ/CGO 복합 전해질 구조 연료전지를 제작하였는데, 이는 우리의 공정이 물질적인 제한 없이 적용 가능한 것을 의미한다. 제작된 연료전지들의 성능을 측정하였을 때, 작동온도 500 °C에서 YSZ 기반 3DA-cell과 CGO 기반 3DA-cell은 각각 0.523 W와 0.931 W의 최고출력을 기록하여 YSZ 기반 Planar-cell과 CGO 기반 Planar-cell의 0.338 W, 0.530 W에 비해 각각 55 %, 76 % 높은 성능을 기록하였다. 우리가 제작한 피라미드 구조 연료전지의 출력은 지금까지 보고되었던 3차원으로 제작된 고체산화물 연료전지의 출력에 비해 높은 것을 확인할 수 있었다. 또한 YSZ 기반 3DA-cell의 경우, 작동온도 550 °C, 0.6 A/cm²의 일정 전류밀도 조건에서 장기 안정성 평가를 진행하였고 0.01 %/h 열화율을 기록, 높은 안정성과 함께 실제 구동 가능한 출력을 보이는 것을 확인하였다.

주요어: 3차원 아키텍처링, 고체산화물 연료전지, 전기분사 증착,
나노중간층, 침투 공정, 마이크로 세라믹 임프린팅
학번: 2015-30162